UNIVERSITY OF SOUTHAMPTON
FACULTY OF ENGINEERING, SCIENCE AND MATHEMATICS
SCHOOL OF PHYSICS AND ASTRONOMY

Using novel spectral-timing techniques to probe the rapid variability of X-Ray Binaries

by

Tony Wilkinson

Thesis for the degree of Doctor of Philosophy
March 18, 2011

UNIVERSITY OF SOUTHAMPTON

ABSTRACT

FACULTY OF ENGINEERING, SCIENCE AND MATHEMATICS

SCHOOL OF PHYSICS AND ASTRONOMY

Doctor of Philosophy

USING NOVEL SPECTRAL-TIMING TECHNIQUES TO PROBE THE RAPID VARIABILITY OF X-RAY BINARIES

by Tony Wilkinson

X-ray spectral variability is a powerful probe of the relationship between the accretion disc and corona in accreting compact objects. In this thesis, I present the use of variability techniques to disentangle the different variable components of X-ray spectra. By examining correlated variability over a range of timescales, I identify for the first time evidence of intrinsic disc variability on timescales of seconds. I go on to examine, utilising a range of spectral-timing techniques, the role this intrinsic variability might play in driving much of the observed spectral variability in these sources.

CONTENTS

APPENDICES

LIST OF TABLES

LIST OF FIGURES

DECLARATION

I, Tony Wilkinson, declare that the thesis entitled *Using novel spectral-timing techniques to probe the rapid variability of X-Ray Binaries* and the work presented in the thesis are both my own, and have been generated by me as a result of my own original research. I confirm that:

- this work was done wholly or mainly while in candidature for a research degree at this University;
- where any part of this thesis has previously been submitted for a degree or any other qualification at this University or any other institution, this has been clearly stated;
- where I have consulted the published work of others, this is always clearly attributed;
- where I have quoted from the work of others, the source is always given. With the exception of such quotations, this thesis is entirely my own work;
- I have acknowledged all main sources of help;
- where the thesis is based on work done by myself jointly with others, I have made clear exactly what was done by others and what I have contributed myself;
- parts of this work have been published as:
  - Accretion disc variability in the hard state of black hole X-ray binaries 2009, MNRAS, 397, pp. 666-676
  - Pulse-phase-resolved spectroscopy of continuum and reflection in SAX J1808.4-3658 2010, MNRAS, 410, pp. 1513-1520

Tony Wilkinson, March 18, 2011

ACKNOWLEDGEMENTS

First and foremost I'd like to thank my supervisor Phil Uttley for the countless hours he has spent supporting my research, reading my articles, correcting my mistakes and improving my abilities as a scientist. Without his fastidiousness and insight, my PhD would not have been nearly as successful. I would also like to thank Tom Maccarone for many useful discussions over the years and for his support, along with Malcolm Coe, as my academic advisor. Thanks also to Ian McHardy for being very supportive when I required some time away from my PhD, and to Tony Bird for elucidating some of the vagaries of Fortran 77 and for being inferior to me at snooker. I also owe a large debt to Rob Fender, with whom I kept losing bets. Roflcopter. Many thanks also to Sera Markoff and Mike Wise for allowing us to stay at their apartment for a month whilst I worked at UVA. I'm sorry to say that Gingit the cat and I didn't bond, but I like to think we developed a shared respect for one another based wholly upon a burgeoning mutual distrust.

So I move on to my fellow students, those mired in the fetid bowels of their PhD. A big thank you to Pablo, Martin and Omar (who emerged from the bowels sometime ago now smelling of roses), to whom I just *moaned* **incessantly**, usually over coffee or beer. It is to your eternal credit that you feigned interest in my bleating for so long. I shall always covet thy motorcycle Martin and my life feels worse for never having actually played that game of human rights poker we so often talked about. The workshop that Pablo organised certainly re-ignited my enthusiasm for astrophysics at a time when I needed it the most. I should apologise to my office mates Chris and Duncan for taking quite so many phone-calls lately from agencies whilst trying to find reputable employment. Many thanks for the C++ help too, Chris. To the other friends I have met since coming here, the quiet, diffident ninja Liz, the cultured, sophisticated kick-boxing fan of bodice-ripping dramas Grace, the creme-egg eating, running machine (or creme-egg eating machine, running) Sadie, the quick-witted queen of the facebook status and owner of some of the best t-shirts I've ever seen, Tana, the intrepid cycling explorer and vehement hater of burpees Matt and the Bruce Parry look alike and all round nice guy Mark - I shall miss you all. No doubt I have forgotten people in this list I've bumped in to over the last three years who should be here too.

Lee, Pablo, Anna, Pieter, PG & Gabriele - we'll always have Hawaii. A place where you can walk in to a hotel that you aren't even staying at, play pool for free and get given free cocktails. I think it truly was paradise, especially compared to my previous conference experience of defecating in a Turkish toilet after drinking some dodgy Efes pilsner. I'll never quite know how, in my inebriated state, I managed to scramble on to that stone horse at the Waikoloa village, but thanks Lee for documenting it. Really, thanks.

Thanks to the always helpful and thoroughly competent Beike Hiemstra, Maria Diaz

Trigo, Chris Done, Dave Russell, Anna Watts, Alessandro Patruno, Adam Ingram and Matt Middleton. You make very difficult stuff look awfully trivial.

Oh, lets not forget the 2010 Ashes series shall we, Jess? 3-1. What a MASSACRE. Wear your t-shirt with pride, and occasionally do the sprinkler.

Finally, and **most** importantly, none of this would have been possible without the unwavering support and encouragement I received from my gorgeous wife, Hannah, through good times and bad. Thanks, love.

Tony Wilkinson, March 18, 2011

> One morning I shot an elephant in my pajamas. How he got into my pajamas I'll never know.
>
> GROUCHO MARX

To Mum, Dad, Hannah, Maddy & Max

All generalizations are false, including this one.

MARK TWAIN (1835 – 1910)

I was walking through Central Park, and I saw an old man smoking. Nothing makes a smoker happier than to see an old person smoking. This guy was ancient, bent over a walker, puffing away. I'm like, ”Duuude, you're my hero! Guy your age smoking, man, it's great.” He goes, ”What? I'm 28.”

BILL HICKS (1961 – 1994)

One had to cram all this stuff into one's mind for the examinations, whether one liked it or not. This coercion had such a deterring effect on me that, after I had passed the final examination, I found the consideration of any scientific problems distasteful to me for an entire year.

ALBERT EINSTEIN (1879 - 1955)

1

Introduction

In this chapter I shall present an overview of the physics of mass accretion, and briefly discuss the behaviour that leads to outbursts in X-ray binary systems. I shall discuss the X-ray spectra of black hole and neutron-star binaries, describe their most general state classifications according to the dominant spectral components and introduce the truncated-disc model. Finally, I have included a section in which I describe the basic tools at the astronomer's disposal to quantify the time and energy variability of such sources, including the Power Spectral Density (PSD), variability spectrum and lag spectrum.

1.1 X-Ray Binaries

Accretion is defined as a process of growth or increase, typically by the gradual accumulation of matter. When a steady flow of material (mass per unit time or $\dot{M}$) falls on to a compact object, it releases half of its gravitational potential energy in the form of radiation, mechanical energy (such as outflows or jets) and thermal energy[1]. Accretion is the most efficient form of energy conversion in the universe. The efficiency with which the rest mass energy of accreted material can be converted

---

[1] it releases more if the compact object has a solid surface since the kinetic energy of the material itself can be liberated on impact.

in to energy can be parameterised by η in the equation $L_{acc} = \eta \dot{M} c^2$, where L_{acc} is the accretion luminosity. For the nuclear fusion of hydrogen in to helium $\eta \sim 0.007$, compared to $\eta \sim 0.1$ for accretion. For a given mass accretion rate, the accretion luminosity scales as M/R (known as the 'compactness parameter' (Frank, King, & Raine, 2002)), where M is the mass of the compact object and R is its radius. It is unsurprising therefore that accretion plays a dominant role in the emission of objects with large M/R ratios, most notably black holes, neutron stars and white dwarfs. An order of magnitude estimate illustrates that stellar mass compact objects radiate at X-ray wavelengths. The energy liberated per unit area in an annulus of the accretion disc due to the change in gravitational potential energy is $\propto M\dot{M}/R^3$. Assuming this is radiated locally as a black body we can qualitatively equate this to the energy flux density σT^4 of a black body. Assuming a black-hole mass of 10 $M_\odot$ and an $\dot{M}$ of 10^{-8} $M_\odot$yr^{-1} then the disc temperature at 50 Schwarzschild radii [2] is of the order 1.5×10^6 K. This corresponds to an average black body temperature of around 0.4 keV, or a wavelength ~3-4 nm in the soft X-ray region of the electromagnetic spectrum. Optically thin, radiatively inefficient emission can emit much higher energy photons with plasma temperatures as high as 10^9 K.

In this thesis I shall concentrate on the variability of X-ray emissions arising due to accretion that takes place in X-ray binaries. I shall concentrate on Low Mass X-ray Binaries (LMXBs) in which the more massive compact object accretes matter from a lower-mass companion via Roche lobe overflow. When a star evolves and expands, its radius can exceed that of its Roche lobe, the region of space within which orbiting material is gravitationally bound to the star. In a binary system matter can flow along equipotentials and become gravitationally bound to the compact object. When the compact object is a highly magnetised neutron star ($\sim 10^8$ G), the accretion flow can be channeled on to the magnetic poles producing an accretion shock. The misalignment of the spin and magnetic poles can lead to pulsations at the spin frequency of the neutron-star, a topic which shall be discussed in chapter 5.

1.2 Mass Accretion

Material accreting onto a compact object spirals inwards and forms a flattened plane, known as an accretion disc. In order to spiral inwards, material in the disc has to lose angular momentum. Angular momentum is conserved in systems in which there are no external torques, so this implies that there must be a torque act-

---

[2] The Schwarzschild radius, R$_s$, is defined as 2GM/c^2 and represents the radius of the event horizon of a non-rotating black hole.

ing on this system. The two key properties of the accretion flow that give rise to such a torque are its Keplerian rotation and the viscosity of the flow itself. An object undergoing Keplerian rotation has an angular frequency, $\omega = \sqrt{GM/R^3}$, that is to say disc material closer to the compact object orbits more quickly than material at a greater distance. If one considers distinct disc annuli rotating differentially in this manner, then the viscosity of the material will lead to shear stress in the rotating fluid. The shear stress is simply a force exerted parallel to the direction of motion of the flow caused by the viscosity of the disc material. A more slowly rotating outer ring will exert a torque which holds back a faster inner ring, and friction between the adjacent annuli will generate heat. It is this 'viscous dissipation' which releases energy in to the disc, which is then radiated as a black body if the disc is optically thick.

The origin of disc viscosity is not entirely clear, and is beyond the scope of this discussion, however a likely candidate is magneto-hydrodynamic (MHD) turbulence (Hawley, Gammie, & Balbus, 1995). A simpler approach is to subsume all of the complex physics in to a dimensionless parameter, $\alpha \leq 1$, and define the viscosity, ν_{vis}, in terms of the disc scale height, H, and the local sound speed c_s (Shakura & Sunyaev, 1973).

$$\nu_{vis} = \alpha H c_s \tag{1.1}$$

It can be shown (Kolb, 2010) that for Keplerian motion, the viscous torque τ_{vis} (or rate of change of angular momentum) is equal to:

$$\tau_{vis} = -3\pi \nu_{vis} \Sigma (GMr)^{1/2} \tag{1.2}$$

where Σ is the surface density of the disc, r the disc radius and M the mass of the compact object. The negative sign in equation (1.2) indicates that the material loses angular momentum and can therefore spiral inwards.

By calculating the viscous dissipation rate per unit surface area, and equating it to the flux emitted by a black body, one can show that the temperature profile of a steady-state (time-independent) optically thick, geometrically thin disc is proportional to $R^{-3/4}\dot{M}^{1/4}$. For non-rotating Schwarzschild black holes, the innermost stable circular orbit (ISCO) lies at 6GM/c^2 (3R$_\mathrm{s}$). It can therefore be seen that more massive black holes have ISCOs lying at larger radii, with correspondingly lower disc temperatures. The accretion disks in Active Galactic Nuclei (AGN) for instance, with their extremely large central black hole mass, emit predominantly in the UV region of the electromagnetic spectrum.

1.3 Timescales in the accretion disc

There are several important characteristic timescales in an accretion disc, one of which has been discussed already, the dynamical or Keplerian timescale. This is the shortest characteristic timescale in the disc I shall discuss, and is the time it takes gravitationally bound material in the disc to complete a Keplerian orbit around the compact object. For a Schwarzschild black-hole, the dynamical time is approximately $t_k \sim 0.3 \times \frac{M}{10M_\odot}\left(\frac{r}{50r_g}\right)^{3/2}$ sec (Gilfanov, 2009). This is about 10 ms at the ISCO of a 10 M⊙ Schwarzschild black hole.

The thermal timescale is the time it takes to establish thermal equilibrium in the disc by balancing heat dissipation and the heat content of the disc. It is defined as:

$$T_{th} = \frac{1}{\alpha} T_{dyn} \tag{1.3}$$

The inward radial drift of accreted material happens on the 'viscous timescale'. It is this radial drift that gives rise to a local mass accretion rate, defined as:

$$\dot{M} = 2\pi r v_r \Sigma \tag{1.4}$$

where v_r is the radial drift velocity. The viscous time is therefore simply r/v_r, which can also be expressed, at some length, as:

$$T_{vis} \simeq \frac{1}{\alpha}(\frac{r}{H})^2 T_{dyn} \tag{1.5}$$

where H is the disc scale height. Using the example above, at the ISCO of a 10 M⊙ Schwarzschild black hole, assuming $\alpha = H/R = 0.1$:

$$T_{dyn} = 10ms \; < \; T_{th} = 0.1s \; < \; T_{visc} = 10s \tag{1.6}$$

1.4 Black Hole X-ray Binary outbursts

LMXBs are often transient, experiencing 'outbursts' where the luminosity increases dramatically for a period of weeks or months and then returns to quiescence. Such a sequence of outbursts is shown in figure 1.1 for the LMXB GX 339-4. During the course of such outbursts, these systems pass through distinct X-ray 'spectral states' which shall be discussed briefly in the next section. The origin of such outbursts is thought to be explained in part by the disc instability model (e.g. Lasota, 2001). As the disc density builds up due to mass transfer from the companion, its

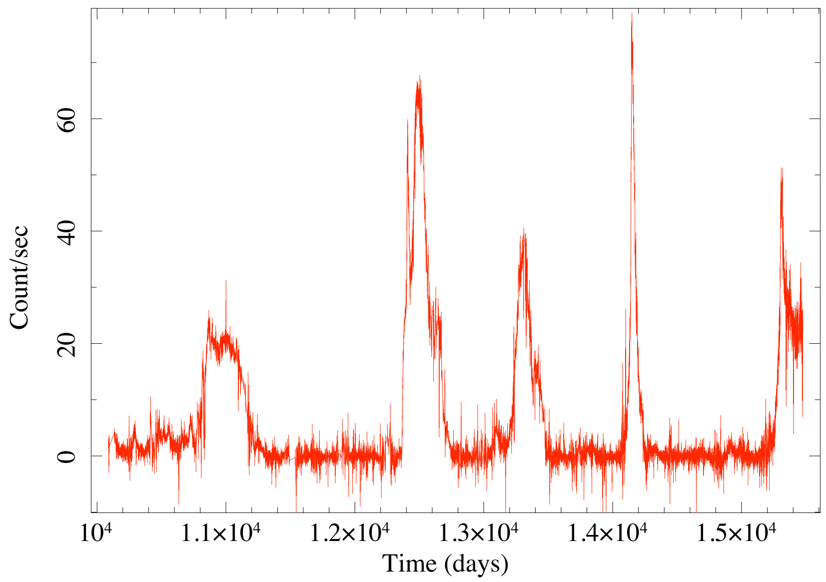

Figure 1.1: RXTE All Sky Monitor light curve of recent outbursts in GX 339-4.

temperature increases and the higher energy photons from the thermal distribution begin to ionise the hydrogen. These photons are therefore absorbed, increasing the disc temperature and a heating wave is propagated throughout the disc ionising virtually all the hydrogen present in the disc. Increased temperature leads to an increased mass accretion rate, since $\nu_{vis} \propto T$ in α-discs (Shakura & Sunyaev, 1973), and material in the disc is consumed. Eventually, the outer disc temperature dips below the hydrogen ionisation temperature and a cooling wave propagates inwards, switching the disc back to a quiescent state whilst mass builds up again.

1.5 X-ray Spectra of X-Ray Binaries

X-ray spectra of Black Hole X-Ray Binaries (BHXRB) show evidence for a two-phase structure to the accretion flow (Eardley, Lightman, & Shapiro, 1975), an optically thick, geometrically thin accretion disc (Shakura & Sunyaev, 1973) giving rise to a blackbody component in the X-ray spectrum, and a hot optically-thin component, usually modelled as a cut-off power law. It has been suggested that the power-law is produced by an inner, optically-thin Advection Dominated Accretion Flow (ADAF) (e.g. Esin, McClintock, & Narayan 1997), which replaces the inner optically thick disc at low accretion rates, and extends down to the Innermost Stable Circular Orbit (ISCO). This implies that the optically thick disc is truncated at some transition radius. Alternatively, the optically thick and optically thin components may co-exist over some range of radii, e.g. if the thin disc is sandwiched by a hot flow or corona (Witt, Czerny & Zycki, 1997; Churazov et al., 2001). The corona may in turn evaporate the innermost regions of the disc at low accretion rates (e.g. Meyer-Hofmeister & Meyer 2003; Mayer & Pringle 2007), so that the optically thin flow is radially separated from the optically thick disc as for the ADAF model. Since the ADAF and corona perform similar roles in that they up-scatter soft photons to produce the observed power-law, we shall henceforth refer to both components interchangeably as the corona, without necessarily favouring either picture.

Regardless of whether the corona is radially or vertically separated from the thin disc, photons up-scattered by the corona will interact with the disc. This interaction gives rise to either scattering or absorption of the incoming continuum emission. The photo-electric absorption cross section is proportional to Z^5/E^3 where Z is the atomic number and E is the energy of the incoming photon. In the process of photo-electric absorption, a photon is absorbed by an atom and one of the orbital electrons of the atom are ejected. The atom is therefore left with a vacancy, usually in the innermost K-shell, which is filled by a higher energy electron transitioning from another shell producing a photon emission line. The combination of the decrease in photo-electric cross section with increasing energy, its dependence on atomic number and the Compton down-scattering of scattered photons leads to a characteristic reflection spectral shape. This spectrum has a break at high (30-40 keV) energies (termed the 'reflection hump') as well as an iron K-edge and fluorescent iron Kα line emission at $\sim$7.1 keV and $\sim$6.4 keV respectively (where approximate values are due to the effects of screening by inner-shell electrons at different ionisations and relativistic Doppler shifts). If there is strong illumination of the disc by the up-scattered photons, then the disc can become highly ionised. Ionisation of the disc causes a drop in the photo-electric absorption, since disc material is less opaque, producing more low energy reflection (scattering). Emission lines emerging from the ionised disc are Compton scattered, broadening the line and edge features. Further broadening of the emission lines occurs due to the rapid rotation of the disc and due to gravitational redshift. All relativistic effects decrease with increasing distance from the black hole. Therefore, narrower emission lines arise from larger radii. An often-neglected consideration is that a significant fraction of the photons interacting with the disc are absorbed and the disc is heated in a process known as thermal reprocessing. Provided that the disc subtends at least a moderate solid angle as seen by the corona, this effect should be particularly significant in the hard state, where the coronal power law continuum dominates the total luminosity. When the power-law luminosity impinging on the disc is high compared to the disc

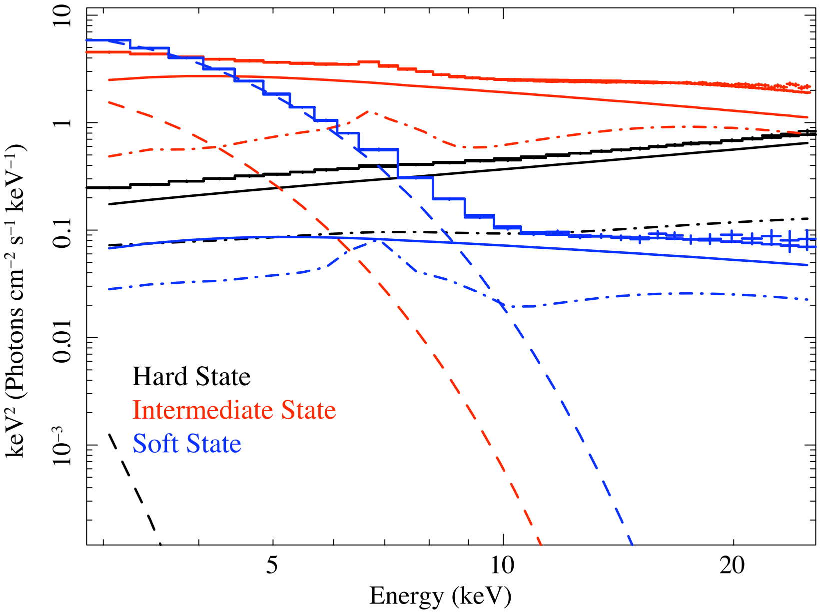

Figure 1.2: Three RXTE observations of GX 339-4 from its 2010 outburst demonstrating different spectral states. Spectra were fitted with a phenomenological model and the individual spectral components can be identified. The blackbody component has a dashed line, the power-law component is a single line and the reflection component is represented as a dot-dashed line. The sum of the spectral components and the data points are also plotted. Such spectra are described as "unfolded spectra", where the data points plotted are the fitted model values multiplied by the ratio of data values to the response folded model.

luminosity due to internal heating, then a significant fraction of the disc blackbody emission should be reprocessed and will therefore track variations of the power law continuum.

The relative strengths of the blackbody and power-law components define the appearance of different 'states' (e.g. Homan et al. 2001). Figure 1.2 shows some examples of spectra obtained from the BHXRB GX 339-4 in different spectral states, which clearly shows differing contributions from the individual spectral components. In the hard state, which I focus on in chapters 2 and 3 of this thesis, the power-law emission dominates the total luminosity and is thought to be caused by inverse Compton scattering of incident disc photons by a thermal (Maxwellian) distribution of electrons. This repeated thermal up-scattering gives rise to a power-law of flux-density $f(E) \propto E^{-\alpha}$ with slope $\alpha = ln(\tau)/ln(1+4\Theta)$ (where τ is the optical depth, Θ is the electron temperature and $\alpha = \Gamma - 1$ is the energy index) (Done et al., 2010). In the soft-state, blackbody emission dominates and the higher energy tail is better described as inverse Compton scattering by a non-thermal, power-law distribution of electrons ($n(\gamma) \propto \gamma^{-p}$). It can be shown (Done et al., 2010) that the power-law index of the resulting spectrum is $\alpha = (p-1)/2$. Typically, given the convention for plotting photon energy spectra described in Appendix A, soft states have $\Gamma > 2$ and their Spectral Energy Distributions (SED) peak at low energies, whilst hard states have $\Gamma < 2$ and their SEDs peak at higher energies.

In the hard state, the variability of the power-law continuum offers further clues to the structure of the accretion flow. Studies of the timing properties of hard state BHXRBs show that the frequencies of broad Lorentzian features in their Power-Spectral Density functions (PSDs, see section 1.6.1) correlate with the strength of the reflection features, as well as the steepness of the power law continuum (Revnivtsev, Gilfanov & Churazov, 2001; Gilfanov, Churazov & Revnivtsev, 1999). These correlations can naturally be explained if the Lorentzian frequencies correspond to a characteristic timescale at the disc truncation radius, e.g. the viscous time-scale, so that as the truncation radius increases, the Lorentzian frequency decreases, with disc reflection and Compton cooling of the optically thin hot flow by disc photons decreasing accordingly. This, as well as the correlation between the reflection scaling factor and the degree of relativistic smearing (Gilfanov, Churazov, & Revnivtsev, 2004) is some of the strongest evidence in favour of a common model for the hard-state of BHXRBs known as the 'truncated-disc model'. It argues that the optically thick, geometrically thin disc can evaporate into an optically thin hot flow at low mass accretion rates[3] $\sim 0.01\ L_{Edd}$. As the disc truncation radius moves inwards, characteristic frequencies in the PSD move to higher frequencies, consistent with variations occurring at smaller radii. The truncated disc model provides a geometric argument explaining the spectral changes in BHXRBs together with the changing characteristic frequencies in the variability power-spectra of these sources.

A common tool used to track the changes in spectral state of a given source with time is the Hardness Intensity Diagram (HID). This is a plot of the total observed counts as a function of the spectral hardness; hardness is defined as the ratio of observed counts in two distinct energy bands. An example of a HID is included in figure 4.1 of chapter 4. A rich phenomenology of source states have been identified, but it is not necessary to examine these in detail here. For an up-to-date discussion of the classification of states and transitions in BHXRBs the reader is referred to Belloni (2009).

---

[3] The Eddington Luminosity, $\mathrm{L_{Edd}}$, is defined as the luminosity at which the outward radiation pressure of accreting material is equal to the total inward gravitational attraction. It is equal to $4\pi \mathrm{GMm_pc}/\sigma_\mathrm{T}$ where m_p is the proton mass, M the black hole mass and σ_T the Thomson cross-section.

The accretion of material onto a neutron star is similar to that of a black hole, with the obvious exception that material accreting onto a neutron star has to impact onto its solid surface releasing kinetic energy in a boundary layer and possibly spinning up the neutron star. This boundary layer creates some spectral differences, but, particularly at low accretion rates, the X-ray variability properties of neutron-stars with low magnetic fields (known as atoll sources) and black hole systems are extremely similar. It is thought that at low mass-accretion rates, the disc is truncated in a similar manner, with seed photons from the surface of the neutron-star being partially Comptonised in the boundary layer and illuminating the hot inner flow. In fact, it has been shown that there is a strong correlation between the break-frequency of band-limited noise and a quasi-periodic oscillation (QPO) often observed above this break in Black Hole Candidates (BHC), atoll sources and a millisecond X-ray pulsar (Wijnands & van der Klis, 1999). It has also been argued that this correlation extends down to white dwarfs (Mauche, 2002). This suggests that the band-limited noise and QPO are caused by the same physical mechanism; they most likely originate in the accretion disc, which is common to all systems, and have nothing to do with the presence of a solid surface. We would expect to see similar disc variability behaviour in neutron-stars, which would further confirm the link between the accretion flows of neutron-star and black-hole binaries. It is perhaps no surprise, therefore, that the atoll class of neutron star X-ray binaries display two distinct states, the island and banana states, analogous to the hard and soft states of BHXRBs respectively.

1.6 Variability

1.6.1 The Power Spectrum

[4] X-ray satellites provide astronomers with time series known as light curves. The continuous emission of X-ray sources are discretely sampled at equal time intervals (even sampling), to produce plots of count rate vs time. One can use Fourier analysis techniques to search for periodicities in such light curves.

The Discrete Fourier Transform (DFT) can be written as:

$$X(\nu_i) = \sum_{k=0}^{N-1} x_k \cos(\frac{2\pi jk}{N}) + ix_k \sin(\frac{2\pi jk}{N}) \tag{1.7}$$

---

[4] Much of the discussion below follows the structure of a lecture given at the Southampton Black Hole Variability 2010 meeting by Simon Vaughan on the 21st May 2010 entitled Black hole variability from limited data and from Vaughan et al. (2003).

where $\nu_j = \frac{j}{N\Delta t}(j = 0, 1, ...N/2)$, $t_k = k\Delta t(k = 0, 1, ..., N-1)$ and x_k = Number of photons detected in time bin k.

This effectively correlates a time signal x(t) with the cos and sin of different frequencies. In reality, the DFT is computed using a fast Fourier transform (FFT) algorithm. Equation (1.7) can be written:

$$X(\nu_i) = R_j + iI_j \tag{1.8}$$

with $R_j = \sum_{k=0}^{N-1} x_k \cos(\frac{2\pi jk}{N})$ and $I_j = \sum_{k=0}^{N-1} x_k \sin(\frac{2\pi jk}{N})$. Since the number of photons in each bin k, x_k, are independent and identically distributed (with a Poisson distribution) random variables, then R_j and I_j will also be normally distributed about a mean of zero (since the cosine and sine terms are distributed about zero). This follows from the central-limit theorem which states that the mean of a large number of independent random variables (in this case the number of photons in a bin) will be normally distributed.

The energy in a signal is proportional to the square of its amplitude. Parseval's theorem states that the total energy in a signal *x(t)* is equal to the area under the square of the magnitude of its Fourier transform (see equation (1.9)). $|X(\nu)|^2$ is called the power-spectral density function, with $|X(\nu)|^2 d\nu$ describing the density of signal energy contained in the differential frequency band ν to ν+dν.

$$\int_{-\infty}^{+\infty} |x(t)|^2 dt = \int_{-\infty}^{+\infty} |X(\nu)|^2 d\nu \tag{1.9}$$

$$P(\nu_j) = A \mid X(\nu_j) \mid^2 = A(R_j^2 + I_j^2) \text{ where } \mathrm{A} = \frac{2\Delta \mathrm{t}}{\mathrm{N}} \tag{1.10}$$

$\mathrm{P}(\nu_\mathrm{j})$ is known as the periodogram (Vaughan et al., 2003; Priestley, 1981), an estimator of the continuous PSD. With this choice of normalisation, A, (which is quoted here without proof), integrating the power over positive frequencies gives the absolute variance in that frequency band.

It can then be shown, since R and I are normally distributed, that the distribution of the powers is a chi-square distribution with 2 degrees of freedom and is *independent of the number of samples, N, obtained.* If such a distribution has an expected value, M, then its variance is M^2. In other words, the periodogram has 100% standard deviation regardless of the amount of data obtained.

To reduce the error, it is necessary to split up the periodogram in to several segments, where periodograms from each of the S non-overlapping intervals are averaged, known as the Bartlett averaged periodogram (Bartlett, 1948). Each estimate of the variance from each segment is statistically independent, and the central limit theorem states that the sum of such independent variables will be normally distributed as the number of segments increases. In this manner, one can obtain a reliable estimate of the standard deviation of the mean variance (power).

In practice, an X-ray source is observed for a long period of time, and the approximation is made that the process is stationary. A stationary process is one for which the expectation values of statistical properties are seen to be independent of time. The observation can then be split up in to many non-overlapping segments and the average properties determined. If the average power observed in L segments is M, then the variance of this average becomes M^2/L, hence the variance decreases as more data is obtained. In summary, taking this approach reduces the variance, but also decreases the frequency resolution of the data since the lowest frequency information obtainable is proportional to the inverse of the length of each segment of the time series.

Any time series generated by a detector will also contain some random noise due to Poisson variations. This corresponds to a white noise process, which has a flat power spectrum. If there are N_i counts in a given bin, then the error in the count rate will be $\sqrt{N_i}/\Delta t$ i.e. the variance is simply $N_i/\Delta t^2$. The flat power spectrum will contribute up to the highest frequency that is sampled (the Nyquist frequency, $1/2\Delta t$) and the integrated power gives the variance as discussed above. Therefore the noise power can be deduced as follows:

$$\int_0^{\nu_{Nyq}} P_{noise} d\nu = P_{noise}\nu_{Nyq} = \frac{P_{noise}}{2\Delta t} = \frac{<N_i>}{\Delta t^2} \tag{1.11}$$

$$P_{noise} = \frac{2<N_i>}{\Delta t} = 2<x> \tag{1.12}$$

The noise power is therefore simply twice the mean count rate.

1.6.2 Cross-correlation, the Lag Spectrum and Covariance

The cross-correlation theorem states that the Fourier transform of the cross-correlation of two time series, s(t) and h(t), is equal to the product of one Fourier transform, S(ν), with the complex conjugate of the other H*(ν). Defining the cross-spectrum as this product, H(ν)*.S(ν), (where * indicates the complex conjugate), using the pentagram notation for the cross-correlation and F to represent the Fourier transform, we have:

$$(s \star h)\ (t) = \int_{-\infty}^{+\infty} s^*(\tau)h(t+\tau)d\tau \tag{1.13}$$

$$F(s \star h) = H(\nu)^* S(\nu) \tag{1.14}$$

The cross-spectrum is the Fourier transform of the cross-correlation function, a complex quantity which can be thought of as a vector in the complex plane (Argand diagram). Representing the Fourier transforms of the two time series as an amplitude, A, multiplied by some randomly distributed phase, ϕ, between 0 and 2π:

$$S(\nu) = A_S(\nu)e^{i\phi_S(\nu)} \tag{1.15}$$

$$H(\nu) = A_H(\nu)e^{i\phi_H(\nu)} \tag{1.16}$$

One can compute the cross-spectrum to obtain:

$$H(\nu)^*.S(\nu) = A_S(\nu)A_H(\nu)e^{i(\phi_S - \phi_H)} \tag{1.17}$$

The identity below applies when the two time series are coherent, that is to say when the time series are linked by means of a linear transfer function which is identical for every realisation of the process.

$$\phi_s(\nu) = \phi_H(\nu) + \Delta \tag{1.18}$$

$$H(\nu)^*.S(\nu) = A_S(\nu)A_H(\nu)e^{i\Delta} \tag{1.19}$$

The argument of the vector is the phase difference, Δ, and this can be converted in to a time-lag by dividing by $2\pi\nu$. The modulus squared of the cross-spectrum contains no phase information, but is equal to $|A_S(\nu)A_H(\nu)|^2$. It is necessary to average together many cross spectra obtained from contiguous segments of data, so that uncorrelated parts of each light curve cancel out, leaving only the correlated components.

If the average cross spectrum is obtained over many segments for every channel of interest with respect to a reference band, R, chosen in such a way that it has high signal-to-noise, then the covariance can be defined in rms units for the ith channel as:

$$\mathrm{Covariance} = \sqrt{\frac{|\mathrm{H_i}(\nu)^{*}.\mathrm{R}(\nu)|^2}{\mathrm{N}|\mathrm{R}(\nu)|^2}} \times \Delta\nu \tag{1.20}$$

Where N is the chosen power-spectral normalisation and the cross spectra and power-spectra are obtained by averaging segments as described above over the frequency range $\Delta\nu$. In this way a covariance spectrum as a function of energy can be obtained. This is the Fourier-resolved covariance spectrum which can be computed over a chosen frequency range. A more simplified overview of the zero-lag covariance spectrum, based on the standard rms spectrum and used to pick out specific timescales of variability, can be found in section 2.3.

1.7 Causes of variability

The power-spectrum of X-ray binaries demonstrates significant variability, $\sim$30% fractional rms in hard-states. As well as aperiodic variability extending over many decades in the frequency domain, the power spectra also sometimes reveal narrower 'quasi-periodic' features of an unknown origin which will be the subject of chapter 4 of this thesis. Typically, power-spectra demonstrate flicker-noise ($P(\nu) \propto 1/\nu$) which dominates at very low-frequencies ($< 10^{-2}$ Hz), but in hard spectral states have excess power at higher frequencies ($10^{-2} - 100$ Hz) known as band-limited noise.

It has been suggested that fluctuations in the viscosity of the disc causes local variations in the mass accretion rate, which propagate inwards to cause the observed variations in X-ray flux (Lyubarskii, 1997). The viscous timescale, the timescale on which variations are able to propagate inwards, is the longest timescale in the accretion disc. Variations of mass accretion rate on shorter timescales are effectively damped, so each radius only contributes significant variations at the local viscous timescale. Variability at high frequencies can't propagate from large radii and is therefore likely to be introduced in to the flow at smaller radii. The broad dynamic range of variability arises due to the range of radii at which viscosity fluctuations are introduced to the flow. It has been shown that, if viscosity fluctuations at all radii have the same relative amplitude, the propagation of $\dot{M}$ variations produces the observed flicker-noise power-spectrum (Lyubarskii, 1997).

There is good evidence that in soft spectral states the disc is extremely stable i.e. the black body component demonstrates only very weak variability (down to an rms of 1%) (Belloni, 2009). This was thought to be because variations in the optically thick geometrically thin disc, with its longer viscous timescale ($(h/r) \sim 0.01$), have a smaller amplitude and therefore do not contribute significantly to the observed flux variability. It can be shown (Churazov et al., 2001) that the amplitude of fluctuations in the disc on a timescale τ will be significantly damped at the characteristic length scale:

$$\frac{\delta r}{r} \sim \sqrt{\frac{\tau}{T_{vis}}} = \frac{h}{r} \tag{1.21}$$

where H is the scale height of the disc. This implies that the observed flicker-noise component must be due to $\dot{M}$ fluctuations occurring in the geometrically thicker part of the flow, the optically thin corona. A picture therefore emerged in BHXRBs that all the variability was generated in the optically thin corona, and the optically thick disc was simply a bystander. In simple terms, it was thought that the optically thin part of the flow was much more transparent to $\dot{M}$ fluctuations than the optically thick disc. The corona therefore effectively propagates such fluctuations without significant damping and modulates the accretion rate at all smaller radii, leading to a significant modulation of the X-ray flux. This notion was supported by the simple observation that the hard-state radiative output is dominated by the power-law emission thought to be associated with an optically-thin flow. Since this state demonstrated much stronger variability, it was natural to link the variability with the hot-flow. However, one important caveat is that studies of variability in hard-states have been limited by a lack of spectral coverage of the disc, which emits at kT < 0.5 keV in these states. It is necessary to study the hard-state variability spectra using the soft X-ray response of *XMM-Newton*, to determine if the disc really is stable in the hard-state.

1.8 Thesis Overview

In chapter 2 I examine the hard-state variability spectrum of GX 339-4. I introduce a new technique to disentangle the correlated variable spectral components of this source, and demonstrate that the disc *is* intrinsically variable in the hard-state. I also present some results from Phil Uttley (Uttley et al., 2011) which provide strong evidence that the intrinsic disc variations lead power-law variations, and therefore drive the variability. This is in complete contrast to the established picture of a stable disc which is described above. Having established that the low frequency Lorentzian feature in the PSD is a disc variability signature, in chapter 3 I go on to explore whether or not changes in this feature can be associated with changes in the truncation radius of the accretion disc. In chapter 4 motivated by recent evidence that disc variability actually *drives* power-law variability, I go on to explore the role intrinsic disc variability might play at higher frequencies in other source states. I present evidence suggesting that intrinsic disc variability could drive the QPO features present in the PSDs of BHXRB. It is clear that we have established a causal connection between intrinsic disc variability and observed modulations of the X-ray flux. In the final chapter, I move from BHXRBs to explore the variability of X-ray emission from the accreting millisecond X-ray pulsar (AMXP) SAX J1808.4-3658, in an attempt to detect changes in the iron-line properties with rotational phase.

You see, wire telegraph is a kind of a very, very long cat. You pull his tail in New York and his head is meowing in Los Angeles. Do you understand this? And radio operates exactly the same way: you send signals here, they receive them there. The only difference is that there is no cat.

ALBERT EINSTEIN (1879 - 1955)

2

Accretion disc variability in the hard-state of black hole X-Ray binaries

In this chapter, I examine the variability spectra of two hard state black hole X-ray binaries, SWIFT J1753.5-0127 and GX 339-4, which have good *XMM-Newton* data for studying simultaneous variations of disc and power-law. The soft and hard band Power-Spectral Densities (PSDs) of these sources demonstrate variability over a wide range of time-scales. However, on time-scales of tens of seconds, corresponding to the power spectral feature generally fitted with a low frequency Lorentzian, there is additional power in the soft band. To interpret this behaviour, I introduce a new spectral analysis technique, the ‘covariance spectrum’, to disentangle the contribution of the X-ray spectral components to variations on different time-scales. I use this technique to show that the disc blackbody component varies on all time-scales, but varies more, relative to the power-law, on longer time-scales. This behaviour explains the additional long-term variability seen in the soft band. Comparison of the blackbody and iron line normalisations seen in the covariance spectra in GX 339-4 implies that the short-term blackbody variations are driven by thermal reprocessing of the power-law continuum absorbed by the disc. However, since the amplitude of variable reflection is the same on long and short time-scales, I rule out reprocessing as the cause of the enhanced disc variability on long time-scales. Therefore, the conclusion is that the long-time-scale blackbody variations are caused by instabilities in the disc itself, in contrast to the stable discs seen in BHXRB soft states. These results provide the first observational evidence that the low-frequency Lorentzian feature present in the PSD is produced by the accretion disc.

2.1 Introduction

Previous analyses of time-averaged spectra for *XMM-Newton* observations of GX 339-4 and SWIFT J1753.5-0127 have shown the existence of the expected blackbody components, together with relativistically broadened reflection features. These have been used to argue that the disc is truncated at significantly smaller radii than previously thought, perhaps only a few gravitational radii (Miller et al., 2006; Miller, Homan, & Miniutti, 2006). However, see Gierliński et al. 2008; Hiemstra et al. 2009; Done et al. 2007 for arguments in favour of disc truncation at larger radii.

The anticipated correlated variations of the blackbody and power-law emission (due to thermal reprocessing) can be studied using variability spectra, e.g. the rms spectrum, which show only the variable components of the spectrum (Vaughan et al., 2003). If the geometry is such that the observed power-law produces reprocessed blackbody emission by X-ray heating the disc, then both power-law and blackbody components should appear together in the variability spectra. Furthermore, by selecting different time ranges covered by these variability spectra (i.e., analogous to the method of Fourier-resolved spectroscopy, Revnivtsev, Gilfanov & Churazov 1999), it is possible to determine whether the low-frequency part of the PSD has a different origin to the high-frequency part in terms of the contributions of blackbody and power-law components. If the optically thick disc does drive the low-frequency Lorentzian, the prediction is that the blackbody component should be stronger in the corresponding variability spectrum.

2.2 Observations and Data Reduction

SWIFT J1753.5-0127 was observed during revolution 1152 for 42 ks by *XMM-Newton* EPIC-pn on 2006 March 24 in *pn-timing* mode using the medium optical filter. The events list was screened using the perl script XMMCLEAN[1] to select only events with FLAG=0 and PATTERN ≤ 4. Examination of light curves showed no

---

[1] http://lheawww.gsfc.nasa.gov/~kaa/xselect/xmmclean

evidence for background flaring. Using SAS Version 7.0, EVSELECT was used to extract the mean spectrum, following the procedure of Miller, Homan, & Miniutti (2006), using event positions between 20 and 56 in RAWX and using the full RAWY range. The SAS tasks ARFGEN and RMFGEN were used to generate the Ancillary Response File (ARF) and Redistribution Matrix File (RMF).

GX 339-4 was observed by *XMM-Newton* on 2004 March 16 during revolutions 782 and 783, again in *pn-timing* mode using the medium optical filter. The SAS command EVSELECT was used to filter the events on TIME to avoid background flaring, producing a total combined exposure of 127 ks. Data reduction was very similar to that for SWIFT J1753.5-0127, using SAS version 7.0, but care was taken to avoid pile-up. Successive columns from the centre of the image were excised in RAWX and spectra extracted until no discernible difference in spectral shape could be identified between successive selections on RAWX, implying that pile-up is no longer significant. The EPIC-pn data was deemed free of pile-up using extraction regions in RAWX from columns 30 to 36 and 40 to 46 (i.e., columns 37 to 39 inclusive were excised). Background spectra were selected in RAWX from columns 10 to 18 over the full RAWY range. To generate an appropriate ARF for the data made in this way, it was necessary to use ARFGEN to generate an ARF for the full region in RAWX from columns 30 to 46 and generate a second ARF from the spectrum of the excluded region (RAWX columns 37 to 39) and then subtract the latter from the former using the command ADDARF[2].

For both sources, the FTOOL GRPPHA was used to scale the background spectra and to ensure that a minimum of 20 counts were in each bin for χ^2 fitting. The EPIC-pn covers the energy range from 0.2-10 keV, but the EPIC Calibration Status Document[3] recommends restricting the fit to energies greater than 0.5 keV. To be conservative, our EPIC-pn spectral fits were restricted to the range 0.7 to 10.0 keV.

Data was extracted from *RXTE* observations which were contemporaneous with the *XMM-Newton* observations. High time and spectral-resolution PCA Event mode data were used to extract mean spectra and make rms and covariance spectra using the same time binning as the EPIC-pn data (see Section 2.3.2). Throughout this chapter I use *RXTE* PCA data in the 3-25 keV range, and fit these together with the corresponding EPIC-pn spectra, tying all fit parameters together but allowing *RXTE* spectral fits to be offset by a constant factor with respect to the simultaneous EPIC-pn fits, to allow for the difference in flux calibration between the PCA and EPIC-pn instruments, and also for the fact that slight flux differences may result from the fact

---

[2] http://xmm.vilspa.esa.es/external/xmm_user_supportdocumentation/sas_usg/USG/node63.html

[3] http://xmm2.esac.esa.int/external/xmm_sw_cal/calib/index.shtml

that the *RXTE* observations covered shorter intervals than the *XMM-Newton* data. A 1 per cent systematic error was assumed in all joint spectral fits to account for uncertainties in instrumental response and cross-calibration. The signal to noise of *RXTE* HEXTE data was not sufficient to perform the covariance analysis described in section 2.3.2.

2.3 Analysis and Results

2.3.1 Power-spectral densities

Before describing the spectral analysis method and results, I first examine the timing properties of each source in soft and hard spectral bands using the power-spectral density function (PSD). For each source, the EPIC-pn data were used to generate light curves with 1 ms time binning in two energy bands: 0.5-1 keV (soft) and 2-10 keV (hard). Only complete segments of 131 s duration[4] were used to construct the PSDs, segments with gaps (which can be common at high count rates in timing mode) were skipped over. The resulting Poisson-noise-subtracted PSDs are shown in figure 2.1. It is clear from the figure that the PSDs are significantly different in shape between the two bands. In GX 339-4, the hard-band PSD shows two broad components, with the higher-frequency component appearing to be shifted to even higher frequencies in the hard band. In SWIFT J1753.5-0127, soft and hard PSDs appear, within the noise, to overlap more closely at higher frequencies. However, in both sources the soft band PSD shows relatively larger low-frequency power compared to the PSD components at frequencies above $\sim$ 0.2 Hz. This $\sim$ 20% extra low-frequency power at lower X-ray energies may be associated with the soft excess emission, e.g. if the disc is varying more than the power-law on longer time-scales. Alternatively, there could be power-law spectral variability that applies only on longer time-scales and causes the soft band variability amplitude to be enhanced, i.e., due to steepening of the power-law spectral slope on longer time-scales. To determine the origin of the extra low-frequency power in the soft band, a spectral analysis of the variations on different time-scales must be carried out, the methodology for which I describe in the next section.

---

[4] Specifically, containing 131072 time bins.

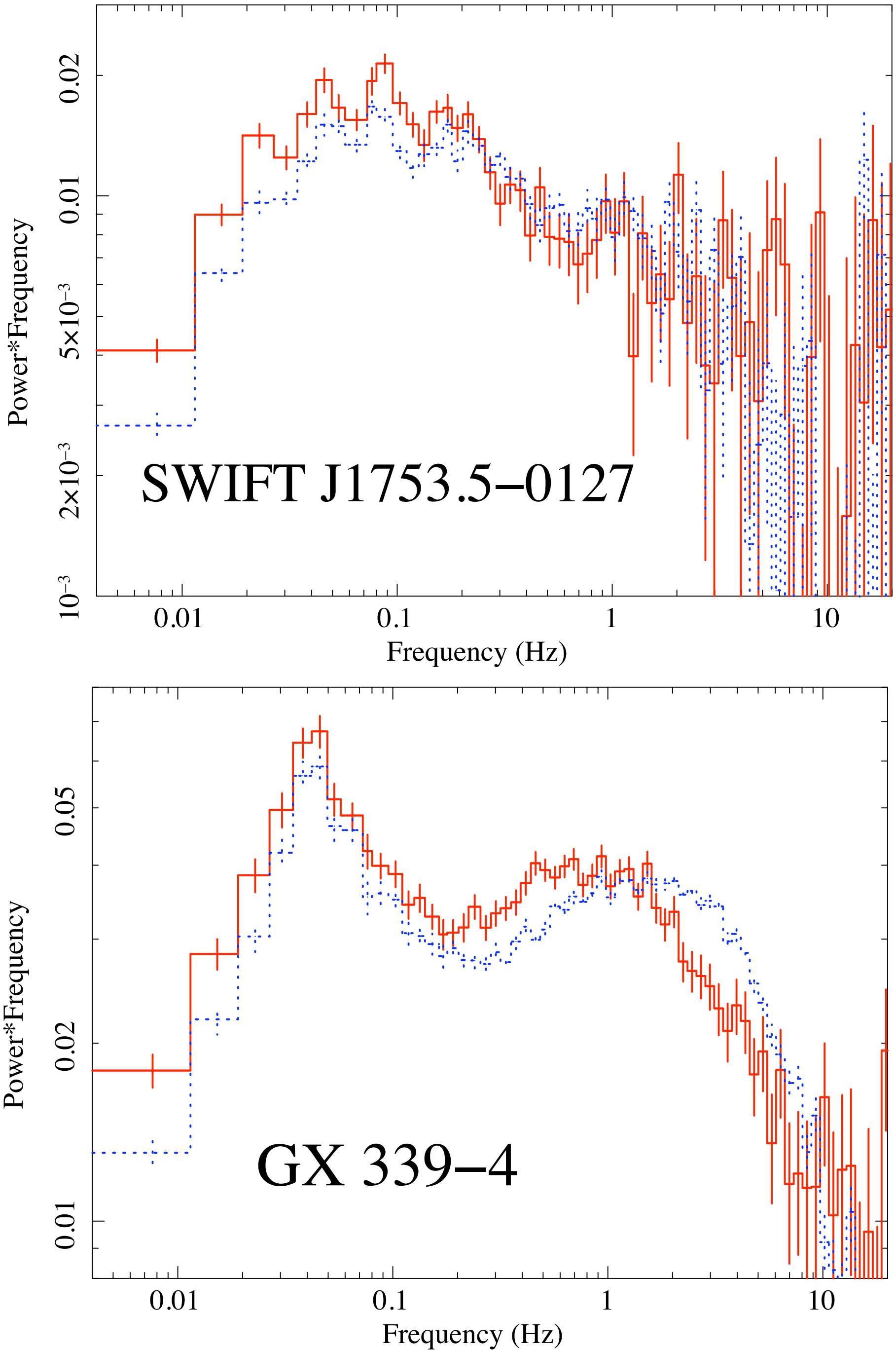

Figure 2.1: Soft and hard band PSDs for SWIFT J1753.5-0127 and GX 339-4. The solid line denotes the 0.5-1 keV PSD, while the dotted line denotes the 2-10 keV PSD. The Poisson noise component has been subtracted from all PSDs.

2.3.2 Methodology: rms and covariance spectra

When fitting models to X-ray spectra, it is typical to use mean X-ray spectra that only describe the time-averaged spectral shape of a source. Such fits say nothing about the way the different spectral components such as disc blackbody and power-law vary with respect to each other in time. By looking at the absolute amplitude of variations in count rate as a function of energy one can construct 'variability spectra' which pick out only the time-varying components. One technique is to construct Fourier-frequency resolved spectra, obtaining a PSD for each individual energy channel and integrating the PSD over a given Fourier-frequency range in order to measure the variance in that channel, which is used to obtain the rms and so construct the spectrum due to components which vary over that frequency range (e.g. Revnivtsev, Gilfanov & Churazov 1999). This approach is attractive in that it allows the user to pick out complex patterns of spectral variability where components have different time-scales of variation, as may be implied by the soft and hard band PSDs shown in figure 2.1. Here I will consider only two time-scales of variability, corresponding roughly to the high and low-frequency parts of the PSD which show significant relative differences between the soft and hard bands. To approximate the more complex Fourier-resolved approach I will measure over two time-scale ranges a variant of the 'rms spectrum', which measures the absolute Root-Mean-Squared variability (rms) as a function of energy (e.g. see Vaughan et al. 2003).

Producing the rms spectrum involves allocating each photon event to a time and energy bin, dividing the light curve into segments consisting of N time bins per segment and then working out the variance in each segment for each energy bin according to the following standard formula:

$$\sigma_{\mathrm{xs}}^2 = \frac{1}{N-1}\sum_{i=1}^{N}(X_i - \bar{X})^2 - \overline{\sigma_{\mathrm{err}}^2} \tag{2.1}$$

where X_i is the count rate in the i^{th} bin and $\bar{X}$ is the mean count rate in the segment. The expectation of Poisson noise variance, given by the average squared-error $\overline{\sigma_{\mathrm{err}}^2}$, is subtracted, leaving the 'excess variance', σ_{xs}^2, in each segment. The excess variances can then be averaged over all of the segments of the light curve. The square root of the average excess variance plotted against energy forms the rms spectrum[5]. By selecting the time bin size and the segment size, different time-scales of variability can be isolated, effectively replicating the Fourier resolved approach for the two

---

[5] This is absolute rms, since this is not normalised by the mean count rate.

time-scale ranges of interest. For this purpose, I chose two combinations of bin size and segment size. To look at variations on shorter time-scales I chose 0.1 s time bins measured in segments of 4 s (i.e., 40 bins long), i.e., covering the frequency range 0.25-5 Hz[6]. For longer time-scale regions I use 2.7 s bins in segments of 270 s, i.e., covering the range 0.0037-0.185 Hz. Note that these two frequency ranges do not overlap and also cover the two parts of both source PSDs which show distinct behaviour in soft and hard bands.

There is, however, a problem with the rms spectrum when signal to noise is low, e.g. at higher energies. It is possible for the expectation value of the Poisson variance term to be larger than the measured average variance term, producing negative average excess variances. If this is the case, it is not possible to calculate the rms at these energies and this introduces a bias towards the statistically higher-than-average realisations of rms values, which can still be recorded. In order to overcome these problems Phil Uttley and I developed a technique called the ‘covariance spectrum’. The covariance is calculated according to the formula:

$$\sigma^2_{\rm cov} = \frac{1}{N-1}\sum_{i=1}^{N}(X_i - \bar{X})(Y_i - \bar{Y}) \tag{2.2}$$

where Y_i now refers to the light curve for a ‘reference band’ running over some energy range where the variability signal-to-noise is large. In this work, I use reference bands of 1–4 keV for EPIC-pn data and 3–5 keV for PCA data. In other words, the covariance spectrum is to the rms spectrum what the cross-correlation function of a time series is to its auto-correlation function. The covariance spectrum therefore does not suffer from the same problems as the rms spectrum, as no Poisson error term has to be subtracted, since uncorrelated noise tends to cancel out and any negative residuals do not affect the calculation. To remove the reference band component of the covariance, and produce a spectrum in count-rate units, one obtains the normalised covariance for each channel using:

$$\sigma_{\rm cov,norm} = \frac{\sigma^2_{\rm cov}}{\sqrt{\sigma^2_{\rm xs,y}}} \tag{2.3}$$

where $\sigma^2_{\rm xs,y}$ is the excess variance of the reference band. Therefore, the only requirement for there being a valid, unbiased value of covariance at a given energy is that the reference excess variance is not negative. This is usually the case, since

---

[6] The upper frequency limit is set by the Nyquist frequency, $\nu_{\rm Nyq} = 1/(2\Delta t)$ where Δt is the time bin size.

the reference band is chosen to include those energies with the largest absolute variability. When the covariance is being calculated for an energy channel inside the reference band, the channel of interest is removed from the reference band. The reasoning behind this is that if the channel of interest is duplicated in the reference band, the Poisson error contribution for that channel will not cancel and will contaminate the covariance. One can think of the covariance technique as applying a matched filter to the data, where the variations in the good signal-to-noise reference band pick out much weaker correlated variations in the energy channel of interest that are buried in noise. In this way the covariance spectrum picks out the components of the energy channel of interest that are correlated with those in the reference band.

It is important to note that the covariance spectrum only picks out the correlated variability component and is therefore a more appropriate measure than the rms spectrum in constraining the reprocessing of hard photons to soft photons, which will result in correlated variations. When the raw counts rms and covariance spectra are overlaid, as in figure 2.2, they match closely indicating that the reference band is well correlated with all other energies (the spectral 'coherence' is high, e.g. see Vaughan & Nowak 1997). Another advantage of the matched filter aspect of the covariance spectrum is that it leads to smaller statistical errors than the rms spectrum. Specifically, the errors are given by:

$$Err\left[\sigma_{\mathrm{cov,norm}}\right] = \sqrt{\frac{\sigma^2_{\mathrm{xs,x}}\overline{\sigma^2_{\mathrm{err,y}}} + \sigma^2_{\mathrm{xs,y}}\overline{\sigma^2_{\mathrm{err,x}}} + \overline{\sigma^2_{\mathrm{err,x}}}\;\overline{\sigma^2_{\mathrm{err,y}}}}{NM\sigma^2_{\mathrm{xs,y}}}} \tag{2.4}$$

where M denotes the number of segments and subscripts x and y identify excess variances and Poisson variance terms for the channel of interest and reference band respectively. This error equation can be derived simply from the Bartlett formula for the error on the zero-lag cross-correlation function, assuming that the source light curves have unity intrinsic coherence (Bartlett, 1955; Box & Jenkins, 1976). By comparison with equation B2 of Vaughan et al. 2003 which is derived in appendix B, using the relation:

$$\frac{\overline{\sigma^2_{\mathrm{err,y}}}}{\sigma^2_{\mathrm{xs,y}}} << \frac{\overline{\sigma^2_{\mathrm{err,x}}}}{\sigma^2_{\mathrm{xs,x}}} \tag{2.5}$$

(which is true because the reference band has good signal to noise) it can be shown that the errors on the covariance are smaller than corresponding errors on the rms values.

Finally, it should be noted that, since the covariance is analogous to the zero-

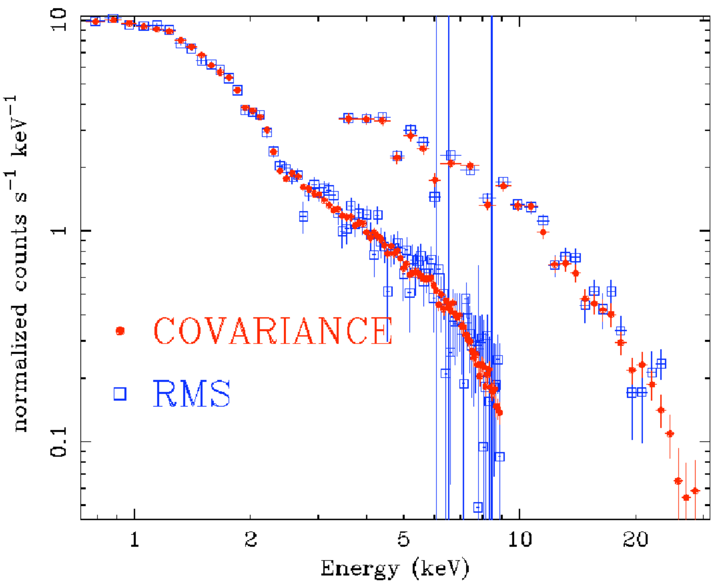

Figure 2.2: Overlaid covariance and rms spectra for EPIC-pn and PCA data of SWIFT J1753.5-0127 covering the frequency range 0.0037-0.185 Hz. The large error bars in the EPIC-pn data indicate negative excess variances where no rms value could be determined.

lag cross-correlation function, it could be affected by intrinsic time lags in the data. Using measurements of the cross-spectral phase-lags between various energy bands, it was confirmed that the lags between hard and soft band variations are smaller than the time bin sizes used to make the long and short time-scale covariance spectra. Thus, intrinsic time lags will have a negligible effect on our results.

2.3.3 SWIFT J1753.5-0127

I first consider the covariance spectra of SWIFT J1753.5-0127, and use XSPEC V12[7] (Arnaud, 1996) to fit the long and short-time-scale data together with the mean spectrum in order to identify the origin of the additional long-time-scale variability which can be seen in the soft band PSD. The covariance spectra do not show sufficient signal-to-noise to detect the rather weak iron line present in the mean spectrum of this source (Hiemstra et al., 2009; Reis, Miller, & Fabian, 2009), so for simplicity only a simple power-law and multicolour disc blackbody DISKBB are fitted, together with neutral absorption. I fitted the short and long-time-scale covariance and mean spectra simultaneously, tying the absorbing column density and renormalising constant for PCA data to be the same for the mean and covariance spectra. An examination of the delta-chi-squared improvement showed that the disk blackbody temperature does not change significantly between spectra, so that was also tied to

---

[7] http://heasarc.gsfc.nasa.gov/xanadu/xspec/

be the same for all spectra. The remaining parameters were allowed to be free between the covariance and mean spectra. For those parameters that were free to vary, EPIC-pn and PCA values were tied together. The χ^2 of the final fit was 1802 for 1948 degrees of freedom (d.o.f.) and full fit parameters are listed in Table 2.1. The best-fitting unfolded spectra and the corresponding data/model ratios are shown in figure 2.3.

To interpret the fits to the covariance spectra, consider the case where the observed PSDs have identical shapes in both hard and soft bands (they may have different normalisations). In this case, the ratio of soft to hard-band variability amplitudes measured over the same time-scale range will be identical for any given time-scale range. Therefore, since (for high-coherence variations) the covariance spectrum quantifies variability amplitude as a function of energy, the shape of the covariance spectrum will be independent of time-scale. On the other hand, if the soft band contains more long-time-scale variability relative to short-time-scale variability than the hard band, the long-time-scale covariance spectrum will appear *softer* than the short-time-scale covariance spectrum: lower energies show correspondingly greater variability on long time-scales and therefore larger fluxes in the covariance spectra. Just such an effect is seen in the model fits to the covariance spectra: the long-time-scale covariance spectrum is softer than the short-time-scale covariance spectrum, because the disc blackbody normalisation is higher on long time-scales. The power-law slope is remarkably similar on both long and short time-scales however. Therefore the additional long-term variability in the soft-band PSD seems to result from *additional* variability of the disc blackbody, not any extra power-law variability (e.g. due to spectral pivoting).

It can be shown in a model-independent way that the blackbody component is the source of the additional long-term variability seen in the soft-band PSD, by measuring the ‘covariance ratio’, i.e., plotting the ratio of long-time-scale to short time-scale covariance spectra. By plotting the ratio, most of the effects of the spectral response can be removed (except the smearing by the instrumental resolution) and one can see more clearly the nature of any spectral differences. The covariance ratio plot is shown in figure 2.4, and shows clearly that the excess in long-time-scale covariance arises abruptly below 2 keV, as expected if caused only by the disc emission, rather than being due to a gradual change across the whole spectrum which might be caused by differences in the power-law index. The interpretation of the short time-scale covariance spectrum is addressed later in section 3.7.

Having established that the reference band is well correlated with all other energies, the normalisations of the covariance spectral components, given in Table 2.1,

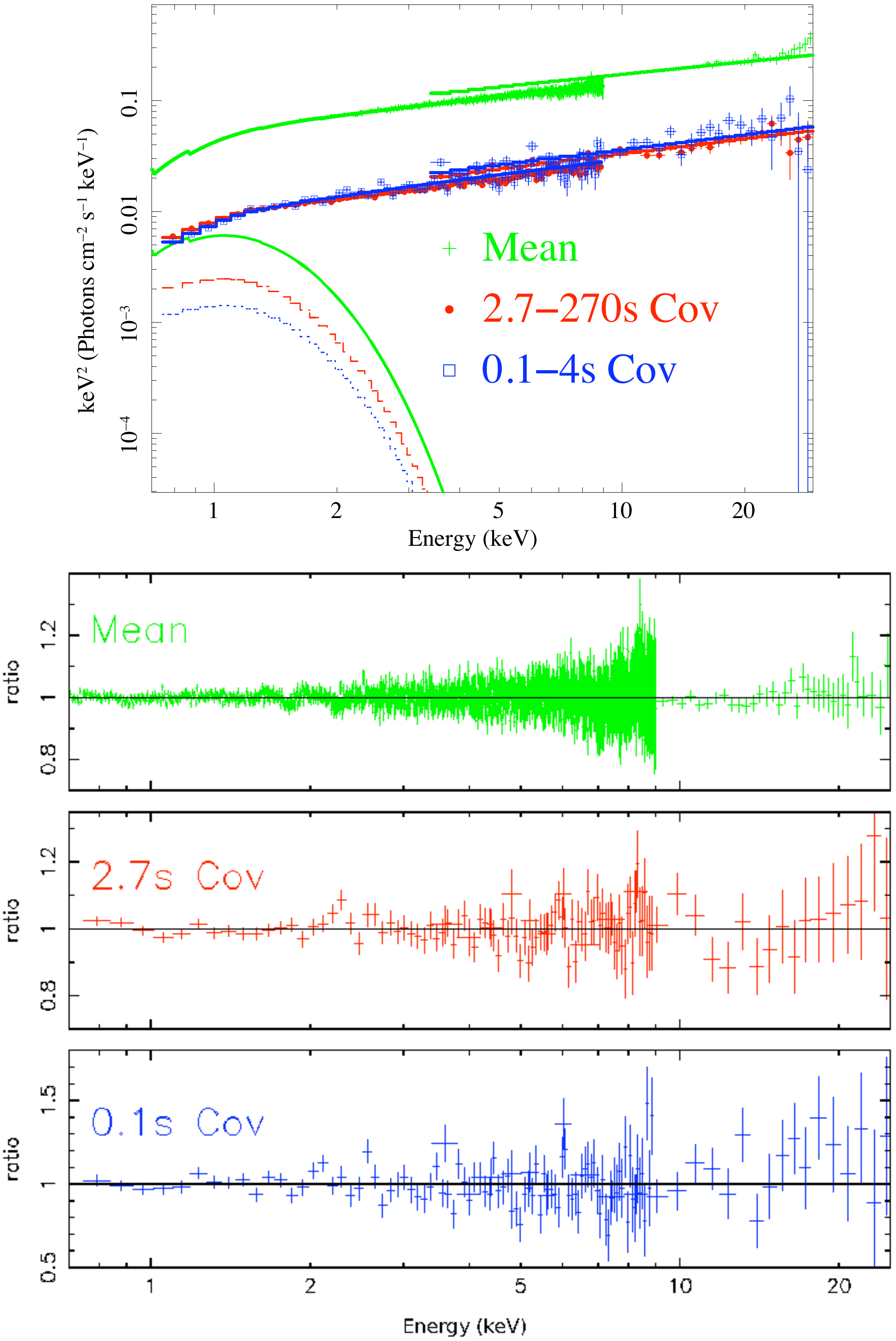

Figure 2.3: Top panel: Unfolded spectra for SWIFT J1753.5-0127 showing the relative contributions of the disc blackbody and power law components in the mean spectrum and short and long-time-scale covariance spectra. Dotted lines indicate spectral components of the short time-scale covariance, dashed lines indicate those of the long time-scale covariance. Bottom panel: SWIFT J1753.5-0127 data/model ratios for the best-fitting disc blackbody plus power-law model.

Table 2.1: Fit parameters for mean and covariance spectra of SWIFT J1753.5-0127 for the model CONSTANT*PHABS*(DISKBB+POWERLAW)

Parameter	Mean	2.7s-270s Cov	0.1s-4s Cov
$C_{\rm PCA}$	$1.222^{+0.006}_{-0.006}$	tied to mean	tied to mean
$N_{\rm H}$	$0.194^{+0.007}_{-0.006}$	tied to mean	tied to mean
Γ	$1.625^{+0.005}_{-0.005}$	1.55 ± 0.02	1.55 ± 0.03
$A_{\rm pl}$	$0.0731^{+0.0009}_{-0.0009}$	$0.0118^{+0.0004}_{-0.0004}$	$0.0128^{+0.0006}_{-0.0006}$
$kT_{\rm in}$	$0.286^{+0.015}_{-0.014}$	tied to mean	tied to mean
$A_{\rm disc}$	320 ± 25	129 ± 11	75 ± 20

From top to bottom, the parameters are: constant renormalising factor applied to model fit to PCA data; neutral absorbing column density (10^{22} cm^{-2}); power-law photon index; power-law normalisation (photons cm^{-2} s^{-1} keV^{-1} at 1 keV); disc blackbody inner radius temperature (keV); disc blackbody normalisation ($[r_{\rm in}/(D/10\ {\rm kpc})]^2$ where $r_{\rm in}$ is the disc inner radius in km and D is the distance in kpc). All errors are 90 per cent confidence limits. Since disc temperature and normalisation are highly correlated, the errors on blackbody normalisation are obtained while fixing temperature at the best-fitting value.

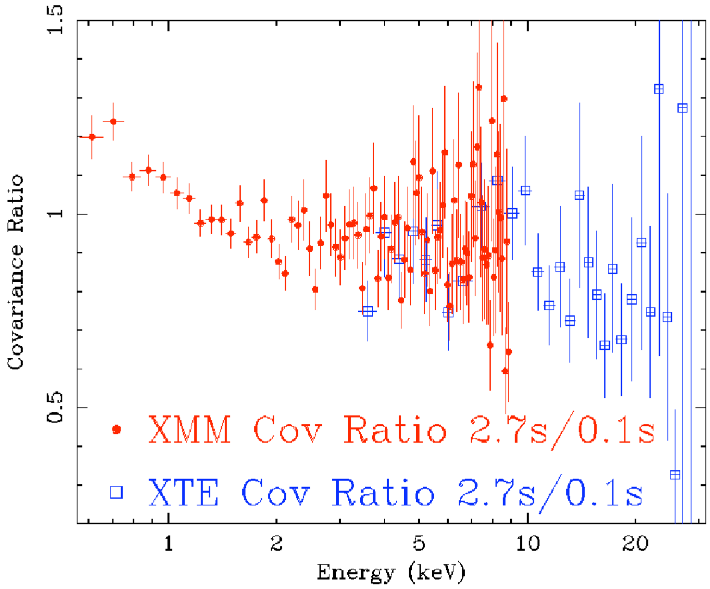

Figure 2.4: Covariance ratios for SWIFT J1753.5-0127 showing the extra black-body component which contributes on longer timescales.

relative to those of the mean spectrum indicate the rms variability amplitude. For example, dividing the disc blackbody covariance normalisations by that of the mean spectrum indicates fractional rms for the disc emission of 40 per cent and 23 per cent over long and short time-scale ranges respectively. The power-law variability is more complicated to quantify, since the covariance spectra show significantly harder power-law slopes than the mean. This result implies that the power-law fractional rms increases with energy. The power-law normalisations imply that at 1 keV the fractional rms of the power-law is 16 per cent and 18 per cent over the long and short time-scale ranges respectively.

2.3.4 GX 339-4

I next produced mean, long and short time-scale covariance spectra for EPIC-pn timing mode and PCA observations of GX 339-4. Fits were carried out to the spectra using a model consisting of a narrow Gaussian emission line (width $\sigma =$ 0.01 keV) and power law (including the multiplicative model HREFL to account for the reflected continuum from a cold optically thick disk), smeared with the convolution model KDBLUR in order to account for relativistic broadening of the reflected emission from material orbiting a maximally spinning black hole (see Reis et al. 2008 for evidence for a high black hole spin in GX 339-4). A multicolour disc model DISKBB was also included to account for the soft X-ray excess. Strictly speaking this component should also be smeared, but it is not appropriate to smear this model with KDBLUR, as the disc temperature is itself a function of radius. Since in the KDBLUR model the disc innermost radius and iron line radial emissivity are somewhat degenerate, the emissivity index was fixed at -3 (i.e., disc-like). Also, the outer radius was fixed at 400 $R_{\rm G}$. The remaining parameters, except the black body normalisation, reflection covering fraction, photon index, power law normalisation and Gaussian normalisation were tied to be the same between the mean and both covariance spectra (I confirmed with F-tests that the tied parameters do not vary significantly between the spectra). As with SWIFT J1753.5-0127, the EPIC-pn and PCA parameters were tied together for the same spectra and a renormalising constant factor was included to allow for differences in EPIC-pn and PCA flux calibration. The final fit had a χ^2 of 2489 for 2199 d.o.f. and a full list of model parameters is given in Table 2.2. The best-fitting unfolded spectra and data/model ratios can be seen in figure 2.5.

The fits to the covariance spectra for GX 339-4 show a similar pattern to that seen for SWIFT J1753.5-0127, in that the long time-scale covariance spectrum is softer

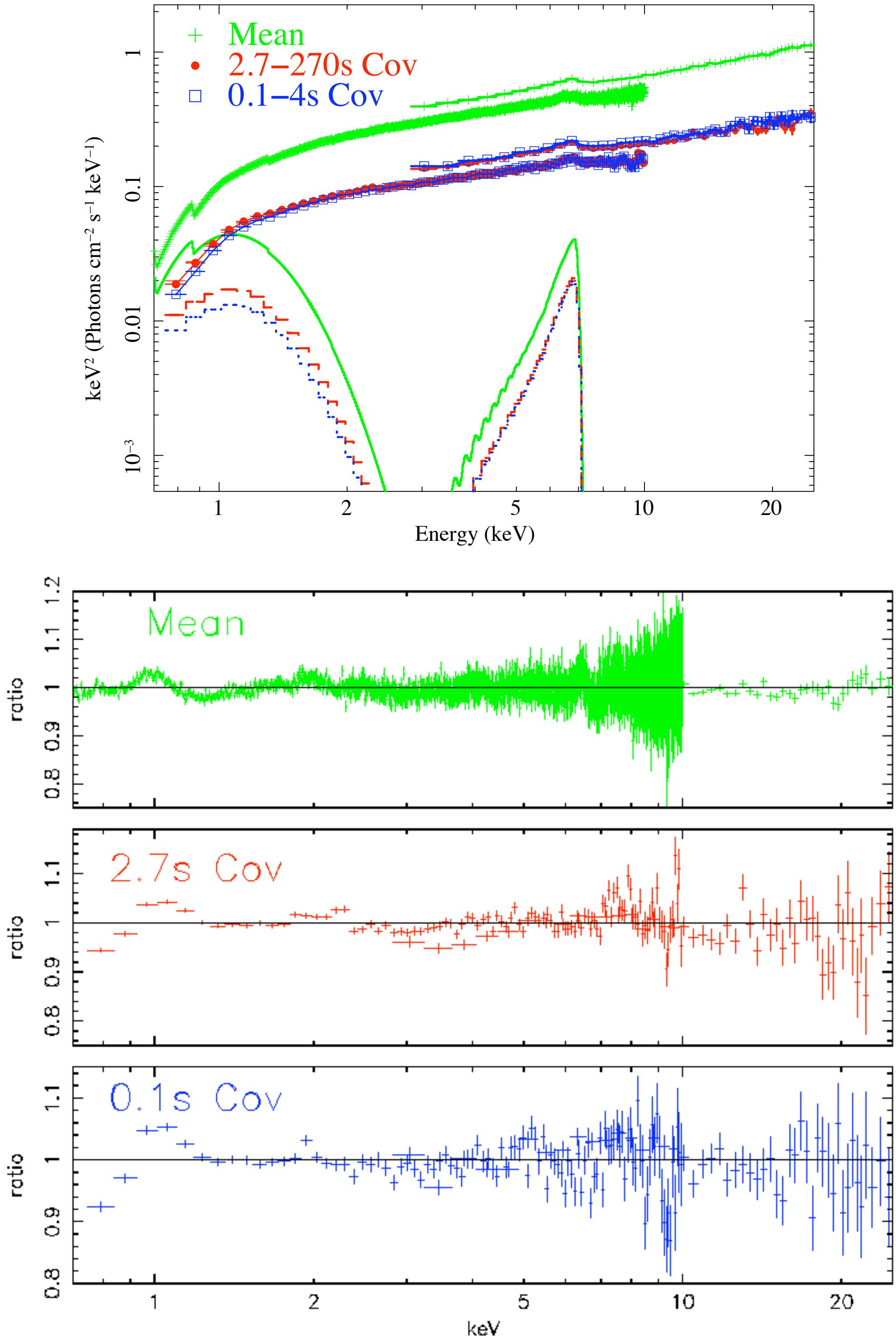

Figure 2.5: Top panel: Unfolded spectra fitted for GX 339-4 showing the relative contributions of the blackbody, power law (incorporating reflection continuum) and iron line components. Dotted lines indicate spectral components of the short time-scale covariance, dashed lines indicate those of the long time-scale covariance. Bottom panel: GX 339-4 data/model ratios for the best-fitting disc blackbody plus power-law and relativistically smeared reflection model.

Table 2.2: Fit parameters for mean and covariance spectra of GX 339-4 for the model CONSTANT * PHABS * (DISKBB+KDBLUR(HREFL * POWERLAW+GAUSSIAN))

Parameter	Mean	2.7s-270s Cov	0.1s-4s Cov
$C_{\rm PCA}$	1.296 ± 0.003	tied to mean	tied to mean
$N_{\rm H}$	0.574 ± 0.006	tied to mean	tied to mean
Γ	1.766 ± 0.006	1.896 ± 0.010	1.875 ± 0.011
$A_{\rm pl}$	0.266 ± 0.002	0.110 ± 0.001	0.107 ± 0.001
$kT_{\rm in}$	0.177 ± 0.001	tied to mean	tied to mean
$A_{\rm disc}/10^4$	8.20 ± 0.65	3.20 ± 0.26	2.46 ± 0.21
$R_{\rm in}$	4.08 ± 0.16	tied to mean	tied to mean
$\theta_{\rm inc}$	40.2 ± 1.4	tied to mean	tied to mean
$E_{\rm Fe}$	6.42 ± 0.07	tied to mean	tied to mean
$A_{\rm Fe}/10^{-3}$	1.17 ± 0.07	0.61 ± 0.07	0.58 ± 0.09
CF	0.91 ± 0.04	1.13 ± 0.08	1.16 ± 0.09

For the definitions of the parameters listed in the first six rows see Table 2.1. The additional parameters shown are for the relativistically smeared reflection (from top to bottom): disc innermost radius (units of $R_{\rm G}$); disc inclination (fixed to be the same in both KDBLUR and HREFL); Gaussian line energy; Gaussian normalisation (photons cm^{-2} s^{-1}); covering fraction of the reflection (where 1.0 corresponds to 2π steradians).

than the short time-scale covariance spectrum because of a significantly stronger disc blackbody component, while their power-law indices are very similar. This interpretation can be confirmed using a plot of the covariance ratio, which is shown in figure 2.6, and shows a similar rise at low energies to that seen for SWIFT J1753.5-0127, which underlines the interpretation that the disc blackbody component is the main contributor to the additional variability seen at low frequencies in the soft band in GX 339-4. Note that the apparent emission feature around 2 keV is an instrumental effect, related to inaccuracies in the Charge Transfer Inefficiency (CTI) correction model. Due to the 1 per cent systematic included in the spectral fitting, this feature has no major effect on the fit results.

Based on the ratio of component normalisations to those in the mean spectrum, the fractional rms values for the disc component are 39 per cent and 30 per cent over the long and short time-scale ranges respectively. The corresponding power-law fractional rms values at 1 keV are 41 per cent and 40 per cent. Using the same

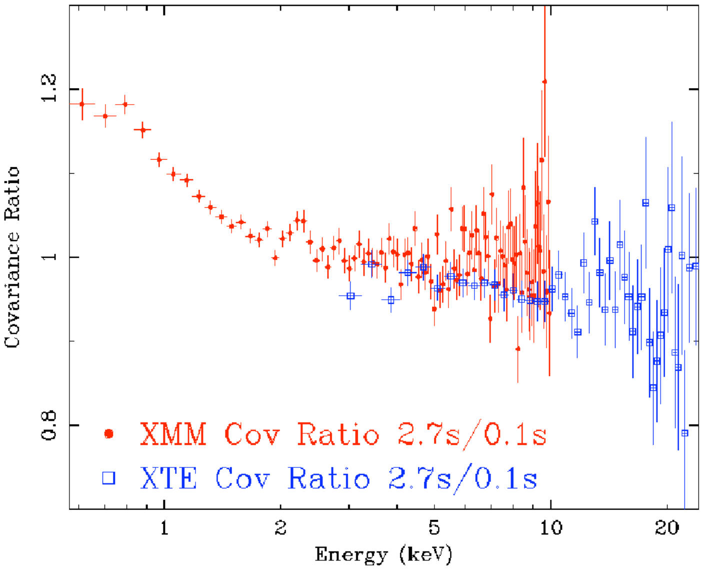

Figure 2.6: Covariance ratios for GX 339-4 showing the extra thermal component on longer timescales

approach, the fractional rms for the iron line emission can be defined for long and short time-scales, at $\sim$ 50 per cent in each case. Interestingly, the $\sim$ 25 per cent increase in iron line rms over that of the power-law emission (which drives the line variability) is comparable to the increase in reflection covering fraction from the mean to covariance spectra. These results may imply the presence of an additional constant power-law component which dilutes the power-law fractional variability but does not contribute to reflection. It is also interesting to note that the power-law component in the covariance spectra for GX 339-4 is softer than in the mean spectrum, i.e., the difference is in the opposite sense to that seen in SWIFT J1753.5-0127.

2.4 Discussion

I have shown that disc blackbody emission contributes significantly to the X-ray variability spectra in the hard state of the black hole candidates SWIFT J1753.5-0127 and GX 339-4, and moreover, that the disc emission is the origin of the additional soft band variability seen on longer time-scales in both sources, which manifests itself as an enhanced low-frequency component in the PSD. In this section, I discuss the evidence for a connection between disc and power-law variability through X-ray reprocessing, and then consider two possible explanations for the enhanced disc variability on long time-scales, in terms of geometry changes or fluctuations intrinsic to the accretion disc. Finally I will compare my results and interpretation to the wider picture of different accretion states.

2.4.1 Power-law variability and evidence for thermal reprocessing

The power-law emission clearly dominates the X-ray luminosity in both sources, as can be seen in figures 2.3 and 2.5. In this situation, if the disc sees a reasonable fraction of the power-law emission, one should expect that X-ray heating of the disc, i.e., thermal reprocessing of power-law emission, will produce a significant fraction of the observed disc luminosity. In fact, the thermal reprocessed emission is directly related to the disc reflection component in the spectrum: if a fraction of incident power-law luminosity f is reflected by the disc (both through Compton reflection and emission line fluorescence), then a fraction $1-f$ must be absorbed and will be reprocessed into thermal blackbody radiation. The reflected fraction f depends on disc ionisation state but simple exploration of the disc reflection models in XSPEC shows that it is typically 30-40 per cent of the incident luminosity, so that around 60-70 per cent of the incident luminosity is reprocessed into disc blackbody emission. For typical iron Kα line equivalent widths (around 1 keV with respect to the reflection continuum), the expected line flux is of the order 1 per cent of the thermally reprocessed flux. It is reasonable to assume that the blackbody component in the short time-scale covariance spectrum is produced by thermal reprocessing of the varying power-law, which also drives the line emission in the same spectrum. The unabsorbed disc flux is $\sim 4.5\times10^{-10}$ erg cm^{-2} s^{-1}, and the iron line flux is $\sim 6\times10^{-12}$ erg cm^{-2} s^{-1} which is 1.3 per cent of the reprocessed flux, i.e., consistent with a reprocessing origin for the thermal emission, at least on short time-scales.

In SWIFT J1753.5-0127, the disc blackbody emission is considerably weaker than in GX 339-4, and correspondingly a relatively weak iron line would be expected, with a few tens of eV equivalent width, which is only just consistent with the lower-limits on line strengths reported by Hiemstra et al. (2009) and Reis, Miller, & Fabian (2009). It is possible that the disc in SWIFT J1753.5-0127 is substantially ionised (e.g. see Reis, Miller, & Fabian 2009) which would reduce the photoelectric cross section at lower energies and therefore enhance the higher energy line emission relative to the lower energy absorbed (and hence thermally reprocessed) emission.

Since it is likely that there is substantial X-ray heating of the disc, one must interpret the observed blackbody normalisations in the mean spectra with caution[8]. The disc emissivity may be more centrally concentrated than the theoretically expected R^{-3} law, and so the normalisations indicate better the emitting surface area and cannot be simply translated to an inner radius. Nonetheless, the inferred emitting areas are still relatively small, implying distance scales of tens to hundreds of km (assuming distances > 7 kpc and 6-15 kpc for SWIFT J1753.5-0127 and GX 339-4 respectively; Zurita et al. 2008; Hynes et al. 2004). Note also here that although the need for disc blackbody emission to explain the spectrum of SWIFT J1753.5-0127 has been questioned by Hiemstra et al. (2009), the model-independent covariance ratio plots in figure 2.4 show that a distinct soft component must be present in order to explain the difference in the shapes of the covariance spectra.

It is interesting to note that the power-law indices of the covariance spectra are different from those of the mean spectra, but in an opposite sense for each of the two sources considered here: compared to the mean spectrum, SWIFT J1753.5-0127 shows a harder power-law in the covariance spectra, while GX 339-4 shows a softer power-law. The difference may be caused by flux-dependent spectral pivoting or steepening, so that as flux increases the spectrum gets softer in GX 339-4, increasing the covariance at soft energies relative to the mean, while the opposite effect occurs in SWIFT J1753.5-0127 (it hardens as it gets brighter). The difference in behaviour may be related to the source luminosity: if they lie at similar distances SWIFT J1753.5-0127 is at least a factor 10 less luminous than GX 339-4, implying a significantly lower accretion rate. Correlations between flux and spectral-hardness have been seen in BHXRB hard states, and interestingly the sign of the correlation appears to switch over from negative to positive at low luminosities, both on short time-scales (Axelsson et al., 2008) and in the long-term global correlation (Wu & Gu, 2008). The same switch in flux-hardness correlation could be related to the different power-law behaviours of SWIFT J1753.5-0127 and GX 339 which are seen here.

The same pattern appears on both long and short time-scales, which show almost identical power-law indices in their covariance spectra, so that the effect of the power-law spectral variability will be to change the normalisation of the PSD, but not the shape. Since most of the power-law luminosity will be found at tens of keV (assuming a thermal cutoff at around 100 keV), spectral steepening with increasing flux will cause the observed GX 339-4 0.5-10 keV variability amplitude to be enhanced compared to the true luminosity variations. Conversely, observed

---

[8] The absolute normalisation in the covariance spectra is a function of variability amplitude and cannot be interpreted in the same way as in the mean spectrum.

variations in SWIFT J1753.5-0127 will be smaller than the total luminosity variations. Therefore, the fractional luminosity variations for SWIFT J1753.5-0127 and GX 339-4 may be similar, but GX 339-4 shows a significantly greater normalisation in the PSDs shown in figure 2.1.

2.4.2 Variable coronal geometry

It is likely that reprocessing of the power-law drives at least some of the disc variability seen in hard state sources, and possibly all of it on time-scales < 1 s. However, model-independent covariance ratio plots and spectral fitting show that the covariance spectra of both sources demonstrate increased disc blackbody variability with respect to the power law on longer timescales. There are several possible explanations for this pattern, but the key thing that any successful model needs to achieve is an increase in disk variability on longer timescales without a concomitant rise in power law variability. Also, it is important to note that the additional disc variability must still be correlated with power-law variations, because the enhanced disc variations appear in the covariance spectrum, which is identical to the rms spectrum over the high signal-to-noise energy range covered by the disc (i.e., coherence is unity). If the disc variations were independent of the power-law they would cancel to some extent, since they would be uncorrelated with the power-law component, and covariance would be smaller than the rms. Thus the blackbody variations map on to power-law variations but with larger amplitude.

One possibility is to change the geometry of the system on longer time-scales. For example, a variable coronal scale height on longer timescales could lead to changes in the solid angle of disc heated by the power-law, thus increasing the disc blackbody variability amplitude relative to the power-law. Weaker correlated power-law variation could then be produced if scale-height correlates with power-law luminosity. Alternatively, correlated power-law variations could be due to variable seed photon numbers from the disc due to the enhanced variable heating, but in either case the additional power-law variability must be of smaller amplitude than the observed blackbody variability. Regardless of these model-dependent arguments, one can make a simple observational test of the variable-geometry model, by comparing the variability of reflection on long and short time-scales.

GX 339-4 shows significant reflection features in its covariance spectra, so any variation in coronal geometry should manifest itself as increased variability in the reflection components as the disk sees the varying power law. However, the spectral fit parameters given in Table 2.2 indicate that there is little change in reflection

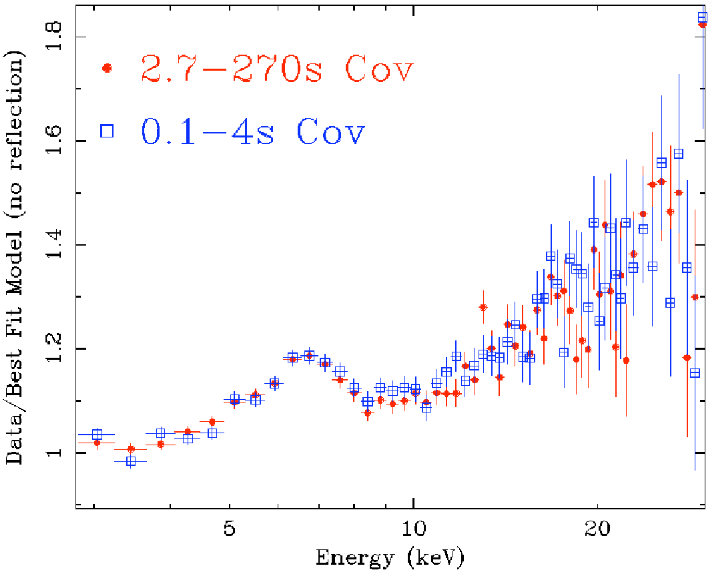

Figure 2.7: Data to model ratios of covariance spectra in GX 339-4 with reflection normalisations set to zero

amplitude between long and short time-scales, both in terms of reflection covering fraction and iron line equivalent width (e.g. ratio of line flux to power-law normalisation, which is meaningful because the power-law indices are so similar). To highlight this similarity in the covariance spectra, I show in figure 2.7 the data/model ratios for the PCA spectra with the reflection components taken out of the fit. The spectra demonstrate no significant change in the reflection continuum and associated iron line. This implies that if there is any change in geometry, it is small, and the increase in the thermal component of the variability spectra on longer timescales has a different origin.

To place this result on a more rigorous statistical footing, I show in figure 2.8 a contour plot of the best-fitting short and long-time-scale reflection covering fractions, which are obtained only from fits to the PCA data, which are most sensitive to the reflection continuum[9]. If variable geometry is the cause of the enhanced long-term blackbody variability, one would expect the covering fraction to show a similar enhancement in variability on long time-scales. The dashed line in the figure shows the largest ratio of short-to-long-time-scale covering fraction which crosses the 99 per cent confidence contour, with a value of 0.81, placing a 99 per cent confidence upper limit of 23 per cent on any increase in the covering fraction on long time-scales compared to short time-scales (the 90 per cent confidence upper limit

---

[9] As a result, the best-fitting covering fraction is significantly lower than observed in the joint fit with EPIC-pn, but since I am interested in the *relative* change in reflection between different time-scales, this does not affect the basic result.

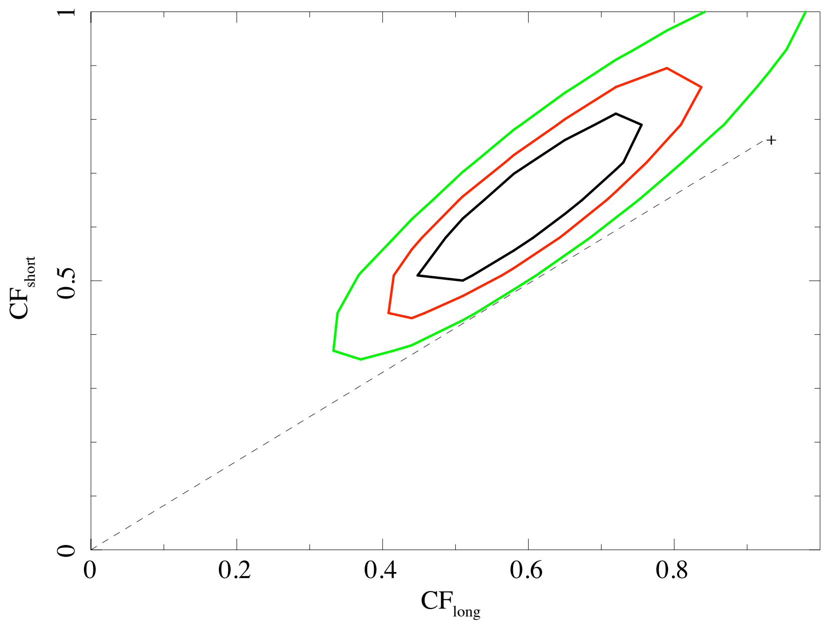

Figure 2.8: GX 339-4 confidence contour plots for the permitted range of reflection covering fraction in simultaneous fits to the long and short-time-scale covariance spectra. The dotted line passes through the 99 per cent confidence contour, so its gradient defines an upper limit to the ratio of long to short-time-scale covering fraction. Also shown are the 90 and 68 per cent confidence level contours.

on any increase is 12 per cent). In contrast, the long-time-scale blackbody variability amplitude increases by 30 per cent compared to that on shorter time-scales, which cannot be explained by the permitted increase in variable reflection at greater than the 99 per cent confidence level. Thus, in GX 339-4 at least, one can rule out long-time-scale changes in coronal geometry as a viable explanation for the enhanced blackbody variability amplitude. Note also that the same arguments apply to any other non-geometric arguments which seek to produce the extra long-term disc variability by varying the power-law contribution as seen by the disc, e.g through variable beaming of the power-law towards the disc. Due to the weakness of the iron line in SWIFT J1753.5-0127 it is not possible to place similar constraints on coronal geometry changes in this source, although by analogy it is expected that the same interpretation should apply.

2.4.3 Intrinsic disc variability

Having established that variable coronal geometry cannot explain the extra blackbody variability on longer timescales, an alternative possibility is that the variations are intrinsic to the disc itself. Perhaps the simplest possibility is that the fluctuations are due to accretion rate fluctuations in the disc which undergo viscous damping before they reach the corona. Such damping is expected in thin discs (e.g. see Churazov et al. 2001), but will not be as significant in geometrically thick flows, which might correspond to the corona. Therefore one can envisage that the long time-scale variability, e.g. corresponding to the low-frequency Lorentzian in the PSD, is generated in the thin disc, producing relatively large amplitude blackbody variations but being damped before reaching an inner coronal emitting region (perhaps inside the innermost radius of the thin disc). The correlated power-law variability could then arise either from the residual undamped variations in accretion rate which reach the corona, or be driven by seed photon variations from the disc.

If the inner radius of the disc were to fluctuate on long time-scales, then the varying disc area would also introduce extra blackbody variability. This model is in some sense analogous to that of changes in coronal scale height, since any change in disc area will vary the solid angle of disc seen by the corona which will cause an increase in reflection as well as correlated power-law variability driven by seed photon variations. One could mitigate these effects if the coronal properties were linked to those of the disc inner-radius, e.g. as inner radius decreases, so does coronal scale-height. This situation might be expected if the corona is formed by evaporation of the disc (Meyer-Hofmeister & Meyer, 2003), so that condensation of the disc will drain and cool the coronal plasma, leading to a reduction in scale-height.

2.4.4 Wider implications

I have established that the hard-state variability on time-scales greater than seconds, corresponding to the low-frequency Lorentzian PSD component, is very probably produced by variations intrinsic to the accretion disc, perhaps in the form of propagating accretion rate fluctuations, as envisaged by Lyubarskii (1997) to explain the broad shapes of observed PSDs. These variations then manifest as weaker power-law variations, either through propagation of accretion fluctuations to the corona (Churazov et al., 2001), or through variations of seed photons from the disc, which are Compton up-scattered in the corona. On shorter time-scales, the blackbody variations are probably mostly produced by X-ray heating of the disc by the power-law, which is a required outcome of the X-ray reflection directly observed in these systems. The exact split between direct emission from intrinsic disc variations and X-ray heating is difficult to judge, since some residual intrinsic variations may remain on short time-scales, and X-ray heating will also contribute on long time-scales.

But in the case of intrinsic disc accretion fluctuations, the variable X-ray heating is itself a product of those fluctuations, and so any intrinsic disc variations on long time-scales must be large, at least comparable to the fractional rms of blackbody emission, i.e., 40 per cent in both sources.

It is interesting to contrast the large intrinsic disc variability in these hard state sources with that in the soft states, where the disc emission dominates the bolometric luminosity. The soft states are well-known for showing very weak, if any, variability (Homan et al., 2001), and the strongest variability which is seen, e.g. in Cyg X-1, is associated with the power-law, with the disc being remarkably constant (Churazov et al., 2001). Therefore it seems likely that hard state discs are inherently unstable compared to soft state discs. This difference may represent just another observable distinction between hard and soft states, but it is interesting to speculate that it may play a more primary role in creating the other observed differences, such as a strong corona and jet formation in the hard state. Certainly, it seems likely that intrinsic disc variability plays an important role in determining the PSD shape in the hard state. For instance, the low energy PSD of GRS 1915+105 in the χ-class hard intermediate state (Rodriguez et al., 2004) shows a low frequency component which disappears at higher energies, possibly indicating that this source is demonstrating intrinsic disc variability.

It is worth noting here that X-ray/optical studies of AGN also show evidence for reprocessing on short time-scales and intrinsic disc variations on longer time-scales (Uttley et al., 2003; Arévalo et al., 2008; Breedt et al., 2009). However these AGN are relatively luminous and radio-quiet and so are likely analogues of BHXRB soft states, perhaps indicating that disc-stability shows a mass-dependence, e.g. related to the transition between gas- and radiation-pressure dominated discs (Maccarone, Gallo & Fender, 2003).

The results strongly suggest that disc variations are responsible for the low-frequency component in the hard state PSD. A number of authors have suggested that the low-frequency Lorentzian corresponds to the viscous time-scale of the inner, truncation radius of the thin disc (e.g. Churazov et al. 2001; Done et al. 2007), a view which is consistent with our results. The higher-frequency PSD components may then be produced in the corona, which is likely to be geometrically thick so will show naturally shorter variability time-scales. The viscous time-scale scales with scale-height (H) over radius (R) as $(H/R)^2$. Assuming the ratio of disc scale-height to radius $H/R \sim \alpha \sim 0.1$ (where α is the viscosity parameter), the predicted inner disc radius corresponding to the observed low-frequency PSD peak around ~ 0.05 Hz is 15 $\mathrm{R_G}$ (see Done et al. 2007). However, this radius may be even smaller for smaller H/R, which would make the disc truncation radius consistent with the results from fits to the iron line (this work, and Reis et al. 2008; Reis, Miller, & Fabian 2009). However, in the latter case the corona would need to be very compact, or seed photon variations from intrinsic disc variability would modulate the power-law with a similar amplitude to the disc. In either case, assuming the disc is thin and that it varies on the viscous time-scale, its inner radius must be relatively small. Such a picture is different from earlier models for the hard state, where the disc is truncated at large radii and power-law emission is produced by a very extended corona or ADAF with H/R$\sim$1 (e.g. Esin, McClintock, & Narayan 1997).

2.5 Conclusions

Spectral fits to observations of BHXRB sources in the hard state show increasing evidence for both power law and black body components. In this work I have explored the hard-state variability of two sources with known soft excesses, SWIFT J1753.5-0127 and GX 339-4. My findings are summarised below.

- I have introduced a new spectral analysis technique, the covariance spectrum, which measures the correlated variability in different energy bands. This technique overcomes the problems of low signal-to-noise and bias associated with the rms spectrum and has smaller statistical errors.

- PSDs of the two sources demonstrate larger low-frequency power in the soft band.

- The longer time-scale (2.7-270 s) covariance spectra of both sources are softer than the short time-scale (0.1-4 s) covariance spectra, due to additional disc variability, i.e., extra disc variability occurs on longer time-scales without a concomitant rise in power law variability on such timescales. However, the coherence of the rms and covariance spectra show clearly that disc variations are not independent of the power law variations.

- The strength of reflection features that are detected in the short time-scale covariance spectra of GX 339-4 are consistent with the observed blackbody variations on those time-scales being driven by thermal reprocessing of the power-law emission absorbed by the disc. However, the reflection covering fraction and iron line equivalent width show little change between short and long time-scales, implying that additional reprocessing, due to coronal geometry change, is not responsible for the additional blackbody variability seen on longer time-scales.

- The extra blackbody variability seen on longer time-scales appears to be intrinsic to the accretion disc itself, giving rise to the extra low-frequency power in the PSD. This represents the first clear evidence that the low-frequency Lorentzian component in hard state PSDs is produced by disc variability. Models invoking damped mass accretion rate variations or oscillations in the disc truncation radius can satisfactorily explain the observed pattern of variability.
- The implication of such variations occurring in a thin disc on viscous timescales, is that the disc truncation radius is $< 20\ \mathrm{R_G}$.

This work highlights the importance of measuring spectral variability on a range of time-scales. Mean spectra, which describe the average properties of a source, provide no information on how different spectral components are related to one another as a function of time. By using the covariance spectra I have been able to disentangle the correlated spectral components in these two sources, identify thermal reprocessing as the mechanism by which variability is correlated in different bands, produce model-independent evidence for additional blackbody variability on longer time-scales and therefore associate intrinsic disc variability with the low frequency Lorentzian feature seen in hard-state PSDs.

Very recent work done by Phil Uttley (Uttley et al., 2011) looking at the lag vs. energy spectra, has shown that on timescales of seconds, disc variations lead power-law variations in four *XMM-Newton* EPIC-pn hard state observations. Figure 2.9 shows a lag vs. energy spectrum over the frequency range 0.125-0.5 Hz. This is generated by taking the cross spectrum with respect to a reference band of $\sim$0.5-10 keV as discussed in section 1.6.2. In this way the spectrum yields the relative (not absolute) lags between any two energies. It is clear from the figure that when the disc begins to dominate the variable spectra ($<$2 keV) there is a negative lag indicating that the disc leads the power-law. This is very strong evidence not only that the disc is intrinsically variable, but that it is also *driving* the power-law variations.

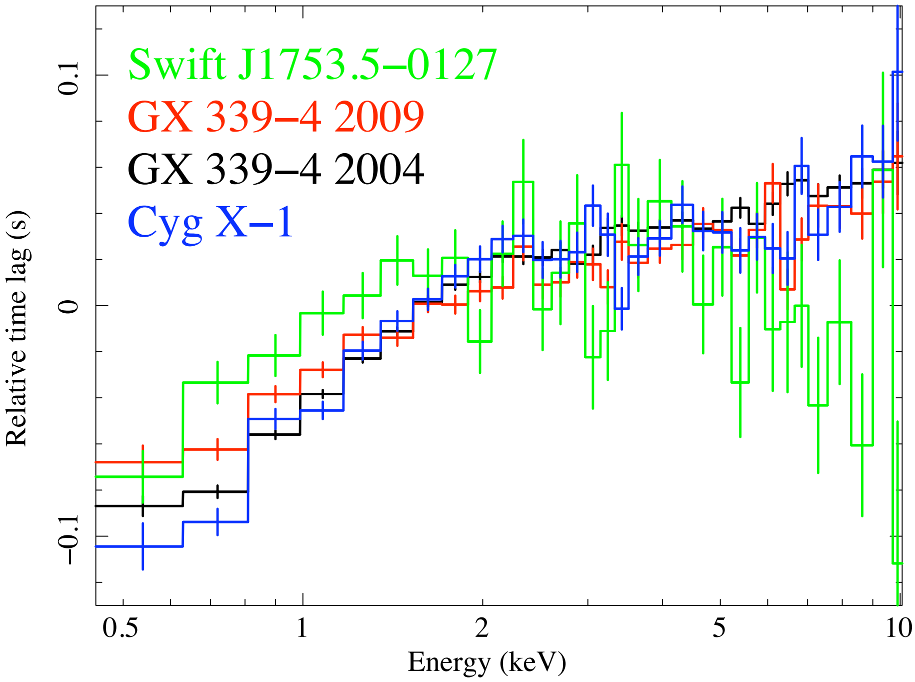

Figure 2.9: Lag vs Energy spectra over the frequency range 0.125-0.5 Hz for four hard-state observations of three different BHXRBs. All show a clear break to larger lags at energies ∼2 keV where the disc starts to dominate the variability spectrum.

Science is facts; just as houses are made of stone, so is science made of facts; but a pile of stones is not a house, and a collection of facts is not necessarily science.

JULES HENRI POINCARÉ (1854 - 1912)

3

GX 339-4 in 2004 and 2009: Using timing signatures to explore changes of truncation radius in the hard-state.

A common model for the hard-state of Black Hole X-ray Binaries (BHXRBs) suggests that the optically thick, geometrically thin accretion disc becomes more truncated as the source becomes harder (see section 1.5). At the same time, frequencies of the Lorentzian features in the Fourier power-spectrum decrease, suggesting that these frequencies are linked to characteristic time-scales in the inner disc. To test this interpretation of hard state behaviour as well as our understanding of broad iron lines, our group recently obtained an XMM-Newton TOO observation of the BHXRB GX 339-4 in its hard state, at a time when the low-frequency Lorentzian timing signature was 5 times lower in frequency than observed in a hard state observation of the source obtained in 2004. I present a detailed comparison of these spectra here, and discuss the implications for the disc truncation model.

3.1 Introduction

The truncated disc model provides a geometric argument explaining the spectral changes in BHXRBs together with the changing characteristic frequencies in the variability power-spectra of these sources. Recent evidence of thermal disc emission and broad iron lines in low/hard states (Rykoff et al., 2007; Miller et al., 2006; Miller, Homan, & Miniutti, 2006; Reis et al., 2008; Reis, Miller, & Fabian, 2009) have cast doubt on this model, suggesting that the accretion disc can, in fact, extend down to the last stable orbit in the hard state. This is a contentious point however, as some of the data used to argue in favour of a broadened iron-line in a rising hard-state observation of GX 339-4 may have been heavily piled up (Miller et al., 2006). A re-analysis of these data (Done & Diaz Trigo, 2009) concluded that the broad iron line was an artifact of pileup in the *XMM-Newton* MOS data. Furthermore, in this re-analysis, the simultaneous PN data was found to be much less piled up and gave a significantly narrower line consistent with *RXTE* PCA data. Recent simulations (Miller et al., 2010) indicate that severe pile-up can falsely narrow emission lines, however no attempt was made to model X-ray loading or Charge Transfer Inefficiency in this work and real data does not reproduce the predictions of this simulation (Maria Diaz-Trigo, private communication). It has also been argued that the broad red wing of the iron-lines in other hard-state observations of BHXRBs can be explained by absorption from an outflowing disc wind (Done & Gierliński, 2006) and any soft X-ray excess is a result of irradiation of the inner parts of the disc by hard X-rays (D'Angelo et al., 2008; Gierliński et al., 2008).

The PSD of the hard-state shows band-limited noise, which when plotted in $\nu \mathrm{P}(\nu)$ vs ν, typically demonstrates a flat region with $\mathrm{P}(\nu) \propto \nu^{-1}$ below which there is a 'break' where the power is $\propto \nu^{0}$. The PSD is better fitted by a series of 4 or 5 Lorentzian components (Psaltis, Belloni, & van der Klis, 1999), rather than a double broken power-law, the lowest of which forms this low-frequency break. It has been suggested that this break is associated with the truncation radius of the thin disc (Gilfanov, Churazov & Revnivtsev, 1999; Churazov et al., 2001) at the outer edge of the hot inner flow. Clearly then, to establish whether or not this break-frequency does track the truncation radius of the disc, two observations with different characteristic frequencies are required. This change of characteristic frequency in the PSD can then be compared to another independent measure of the inner radius. In an earlier paper (Wilkinson & Uttley, 2009) we examined the Lorentzian component which forms the low-frequency break in the PSD of GX 339-4 and showed that it was associated with intrinsic variability of the accretion disc. Having established that this feature is associated with the disc, it is reasonable to suppose that a change in the peak frequency of this Lorentzian component could be associated with a change in the disc truncation radius. Dynamical and viscous timescales are well-known functions of radius, so the change in Lorentzian peak-frequency between two observations can be used to predict a change in truncation radius. Spectral fitting to the iron-line can also provide a second, independent measure of the inner radius of the disc, since the line-shape is highly sensitive to the reflector's proximity to the black-hole.

This work therefore concentrates on two observations of the Low Mass X-ray Binary (LMXB) GX339-4. Hard state observations were taken with *XMM-Newton* in March 2004, and we later triggered a Target Opportunity Observation (TOO) in March 2009 when the low-frequency Lorentzian peak frequency was five times lower than in the 2004 observation. By comparing the broadening of the iron-line and the distinctly different timing signatures in these observations, I explore possible links between the low-frequency Lorentzian feature and the inner disc edge as the source transitions to an even harder state in the recent 2009 TOO.

3.2 Observations and Data Reduction

I analysed the 2004 March 16 and 2009 March 26 *XMM-Newton* EPIC-pn observations (OBS IDs 0204730201, 0204730301 and 0605610201) of the LMXB GX 339-4. I chose to use the EPIC-pn data, rather than the simultaneous MOS data, as it had been demonstrated in the months subsequent to my work in chapter 2 that the 2004 EPIC-pn data are not significantly piled up (Done & Diaz Trigo, 2009) because the highest count-rate data is excluded due to telemetry limitations.

The data were reduced in the standard manner using SAS 10.0.0, processing the ODF products using the SAS tools EPSPLITPROC and EPFAST, taking account of background flaring and extracting RAWX from columns 31 to 45 using the SAS tool EVSELECT. Although the tool EPFAST was used on the events file, the Charge Transfer Inefficiency[1] (CTI) corrections were insufficient to remove features at 1.8 and 2.2 keV (Si and Au edges) in the 2004 spectrum. Potential background regions from the 2004 and 2009 observations are strongly contaminated by the source, therefore a background spectrum was used for both observations from 2001 when the source was in quiesence (Maria Diaz-Trigo, private communication). The SAS tools ARFGEN and RMFGEN were used to generate the ancillary response file (ARF)

---

[1] This is the loss of some fraction of the signal charge which occurs during the read-out of the detector

and redistribution matrix file (RMF) for the 15 inner columns. The total exposure time for the combined 2004 data was 155 ks and for the 2009 data 31.7 ks. Note that the difference in total exposure time of the 2004 data between this chapter and chapter 2 is due to slightly less conservative background flaring selection. I grouped the EPIC-pn energy spectra using the PHARBN script of M. Guainazzi so that there was a minimum of three channels per resolution element (the instrumental resolution was over-sampled by a factor of three) and a minimum 20 counts per channel.

Our EPIC-pn spectral fits were restricted to the range 0.7 to 10.0 keV and all spectral analysis was performed using XSPEC version 12.6.0 (Arnaud, 1996).

3.3 Flux Selection

As also discovered by Done & Diaz Trigo (2009), the spectral index and flux are correlated in the 2004 PN data (though in an opposite manner to that expected as a consequence of pile up), so the brightest PN data excluded due to telemetry limitations are the softest. Apart from the significant difference in the power-spectra (figure 3.1) between the 2004 and 2009 observations, the flux of the 2009 observation is lower by a factor of $\sim$2. It is therefore conceivable that any differences in model parameters or spectral shapes could simply be flux related, and have nothing to do with complicated geometrical factors such as disc truncation. To account for this possibility, the 2004 data were split in to two rate-selected spectra which will be referred to as low-flux (0-300 cps) and high-flux (300-700 cps). The fluxes were chosen so that the lower flux subset of the 2004 data was similar to the flux of the 2009 data (strictly flux-matched spectra were also created but did not have sufficient signal-to-noise for full spectral analysis). The FTOOL TABGTIGEN was used to generate good time intervals (GTIs) (selecting on rate) from light curves with a bin-time of two seconds and the event files were then filtered with EVSELECT using these GTIs. All three data sets were fitted simultaneously, with the high-flux data used to further constrain changes in the inner radius, in case the inner radius changed as a function of flux.

3.4 Spectral Analysis and Results

Figure 3.1 shows power spectra of the 2004 and 2009 observations in the energy band 0.5-1.0 keV, demonstrating a clear shift by a factor of 5 in frequency of the low-frequency Lorentzian component. The dynamical and viscous timescales of

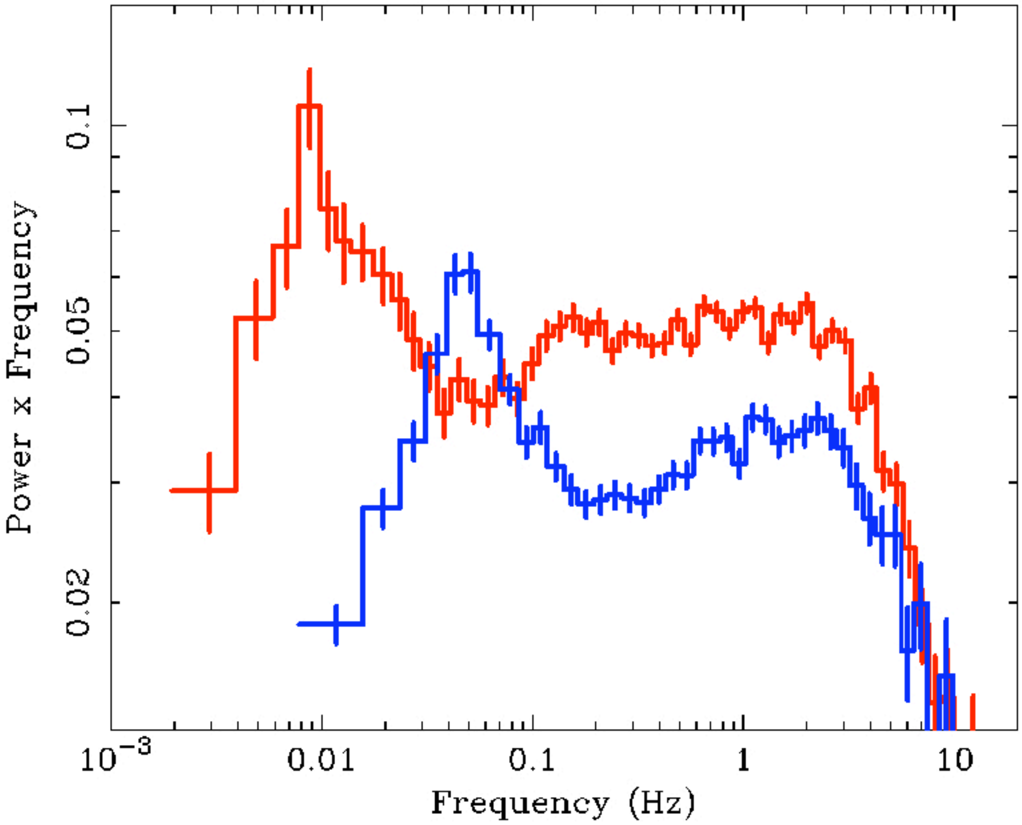

Figure 3.1: PSD showing the shift in the low-frequency Lorentzian timing signature from a peak of 0.05 Hz in 2004 (blue) to 0.01 Hz in 2009 (red). If this frequency change is associated with the inner disc radius, one would expect an increase in radius of approximately a factor 3 in the 2009 observation.

material accreting on to a Black Hole are both proportional to $R^{3/2}$. If this frequency change is related to changes in the truncation radius of the thin disc, and the assumption is made that the ratio of disc radius to disc scale height is unchanging, one would expect the inner radius of the disc in the 2009 observation to have receded by a factor of almost 3 relative to the 2004 value.

Figure 3.2 shows a ratio plot over the iron line region for all three data sets using the thermal Comptonisation model NTHCOMP fitted over 0.7-10.0 keV (see section 3.4.1 for a detailed explanation of this model component). The 6.4 keV core of the 2009 line profile is slightly broader than in 2004, and the similarity of the line red-wing shapes suggests that a large change in geometry, such as a factor of three change in the truncation radius as described above, is unlikely. I will explore the difference in disc parameters more quantitatively in the following sections.

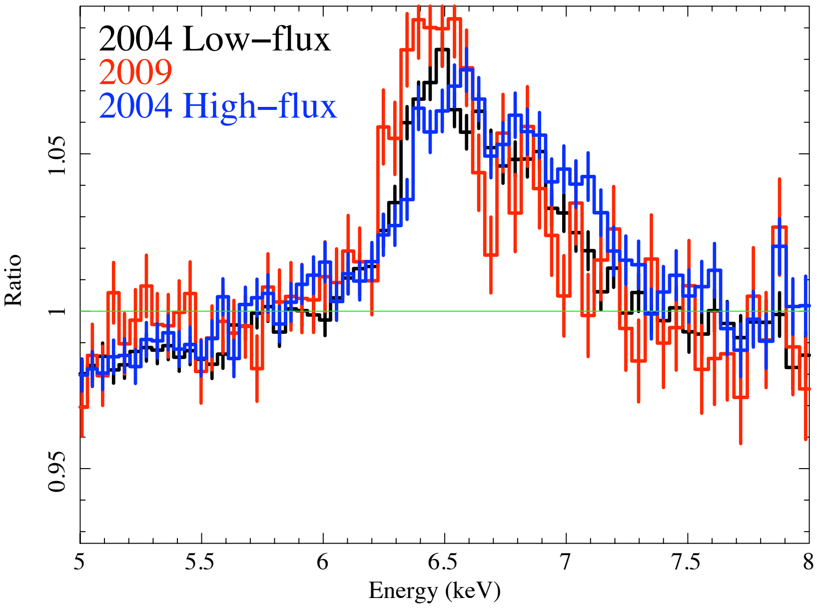

Figure 3.2: Data to model ratio plot using the thermal Comptonisation model NTHCOMP.

3.4.1 Choice of spectral model

To explore the hypothesis that the low frequency Lorentzian feature is a signature of the inner disc radius, the 2004 low-flux, 2004 high-flux and 2009 spectra were fitted simultaneously in XSPEC. Previous spectral fitting to hard-state observations of GX 339-4 has demonstrated evidence for both a soft excess and reflection features, consistent with reprocessing of the continuum emission from an optically thick accretion disc.

Self consistent reflection models such as REFLIONX (Ross & Fabian, 2005) consider reflection assuming conditions for supermassive black holes, where the accretion disk is at a much lower temperature. The assumption that the reflection spectrum of a BHXRB is simply that of a cool disc with a blackbody spectrum added is not valid. Both the line-shape and the surrounding continuum have been shown to be quite different (Ross & Fabian, 2007). When performing fits with the REFLIONX model, there is enhanced reflection and line emission from ionised material in the 0.1-1 keV bandpass which gives a soft X-ray excess (C. Done, private communication). In BHXRB spectra the source has a thermally reprocessed component at these energies, which the REFLIONX model mistakes for (and fits as) reflection. This can tend to drive the spectral fits due to the better statistics at these energies. This motivated us to perform our spectral fits using a simple phenomenological model TBNEW×(DISKBB+NTHCOMP+KYRLINE) consisting of a disc blackbody, a thermal Comptonised continuum and a relativistically smeared iron line. TBNEW[2] is a model which takes account of X-ray absorption by the interstellar medium (Wilms, Juett, Schulz & Nowak, 2009). DISKBB is a multi-colour disc blackbody model which is parameterised by the temperature at the inner disc radius and the normalisation which is defined as $(\mathrm{R_{in}}/\mathrm{D}^2)\cos i$ where R is the inner radius in km, i is the inclination angle and D is the distance to the source in units of 10 kpc. NTHCOMP (Zdziarski, Johnson, & Magdziarz, 1996; Życki, Done, & Smith, 1999) is a thermal Comptonisation model with a high-energy cut-off parameterised by the electron temperature (frozen at 75 keV in our fits), and, importantly, also includes a low-energy cut-off to account for the fact that at energies below the seed photon energies there are few photons in the scattered spectrum. NTHCOMP is parameterised by the power-law photon index, the electron temperature, the seed photon temperature and the normalisation, defined as the photon flux at 1keV in units of photons $\mathrm{cm^{-2}s^{-1}keV^{-1}}$. KYRLINE (Dovčiak, Karas, & Yaqoob, 2004) models the line emission from an accretion disc around a black hole taking general relativistic effects into account. It is parameterised by the black hole angular momentum (frozen at 0.9 in our fits consistent with the upper limit of Kolehmainen & Done (2010), though fits are insensitive to this parameter at large truncation radii), the inclination, the inner radius, the outer radius (frozen at 400 GM/c^2 in the model, though extending to larger outer radii had no effect on the fits), the rest energy of the line, the emissivity power-law index (initially frozen at -3 in our fits consistent with a simple accretion-disc-like emissivity profile) and the normalisation ($\mathrm{photons/cm^2/s}$ in the line).

The DISKBB normalisation is not a strictly accurate estimator of disc inner radius as it fits a disc blackbody spectrum to an X-ray illuminated disc. Some of the power-law flux incident on the disc is reprocessed and adds to the intrinsic disc flux, changing the disc emissivity profile. When a simple multi-colour disc blackbody is fitted, the disc temperature is overestimated and the disc radius underestimated (Gierliński et al., 2008). It would therefore be incorrect to infer anything about the disc inner radius from the blackbody normalisation of the model component DISKBB. When combined with the fact that the simple DISKBB model does not

---

[2] http://pulsar.sternwarte.uni-erlangen.de/wilms/research/tbabs/

take into account colour-temperature correction (Comptonisation leads to a higher observed colour temperature than the effective blackbody temperature by a factor of $\sim$1.7), I considered it as reliable to trust the estimate of inner radius provided by the KYRLINE model at the expense of “self-consistency” in our model. It should be noted however, that the interpretation of inner radius obtained from iron-line fitting is also hampered by factors such as unmodelled iron K-edges, the unknown ionisation and emissivity profile of the reflector and the reflection continuum.

The absorption and inclination were constrained to find the same best-fitting values across all three data sets and the disk blackbody seed photon temperature for the NTHCOMP model was assumed to be equal to the temperature at the inner disc radius obtained from DISKBB. Adding a reflection continuum component (PEXRIV) over the energy range 0.7-10.0 keV only marginally improved the fit. Given that the reflection fraction (and normalisation) of this component was small, I decided not to include a reflection continuum component in the model fits.

3.5 Evidence for a flux dependence of disc inner radius estimates

3.5.1 Fits with one KYRLINE component

An initial simultaneous fit to the 2004 low-flux, 2004 high-flux and 2009 data was performed over the energy range 0.7-10.0 keV using the model described above. In accordance with Done & Diaz Trigo (2009) a 1.0% systematic error is applied to this fit to allow for CTI features present in the data and for uncertainties in the response. The energy ranges 0.9-1.1 keV and 2.05-2.35 keV were ignored when fitting due to large CTI residuals in these regions (especially in the 2004 data). The DISKBB temperature, DISKBB normalisation, NTHCOMP normalisation, KYRLINE inner radius, KYRLINE rest energy and KYRLINE normalisation were all free to vary independently in each data set. This fit resulted in a χ^2/dof of 851/607 and the ratio plot shown in figure 3.3 demonstrates residual narrow-line emission and a possible absorption feature at around 7 keV.

A narrow Gaussian component ($\sigma = 0.01$ keV) was then also added to the model to account for residual narrow line emission which was not fitted by the KYRLINE model. Such a line may result from reflection at large radii. Evidence for such X-ray-optical correlations consistent with thermal reprocessing of X-rays into optical emission by the outer disc have been seen in SWIFT J1753.5-0127 and GX 339-

4 (Hynes et al., 2009; Gandhi et al., 2010). It has been suggested previously that reprocessing of X-rays from an optically thick accretion disc may be the cause of optical variations in both BHXRB and AGN (Russell et al., 2006; Breedt et al., 2009). Further discussion on this issue can be found in section 3.7.

The energy of the narrow-line Gaussian component was initially fixed at 6.4 keV, improving the χ^2/dof to 779/606. The individual narrow-line component energies of the three data sets were allowed to vary between 6.4 and 6.6 keV, which further improved the χ^2/dof to 732/603, with the Gaussian line energy increasing slightly with increasing flux. Finally, allowing the normalisations of the narrow line components to vary produced a final χ^2/dof of 724/601, which is a marginally significant improvement in chi-squared (F-test probability of 0.038). The equivalent width (EW) of the narrow gaussian component was 11 eV in the 2004 high and low-flux data, and 17 eV in the 2009 data. These fits suggest that a separate narrow Gaussian component is present, and furthermore that the normalisation and energy of the narrow-line needs to be free. This suggests that the outer-disc may be slightly ionised, which would favour a lower density (possibly flared) outer-disc. Referring back to figure 3.2, the blue wing of the line shifts with increasing flux to higher energies indicating that the inner disc is also becoming more ionised.

The full details of this fit are shown in table 3.1. A data-to-model ratio plot of this final fit is shown in figure 3.4 for comparison with figure 3.3. Given that the surrounding residuals in figure 3.4 are of similar order to the absorption-like feature at $\sim$7 keV, I decided not to fit this feature of the data.

The most surprising aspect of the fit is that the best-fitting inner radius in 2009 is not significantly different from the low-flux 2004 data. Figure 3.5 shows a contour plot from this fit, demonstrating that, under the assumptions made, there is a 1% chance that the confidence region does not cover the correct 2009 R_{in} / 2004 R_{in} ratio. However, figure 3.6 for the higher flux 2004 data, is clearly more consistent with a factor of 3 change in truncation radius if the 2004 radius lies between $\sim$20 and $\sim$35 Rg. The 2004 high-flux estimate of the inner radius is different to the 2004 low-flux estimate by more than a factor of two, and a contour plot comparing the allowed values of inner radius at these different fluxes is shown in figure 3.7. This plot shows that the amount of parameter space consistent with a fixed, flux-independent value of inner radius is very small.

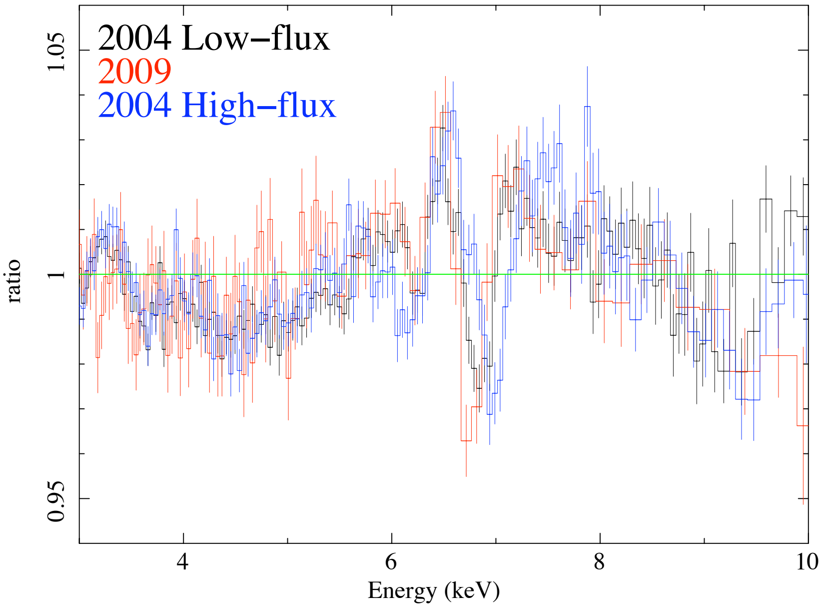

Figure 3.3: Data to best-fitting-model ratio using a model without a narrow Gaussian component. The KYRLINE model is clearly not fitting this residual narrower component of the line. Only the energy range 3.0-10.0 keV is shown, since there are large residuals due to CTI features and the energy bands 0.9-1.1 keV and 2.05-2.35 keV were ignored in the fits.

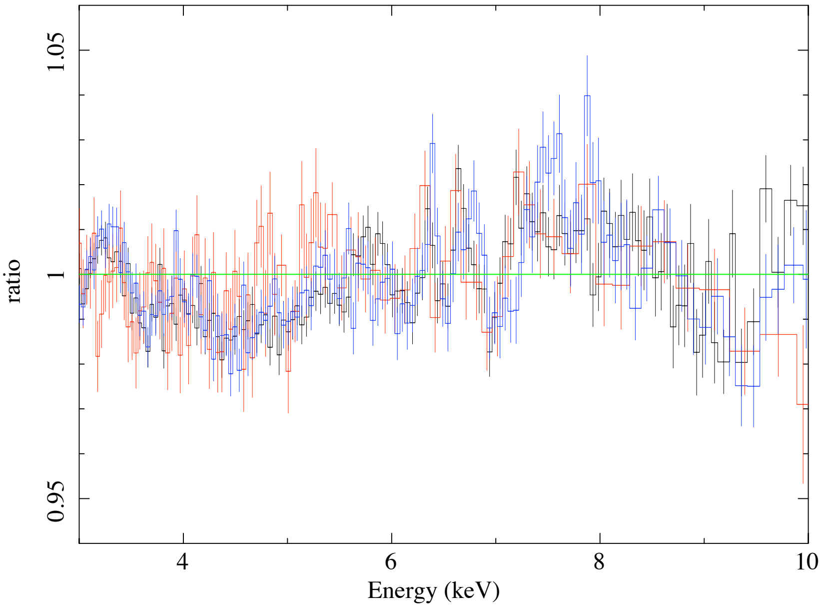

Figure 3.4: Data to best-fitting-model ratio which includes a narrow Gaussian component free to vary between observations in normalisation and energy between 6.4 and 6.6 keV.

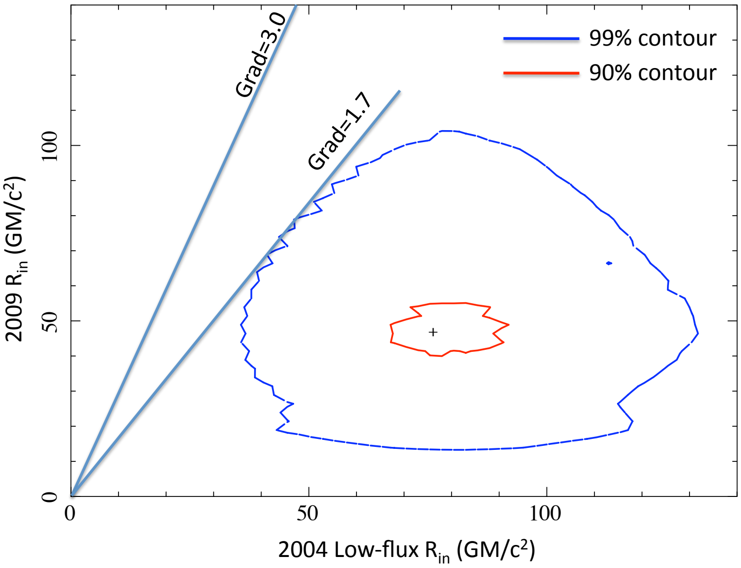

Figure 3.5: Confidence contour plot demonstrating the allowed variations in the 2004 Low-flux R_{in} and 2009 R_{in} for the fit shown in table 3.1. From the centre outwards, plotted are the 90% and 99% contours. The line drawn with a gradient of 1.7 just touches the 99% confidence contour, and therefore defines an upper limit to the ratio of the 2009 to 2004 low-flux radius estimates. For reference, a line with a gradient of 3 is also plotted.

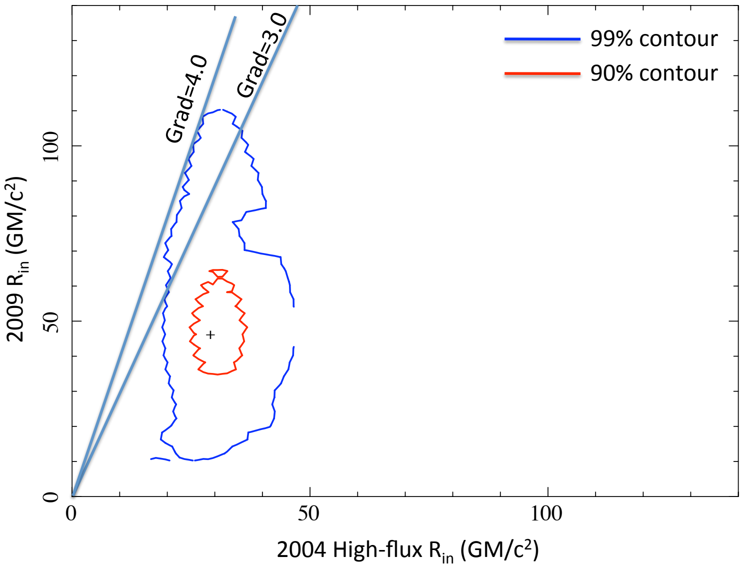

Figure 3.6: Confidence contour plot demonstrating the allowed variations in the 2004 high-flux R_{in} and 2009 R_{in} for the fit shown in table 3.1. The scales are identical to aid comparison with figure 3.5, showing that the high-flux estimate of R_{in} (horizontal axis) is much more constrained than the low-flux estimate.

Table 3.1: Best fitting parameters for the model TBNEW*(DISKBB + NTHCOMP + GAUSSIAN + KYRLINE). Features at 0.9-1.1 keV and 2.05-2.35 keV were ignored in this fit due to uncertainties in the response.

Parameter	2004 Low-flux	2004 High-flux	2009
$N_H(\times10^{22})$ tied	$0.52^{+0.01}_{-0.01}$	$0.52^{+0.01}_{-0.01}$	$0.52^{+0.01}_{-0.01}$
kT_{BB}(keV)	$0.30^{+0.01}_{-0.01}$	$0.34^{+0.01}_{-0.01}$	$0.30^{+0.01}_{-0.01}$
A_{BB}	1137^{+446}_{-101}	1300^{+288}_{-72}	360^{+107}_{-53}
R_{in} (GM/c^2)	76^{+31}_{-20}	30^{+8}_{-7}	46^{+27}_{-29}
E_{Kyr} (keV)	$6.61^{+0.04}_{-0.07}$	$6.61^{+0.05}_{-0.04}$	$6.54^{+0.06}_{-0.07}$
$A_{Kyr}(\times10^{-4})$	$4.6^{+0.6}_{-0.5}$	$12.0^{+1.3}_{-1.2}$	$3.5^{+0.6}_{-0.6}$
EQW_{Kyr}(eV)	51	77	57
Γ	$1.52^{+0.01}_{-0.01}$	$1.55^{+0.01}_{-0.01}$	$1.51^{+0.01}_{-0.01}$
Inc(°) tied	$47.4^{+1.9}_{-4.4}$	$47.4^{+1.9}_{-4.4}$	$47.4^{+1.9}_{-4.4}$
kTe (keV)	75.00(F)	75.00(F)	75.00(F)
$A_{nthcomp}$	$0.151^{+0.002}_{-0.001}$	$0.275^{+0.003}_{-0.002}$	$0.099^{+0.001}_{-0.001}$
E_{Gauss}(keV)	$6.48^{+0.03}_{-0.03}$	$6.54^{+0.03}_{-0.03}$	$6.45^{+0.03}_{-0.03}$
$A_{Gauss}(\times10^{-4})$	$1.1^{+0.3}_{-0.3}$	$2.0^{+0.5}_{-0.4}$	$1.2^{+0.2}_{-0.2}$
EQW_{Gauss}(eV)	11	11	17
χ^2 / d.o.f : 723.94 / 601			

From the top to bottom, parameters are hydrogen column density, blackbody temperature, blackbody normalisation, disc inner-radius relative to the horizon, Kyrline rest energy, Kyrline normalisation, Kyrline equivalent width, photon index, inclination, electron temperature of the Comptonising region, normalisation of the thermal Comptonisation continuum, narrow Gaussian line energy, Gaussian normalisation and finally its equivalent width. The emissivity was fixed at -3.0 and R_{out} was fixed at 400 R_G. The narrow Gaussian line width was frozen at 0.01. Tied indicates that these parameters were free to vary, but constrained to be the same for all three data-sets. Frozen (F) indicates that parameters were fixed at this value during the fitting procedure. Quoted errors are at the 90% confidence level.

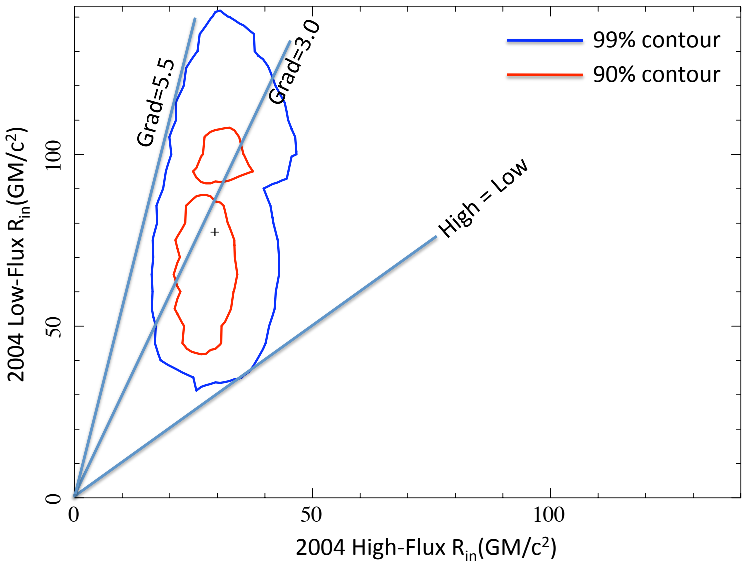

Figure 3.7: Confidence contour plot demonstrating the allowed variations in the 2004 high-flux $R_{\rm in}$ and 2004 low-flux $R_{\rm in}$ for the fit shown in table 3.1. The amount of parameter space consistent with a flux-independent value of inner radius is very small and is situated towards the bottom right of the contours.

3.5.2 Fits with two KYRLINE components

The model described previously, and shown in Table 3.1, includes one KYRLINE component, and therefore ascribes a single rest-frame energy to the fluorescent Kα line emission. To allow for the possibility that multiple ionisation states of iron could co-exist at similar radii, broadening the overall line width, a second fit was performed with two KYRLINE components whose energies were constrained to lie between 6.4 (Fe XVII and lower ionisation states) and 6.97 keV (hydrogen-like Fe XXVI). This best fitting parameters of this fit are shown in Table 3.2. The inner radii of these two KYRLINE components were tied to be the same value and the emissivity indices were fixed at -3.0. The chi-squared of this fit was significantly better than the fit of Table 3.1 with a χ^2/dof of 661/595. The inner radii from this fit are very similar to those in Table 3.1 with the high-flux inner radius still significantly lower than the low-flux estimate. The data-to-model ratio plot in figure 3.8 shows that the residuals around the iron-line region are reduced further, and also that the absorption-like feature present in figures 3.3 and 3.4 has been largely subsumed in to the lines. It should be noted that the narrow Gaussian component was still required in these fits with EQWs comparable to those in table 3.1.

Allowing the ionisation state of iron in the disc to vary in this way (by including two KYRLINE model components) permits a slightly larger truncation of a factor 2.5 in the 2009 data, as demonstrated in figure 3.9. The confidence contours of Figure

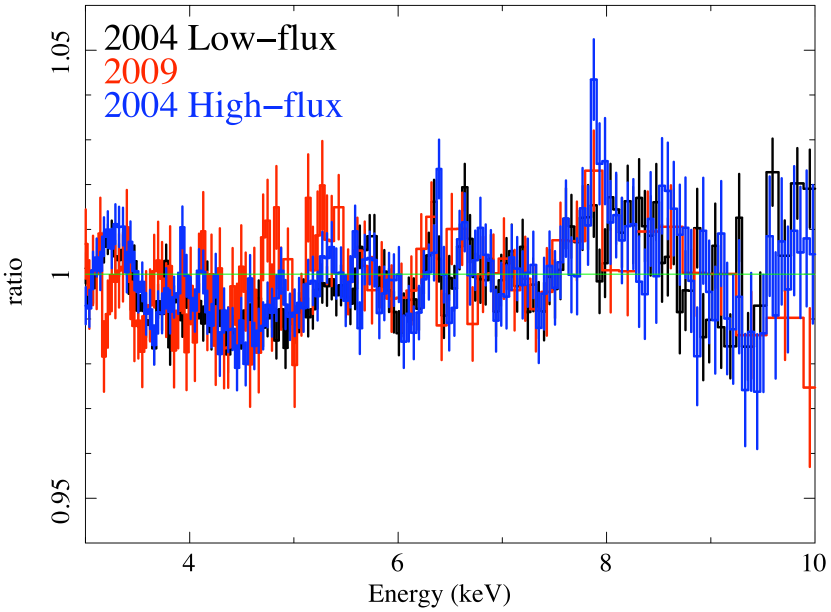

Figure 3.8: Data to best-fitting-model ratio which includes two KYRLINE components free to vary between 6.4 and 6.97 keV and a narrow Gaussian component free to vary between observations in normalisation and energy between 6.4 and 6.6 keV

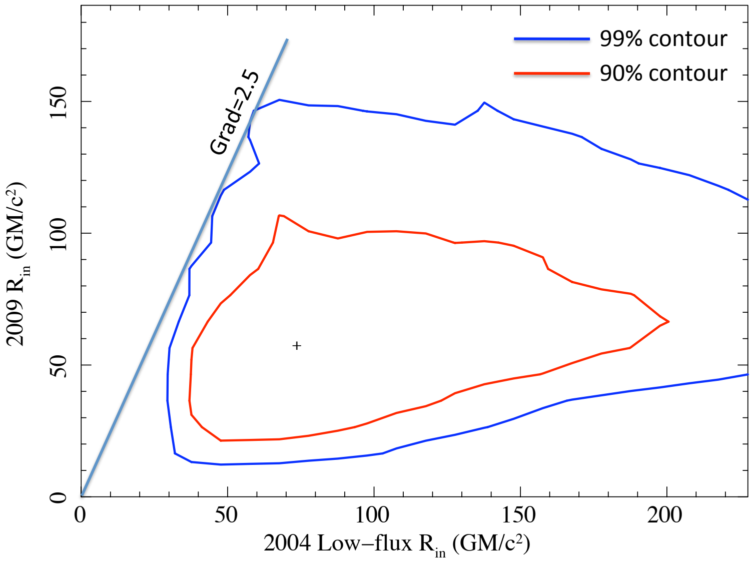

Figure 3.9: Contour plot showing that, for the fit with two kyrline components, the 2004 low-flux inner radius is allowed to truncate by a factor of 2.5 at the 99% level.

Table 3.2: Best fitting parameters for the model TBNEW*(DISKBB + NTHCOMP + GAUSSIAN + KYRLINE + KYRLINE). As in table 4.1, features at 0.9-1.1 keV and 2.05-2.35 keV were ignored in this fit due to uncertainties in the response.

Parameter	2004 Low-flux	2004 High-flux	2009
nH($\times10^{22}$) tied	$0.52^{+0.01}_{-0.01}$	$0.52^{+0.01}_{-0.01}$	$0.52^{+0.01}_{-0.01}$
kT_{BB}(keV)	$0.29^{+0.01}_{-0.01}$	$0.34^{+0.01}_{-0.01}$	$0.29^{+0.01}_{-0.01}$
A_{BB}	1211^{+430}_{-71}	1349^{+174}_{-47}	385^{+23}_{-37}
R_{in} (GM/c^2)	74^{+40}_{-30}	32^{+9}_{-9}	58^{+17}_{-17}
E_{Kyr1}(keV)	$6.53^{+0.05}_{-0.05}$	$6.47^{+0.06}_{-**}$	$6.41^{+0.09}_{-**}$
E_{Kyr2}(keV)	$6.95^{+**}_{-0.19}$	$6.97^{+**}_{-0.04}$	$6.86^{+**}_{-0.13}$
A_{Kyr1}($\times10^{-4}$)	$3.9^{+0.7}_{-0.5}$	$9.5^{+1.9}_{-0.8}$	$2.7^{+0.7}_{-0.4}$
A_{Kyr2}($\times10^{-4}$)	$1.74^{+0.47}_{-0.54}$	$5.76^{+1.65}_{-1.21}$	$1.65^{+0.66}_{-0.57}$
EQW_{Kyr1}(eV)	42	60	41
EQW_{Kyr2}(eV)	20	40	28
Γ	$1.52^{+0.01}_{-0.01}$	$1.56^{+0.01}_{-0.01}$	$1.51^{+0.01}_{-0.01}$
Inc(°) tied	$52.5^{+2.5}_{-4.0}$	$52.5^{+2.5}_{-4.0}$	$52.5^{+2.5}_{-4.0}$
kTe (keV)	75.00(F)	75.00(F)	75.00(F)
$A_{nthcomp}$	$0.152^{+0.002}_{-0.001}$	$0.277^{+0.001}_{-0.001}$	$0.099^{+0.001}_{-0.001}$
E_{Gauss}(keV)	$6.46^{+0.02}_{-0.04}$	$6.52^{+0.04}_{-0.04}$	$6.43^{+0.03}_{-0.03}$
A_{Gauss}($\times10^{-4}$)	$1.1^{+0.3}_{-0.3}$	$1.6^{+0.5}_{-0.3}$	$1.0^{+0.3}_{-0.2}$
EQW_{Gauss}(eV)	11	9	15
χ^2 / d.o.f : 661.46 / 595			

Kyrline rest energies were free to vary between 6.4 and 6.97 keV and inner radii were tied together. The emissivity was fixed at -3.0 and R_{out} was fixed at 400 R_G. The narrow Gaussian line width was frozen at 0.01. Tied indicates that these parameters were free to vary, but constrained to be the same for all three data-sets. Frozen (F) indicates that parameters were fixed at this value during the fitting procedure. Values of inner radius are relative to the horizon. Quoted errors are at the 90% confidence level. ** indicates that the fit parameters pegged at the upper or lower limit during the error calculations.

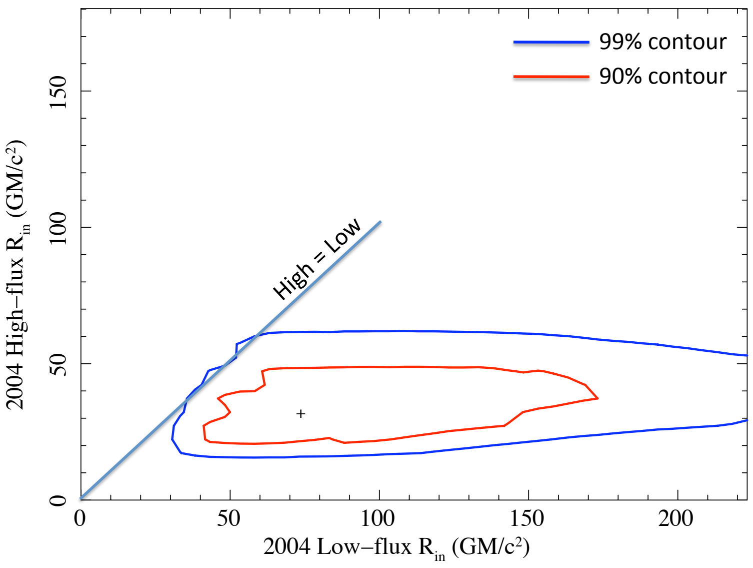

Figure 3.10: With two kyrline components the confidence contours show that identical radius estimates are excluded at more than the 90% confidence level.

3.10 show that identical radius estimates for the 2004 low and high-flux data are excluded at more than 90% confidence, similar to figure 3.7.

To summarise this section, both fits assuming a single Kα line energy and fits allowing for multiple ionisation states of iron show no evidence for a factor of 3 truncation in the 2009 inner radius relative to the 2004 value *derived from the low-flux data*. However, the high-flux data is more consistent with a factor of three truncation in inner radius. Furthermore, contour plots of the 2004 high-flux derived inner radius against the 2004 low-flux derived value indicate that only a very small amount of parameter space is consistent with no change in radius estimates. This clearly points to a flux dependent change in the inner radius measurement. I now go on to consider arguments that suggest this flux dependence is not a real effect.

3.6 Evidence against a flux dependence of disc inner radius estimates

If the lower estimates of inner radius derived from the high-flux data are genuine, then there should be a flux-dependence of the lag between the direct power-law emission and the reflected emission. The shape of the lag vs energy spectrum is thought to arise as a result of two distinct processes that are dependent on frequency. At high frequencies (2-8 Hz) the soft photons *lag* the hard photons where as at lower frequencies (0.01-1 Hz) the soft photons *lead* the hard photons. At low frequencies (figure 2.9), the hard lag (hard photons lagging soft) is most likely due to the production and propagation of mass accretion rate fluctuations through the disc prior to reaching the power-law region (Arévalo & Uttley, 2006; Uttley et al., 2011). At high frequencies, however, X-ray heating by the illuminating power-law is thought to dominate the disc variability and a characteristic upturn is seen at low energies in the lag vs energy spectrum due to thermal reprocessing. The magnitude of the soft-lag seen at high frequencies is therefore associated with the light travel time from the power-law emitting region to the disc. If the disc were truncated further from the power-law, then the reflected emission would have travelled a larger path length producing a larger lag. Figure 3.11 shows a short-timescale (2-8 Hz) lag spectrum, demonstrating that, to within the errors, the upturn in the lags at soft energies is independent of flux. This suggests that the flux dependence of the inner radius may not be a real phenomenon, but simply a manifestation of the degeneracies inherent in the fitting of iron-line components at large inner radii.

The location of the inner radius of the disc governs the soft-photon flux incident on the hot-flow. If the disc moves inwards, closer to the hot-flow, the subsequent Compton-cooling would be expected to soften the slope of the power-law. In this way, a flux-flux plot in distinct non-overlapping energy bands covering soft and hard photons, can be used to identify changes in truncation radius. Using the slope of a flux-flux plot from 2004 as reference, one can determine whether or not the ratio of hard to soft emission has changed significantly in 2009 as would be expected if the disc truncation radius has changed appreciably. If the 2004 and 2009 flux-flux plots show a linear trend of similar slope, then this would be a strong model-independent indicator that the disc truncation radius is similar. Light curves with 4 second binning were created of the 2004 and 2009 outbursts, and binned flux-flux plots were created in several energy bands as displayed in figure 3.12. In the upper two panels of figure 3.12 the intercept on the y-axis of a straight line fit through the 2004 flux points is non-zero. This indicates that there is an extra, stable component contributing at soft energies (if the correlation is extrapolated down to zero hard flux there is still a soft component). It has been established previously in this source (chapter 2 and Wilkinson & Uttley (2009)) that there is extra power present on longer timescales (tens of seconds) at softer energies, corresponding to the low frequency Lorentzian feature in the PSD. This has been explained in terms of variations intrinsic to the disc giving rise to extra variability on these timescales. The extra stable component in the 2004 observation implies that this disc variability is less pronounced, agreeing with the power-spectra of figure 3.1, which clearly shows a lower amplitude of variability in 2004 than in 2009. It is clear that the

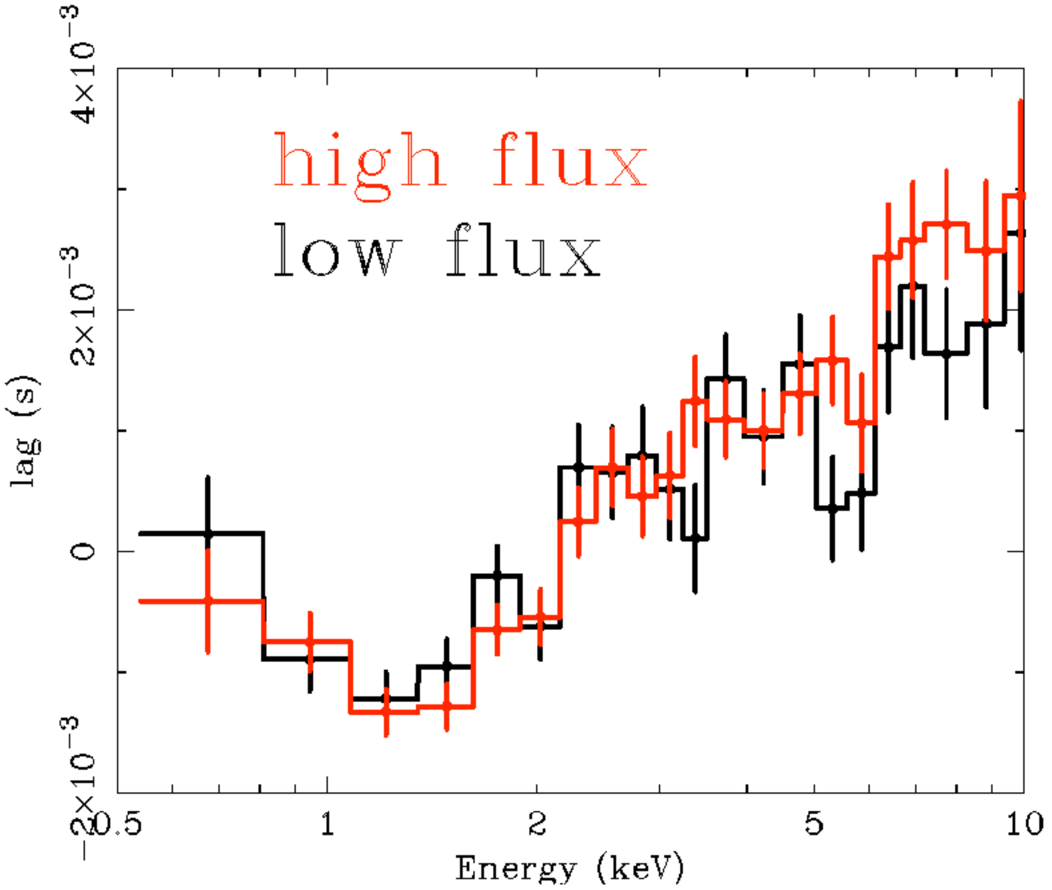

Figure 3.11: Short timescale (2-8 Hz) lag spectrum using a 0.5-10 keV reference band demonstrating the upturn at soft energies thought to be caused by disc illumination by the X-ray power-law. The magnitude of the soft-lag is associated with the light travel time from the power-law emitting region to the disc. The lag between the direct power-law emission and the reflected emission is independent of flux in this figure, supporting the idea that the geometry is similar and the inner radius of the disc is not a function of flux (Phil Uttley, private communication).

2004 observation has more soft emission than the 2009 observation, a fact also corroborated by the black body normalisations in tables 4.1 and 4.2 and in the ratio plot of figure 3.14. Given the similarity of the hard components in the lower panel of figure 3.12, it is unlikely that the properties of the disc are changing considerably at its inner radius. The continuum slopes in tables 4.1 and 4.2 are very similar between 2004 and 2009, also suggesting that there is not a significant hardening of the spectrum or a large change in geometry. The similarity of the power-law slopes and the fluxes in the lower plot of figure 3.12, may indicate that the relative change in soft-photon flux between the 2004 and 2009 observations is not seen by the power-law. With the caveat that there needs to be enough seed photons to produce the observed hard x-rays (since Comptonisation conserves photon number),

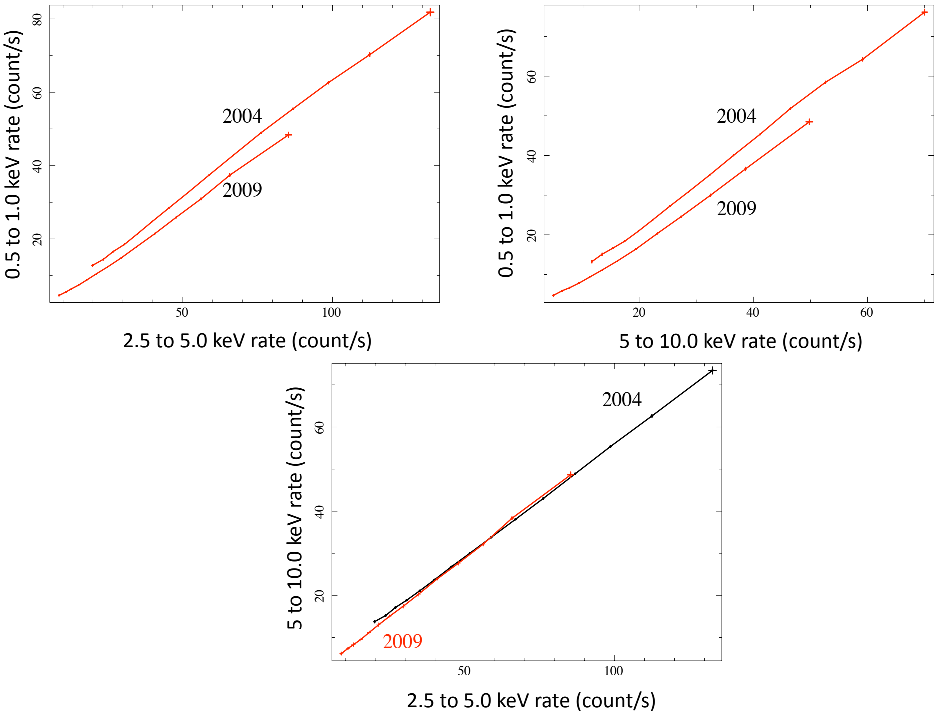

Figure 3.12: Flux-flux plots for the 2004 and 2009 data showing the stability of the hard component (lower panel) and the presence of an extra stable soft component in the 2004 observation (top panels).

this could be consistent with a larger radius of truncation, where the solid angle subtended by the hot-flow is small. Another possibility, which does not preclude changes of inner radius, is that a Compton ‘thermostat’ (Haardt & Maraschi, 1991) could be operating that maintains the same photon index at different fluxes.

3.6.1 Variable Emissivity

So far, in the spectral fits performed on the 2004 and 2009 data, I have allowed the ionisation state of iron to vary within the disc by including two KYRLINE models, but the constant emissivity profile means that the line ratios are constant across the disc. In other words, the ratio of the flux of different ionisation states at any given radius is always the same. By allowing the emissivity profile of the reflected emission to be different for each line, this constraint is removed, and the ratio of iron line fluxes is allowed to change with radius. The inner radius and the emissivity are highly degenerate parameters in the KYRLINE model (both have a profound effect on the line-shape), so freeing the emissivity index allows the inner radius to move closer to the innermost stable circular orbit (ISCO). I fitted the total 2004 and 2009 data using the two KYRLINE model described in section 3.5.2, but with

Table 3.3: Best fitting iron line parameters from the fit to the model TBNEW*(DISKBB + NTHCOMP + GAUSSIAN + KYRLINE + KYRLINE) with the emissivity and line energy of each KYRLINE component free to vary.

Parameter	2004 Total	2009
$R_{\rm in}$ (GM/c^2)	$0.3^{+13.2}_{-**}$	$0.6^{+21.6}_{-**}$
$E_{\rm kyr1}$ (keV)	$6.58^{+0.04}_{-0.04}$	$6.52^{+0.05}_{-0.07}$
$\alpha_{\rm kyr1}$	$1.23^{+0.26}_{-0.66}$	$1.51^{+0.24}_{-1.04}$
$E_{\rm kyr2}$ (keV)	$6.97^{+**}_{-0.15}$	6.97^{+**}_{-**}
$\alpha_{\rm kyr2}$	$2.43^{+0.73}_{-0.51}$	$3.16^{+**}_{-1.22}$
$A_{\rm kyr1}(\times 10^{-4})$	$6.9^{+1.4}_{-2.2}$	$4.7^{+0.9}_{-2.1}$
$A_{\rm kyr2}(\times 10^{-4})$	$3.6^{+2.0}_{-1.4}$	$1.4^{+2.5}_{-1.0}$
Γ	$1.54^{+0.01}_{-0.01}$	$1.51^{+0.01}_{-0.01}$
Inc($^\circ$) tied	$59.8^{+**}_{-7.0}$	$59.8^{+**}_{-7.0}$
$E_{\rm Gauss}$(keV)	$6.51^{+0.03}_{-0.05}$	$6.45^{+0.03}_{-0.03}$
$A_{\rm Gauss}(\times 10^{-4})$	$1.1^{+0.3}_{-0.3}$	$1.1^{+0.2}_{-0.2}$
χ^2 / d.o.f : 346.44 / 391		

KYRLINE rest energies were free to vary between 6.4 and 6.97 keV, inner radii were tied together, the emissivity was free to vary and R_{out} was fixed at 400 R_G. The narrow Gaussian line width was frozen at 0.01. Tied indicates that these parameters were free to vary, but constrained to be the same for both data-sets. Values of inner radius are relative to the horizon, which is why quoted values are so small. Quoted errors are at the 90% confidence level. ** indicates that the fit parameters pegged at the upper or lower limit during the error calculations. Parameters not quoted are very similar to those in table 3.2.

the emissivity as well as the energy of both KYRLINE components free to vary (the latter between 6.4 and 6.97 keV). This produced a best fit of 346.44/391 and the fit parameters are shown in table 3.3. The large amount of degeneracy in this fit meant that there was a high degree of uncertainty in many of the parameters, with several of them hitting their upper/lower limits during the error calculations. The main purpose of this fit is simply to illustrate that, with the appropriate choice of emissivity index, a model can be fitted to the data which is consistent with the disc being truncated at or very close to the ISCO.

Figure 3.13 shows a contour plot of the 2004 vs 2009 inner radius, for comparison with figure 3.9. When the index of emissivity is a free parameter, the inner radius is more constrained but could lie anywhere between the ISCO and ~40Rg.

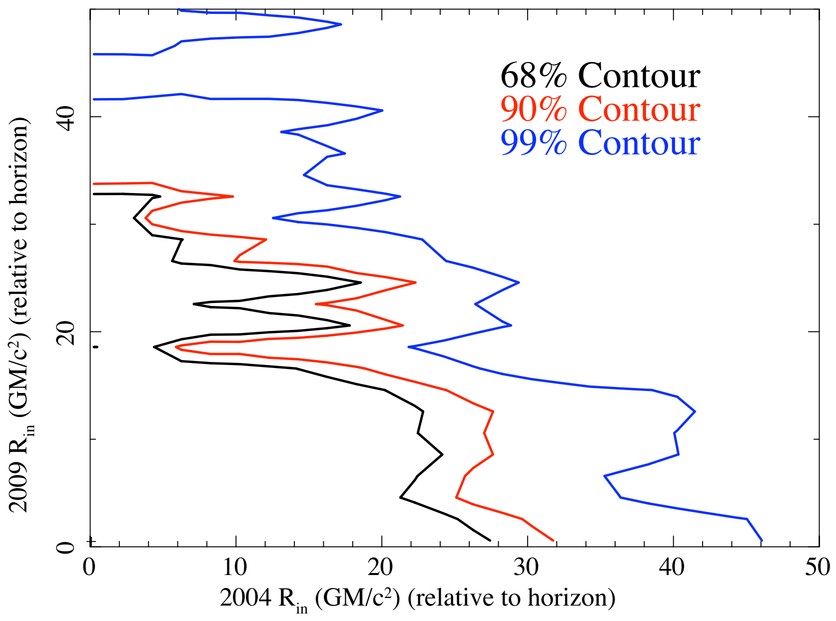

Figure 3.13: Contour plot showing the allowed range of 2004 and 2009 inner radii for the fit in table 3.3. The best fitting values of inner radii are at the lower left hand corner of the plot. $R_{in} = 0$ corresponds to the event horizon, which is always greater than GM/c^2.

This plot illustrates that current models are too degenerate to draw any firm conclusions regarding the location of the inner radius of the accretion disc from spectral fitting alone.

3.7 Discussion

Figure 3.14 shows a ratio of the higher flux 2004 data to the 2009 data, demonstrating that the narrow iron-line emission relative to the continuum is stronger in the 2009 data than it is in 2004. The fact that this difference is confined mostly to the narrow core of the line, suggests that it is the reflection at larger radii that contributes most of the change in iron-line shape between these two observations. An obvious explanation for this might be that the solid angle for reflection at large radii is higher in 2009, possibly due to a more flared outer disc. Although not statistically significant, table 3.3 shows that the Gaussian line energy is lower in 2009 than in 2004, implying that the outer disc is less ionised. It should however be remembered

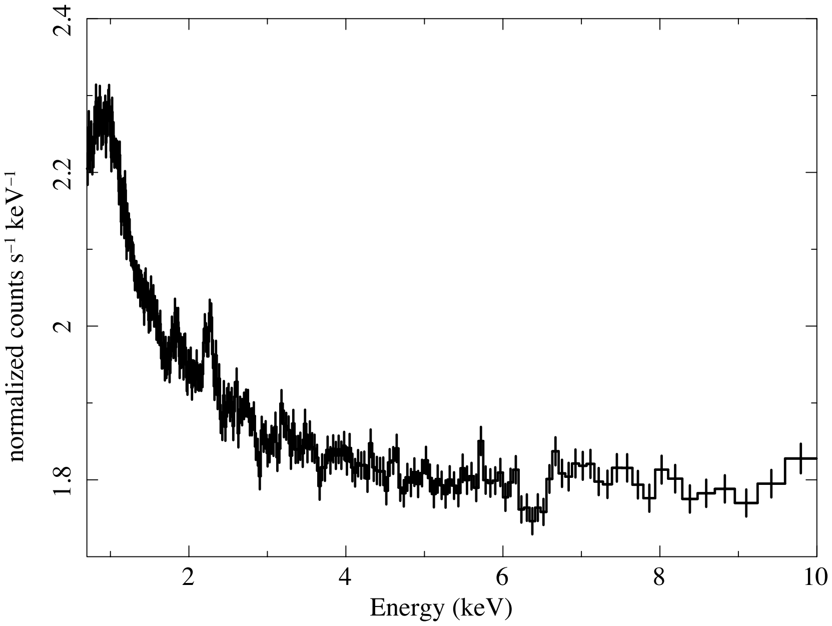

Figure 3.14: A ratio of the total 2004 data to the 2009 data, showing CTI features, extra blackbody emission in the 2004 data and a lower contribution from the core of the iron-line region.

that the flux is much lower in the 2009 observation, so this line energy may not be inconsistent with a more flared (less dense) disk.

It is apparent from spectral fitting that a residual "narrow" component remains at ∼6.4 keV when iron-line models are fitted. Reprocessing occurring at large radii could explain this feature, and a simple order of magnitude calculation can lend some weight to this argument. Referring to figure 5 of Coriat et al. (2009), it can be seen that just prior to the jet switching on in the hard-state of GX 339-4 the optical flux is approximately 10 mJy and the X-ray flux is approximately 2.5×10^{-9} ergs s^{-1} cm^{-2}. The model flux from the 2009 spectral fit (using the same 9-200 keV band as in Coriat et al. (2009)) is 3.8×10^{-9} ergs s^{-1} cm^{-2}. Therefore it is reasonable to assume that, to within an order of magnitude, the optical flux in the 2009 data should be around 15 mJy (1.5×10^{-25} ergs s^{-1} cm^{-2} Hz^{-1}). Assuming the width of the V-band is 1.7×10^{15} Hz and that the iron line flux is approximately 1% of the optical flux, one would expect the total number of photons/cm^2/s in the narrow iron line to be $\sim 2\times10^{-4}$. This lower limit (some of the optically reprocessed emission falls outside of the V-band) is within a factor of ∼2 of the observed GAUSSIAN normalisations measured in tables 3.1 and 3.2.

In sections 3.5.1 and 3.5.2, contour plots comparing estimates of inner radius derived from high and low-flux subsets of the 2004 data, revealed a possible flux dependence of the truncation radius. These rate-selected spectra were generated from 2-second binned light curves, but the viscous time-scale at a typical inner radius derived from the low-flux data of 70Rg for an optically thin flow is $>$100 s. Since the viscous timescale represents the time on which accreted material can drift inwards from the larger low-flux estimates of radius to the smaller high-flux estimates, it is therefore unlikely that the disc truncation radius could move on such short timescales. Further model independent analysis in the form of energy dependent lags and flux-flux plots provided strong evidence that this flux dependence was not real, but simply a result of the degeneracies in the spectral model.

With the exception of section 3.6.1, the power-law index of emissivity is frozen at -3 in the KYRLINE models in all of our spectral fits. As shown in section 3.6.1, it is possible to get much smaller inner radii ($< 2\mathrm{R_g}$) if the emissivity is low ($<$2.0). A low emissivity index implies that the reflected emission per unit area is not highly centrally concentrated, perhaps indicating a very ionised inner flow or a large scale-height corona which preferentially illuminates larger radii. However, it is the *relative* truncation of the inner-disc I wanted to explore in this analysis, so by fixing the emissivity at a sensible value in much of our analysis, I hope to have circumvented some of the controversies surrounding an objective measure of the disc truncation radius in the hard-state of BHXRBs.

It is important to explore the self consistent reflection model, despite the caveats mentioned in section 3.4.1, to see if the degeneracy between the emissivity index and inner radius was less problematical. Fits to the 2009 data using the self-consistent reflection model REFXION[3] indicate that the reflected fraction is less than 0.15, the disc is only moderately ionised ($\xi = 4\pi F/n \sim 650$) and the 2009 truncation radius is $\sim$ 11Rg with a best-fitting power-law emissivity index of -2.25. The confidence contour plot in figure 3.15 shows that the emissivity index and inner radius are still very degenerate in these spectral fits, and the data/model are not of sufficient quality to differentiate between the contribution from these two parameters. This justifies the decision to freeze the emissivity at -3 in our phenomenological models for both the 2004 and 2009 observations, enabling us to break the degeneracy and explore the relative changes in truncation radius. It should, of course, be noted that due to this degeneracy, any inferred radius changes could actually be changes in the emissivity profile of reflection coming from the disc, and the truncation radius could remain constant.

---

[3] REFXION is a convolution model based on the reflection model REFBAL described in (Done & Gierliński, 2006). Instead of using the reflected spectra of D. Ballantyne (Ballantyne, Iwasawa, & Fabian, 2001) this model uses the reflionx fits table of Ross & Fabian (2005) for any illuminating continuum.

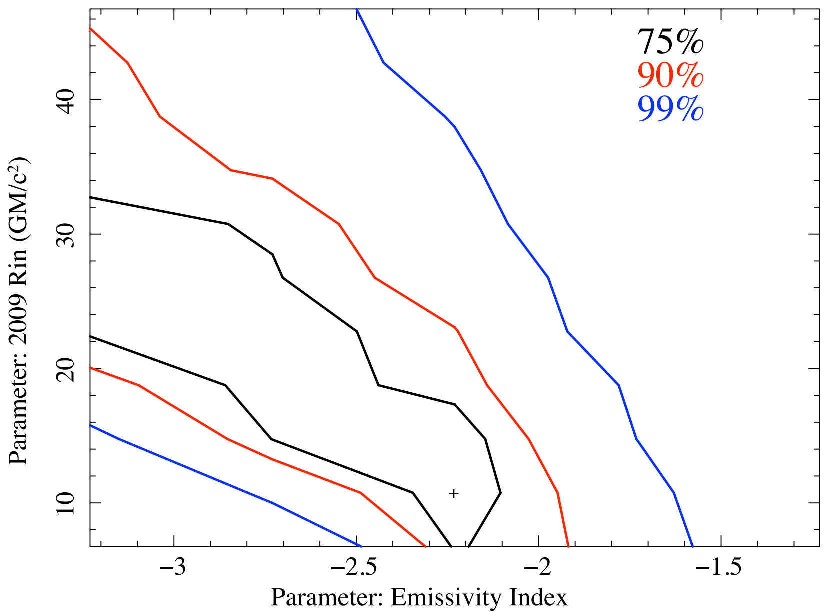

Figure 3.15: Confidence contour plot showing the degeneracy between the power-law index of emissivity and the inner radius for the 2009 observation using the spectral model TBNEW*(DISKBB + RDBLUR * (REFXION * NTHCOMP) + NTHCOMP + GAUSSIAN).

If the shift in frequency cannot be explained by changes in the disc truncation radius, then it is possible that this is a signature of some characteristic timescale of intrinsic disc variability (Wilkinson & Uttley, 2009). Alternatively, the broad low-frequency Lorentzian could be a quasi-periodic-oscillation (QPO) arising due to Lense-Thirring precession of the hot inner flow (Ingram, Done, & Fragile, 2009). The precession frequency is a function of the varying surface density, and when high-frequency accretion rate fluctuations can be propagated through the flow, the QPO could become markedly more incoherent. The results described in this paper show no strong evidence for a varying truncation radius, despite a large change in the characteristic low-frequency break. If this break can indeed be associated with a Lense-Thirring QPO, then it is possible that the properties of the flow itself could be changing, as well as its radial extent. If the flow was geometrically thick, hot and therefore of low density, it would be considerably more transparent to high-frequency fluctuations in mass-accretion rate than a thin Shakura-Sunyaev type disc. Broadened QPOs would be favoured by hot, large scale-height flows and current models indicate truncation radii of $> 50R_g$ for precession frequencies ∼0.01Hz, not inconsistent with our simple fits to the iron line with a standard accretion-disc-like emissivity profile.

In a source such as GX 339-4, where the inclination is not well constrained, one needs to be extremely careful when interpreting spectral fits to the iron-line. The inclination dramatically modifies the velocity component of material in the disc towards the observer which effects the blue-wing of the iron line, the location of the inner radius has a large effect on the red wing of the line and the line itself becomes much less centrally peaked when the emissivity profile is flat. In our spectral fits of section 3.6.1, the emissivity index is forced downwards to fit the narrow core of the line, possibly indicating that the reflected emission is coming from larger radii. When comparing the line shapes, as in figures 3.2 and 3.14, the red wing of the line is similar between 2004 and 2009 also indicating that there is no significant change in the truncation radius of the disc.

3.8 Conclusions

I have performed spectral fitting to *XMM-Newton* data from the 2004 and 2009 low/hard-state outbursts of GX 339-4 in an attempt to constrain the changes in truncation radius. Our analysis has shown that there is no strong evidence for large changes in the disc truncation radius between these observations despite a factor of 5 change in the low-frequency Lorentzian timing signature. The change in iron line shape is largely confined to the narrow core, and this could be explained by changes in the reflection occurring at large radii. The work discussed in this chapter therefore shows no strong evidence that the low-frequency Lorentzian feature in the hard-state power-spectra of GX339-4 can be associated with the viscous timescale at the inner edge of the accretion disc. A possible alternative explanation for this feature could be a broadened QPO arising from precession of the hot inner-flow, or some characteristic timescale of intrinsic disc variability. The apparent flux dependence of the fits in section 3.5 highlights the care that must be taken when interpreting complex, often degenerate, spectral fits. The use of methods to independently verify the results of spectral fitting should be undertaken whenever possible.

Science is a wonderful thing if one does not have to earn one's living at it.

ALBERT EINSTEIN (1879 - 1955)

4

Exploring the QPO variability spectrum in the 2010 outburst of GX 339-4: Evidence that the disc might drive the QPO

I examine the spectral and timing properties of the type-B quasi-periodic oscillation (QPO) observed in the 2010 outburst of GX 339-4 as measured by the Rossi X-ray Timing Explorer (RXTE). My analysis shows that the disc variability is markedly reduced over the QPO frequencies, with only the innermost parts of the disc contributing to the QPO variability spectra when the QPO is near its maximum fundamental frequency. This is consistent with the QPO being generated by a region of turbulence near the inner edge of the disc where intrinsic disc variations cannot modulate a significant fraction of the disc luminosity. Energy dependent lag spectra obtained over the QPO frequencies demonstrate that the disc blackbody variations lead the power-law variations, indicating that the disc could be driving the QPO. These results are consistent with the overall picture that the QPO frequency corresponds to a radius, R_{QPO}, where a region of turbulence occurs in the disc. If the

turbulent region moves on viscous timescales then $\nu_{\rm QPO} \propto {\rm R_{QPO}}^{-3/2}$. The QPO finally switches off when the turbulent region reaches the ISCO and the innermost disc becomes stable.

4.1 Introduction

It is well established that Black Hole X-ray Binaries (BHXRB) display many different source states as an outburst evolves. Originally, these states were simply distinguished in terms of the energy bands which dominated the observed emission. A wealth of subsequent observations of such systems, largely thanks to the Rossi X-ray Timing Explorer (RXTE), has led to more detailed and rich phenomenology. Now source states can be segregated according to their variability properties as well as their energy dependence and luminosity. The evolution of BHXRB behaviour with time is perhaps best illustrated by means of hardness-intensity diagrams (HID) and/or hardness-rms diagrams (HRD) (Muñoz-Darias, Motta, & Belloni, 2010). For a full overview of the current picture of states and transitions in BHXRB, the reader is referred to Belloni (2009).

It was shown in chapter 2 that in a previous 2004 hard-state observation of GX 339-4 the power-spectrum (PSD) of this source demonstrated larger low-frequency power in the soft band, and that this could be associated with intrinsic variability of the disc thermal emission on these timescales. The implication of this work was that the disc was responsible for the low-frequency Lorentzian feature in the power-spectrum of this hard-state observation. Subsequent Target Of Opportunity (TOO) *XMM-Newton* hard-state observations of GX 339-4 obtained in 2009 and 2010 have established beyond doubt that the disc dominates the variability over two decades in frequency up to ∼2 Hz. The strong evidence (figure 2.9) that intrinsic disc variability drives the power-law variability in the hard-state came recently from the discovery that disc blackbody variations on time-scales of seconds lead the variations in the power-law emission by ∼0.1s (Uttley et al., 2011).

Having established the role of the disc in the hard-state at low-frequencies, I wanted to extend this analysis to examine the importance of disc variability at higher frequencies and in other black hole states. It is currently entirely unclear at what stage of the outburst the intrinsically variable disc becomes stable. In the following sections I shall show evidence that disc signatures are present in the QPO variability and lag spectra, and at the QPO frequencies examined in this work it is most likely the variations occurring at the inner-edge of the disc that contribute to, and possibly

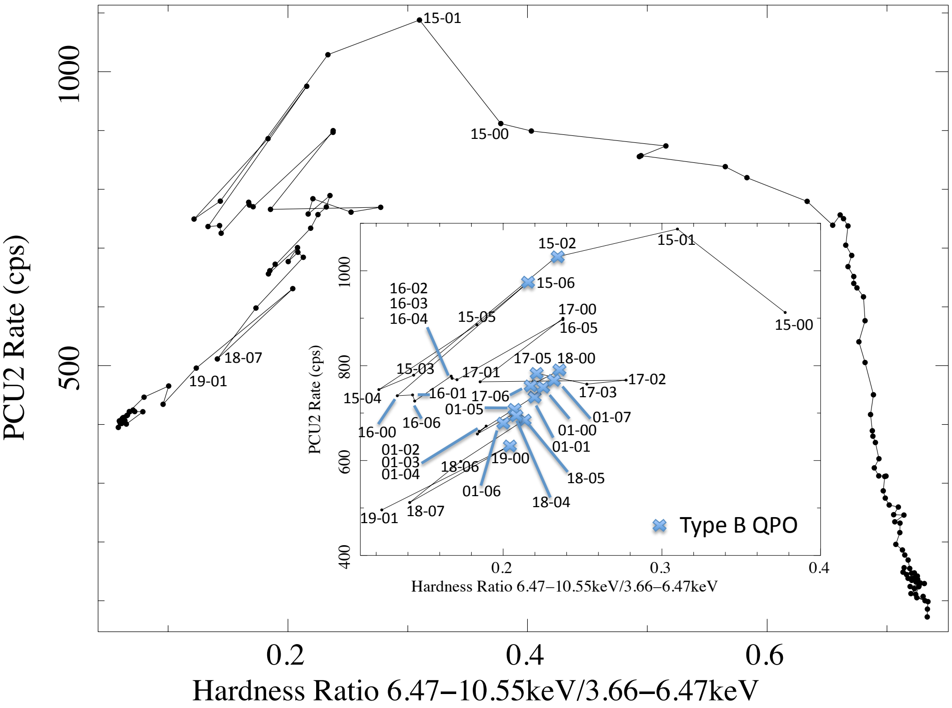

Figure 4.1: Hardness ratio plot showing the evolution of the 2010 outburst. Inset is close up of observations 95409-01-14-05 to 95409-01-18-07.

drive, the QPO.

4.2 Observations and Analysis

I extracted data from *RXTE* observations of GX 339-4 in its 2010 outburst. I used high time and energy resolution Proportional Counter Array (PCA) 125 μsec event mode data from observation IDs P95409 and P95335. Data extraction followed standard methods, creating Good Time Intervals (GTIs) using the ftool MAKETIME, filtering the data using SEFILTER and extracting spectra using the ftool SEEXTRCT. Event lists were created using the ftool DECODEEVT, responses created using PCARSP and background files created by running the tasks PCABACKEST and SAEXTRCT. Unless otherwise stated, only data from Proportional Counter Unit (PCU) 2 was extracted. It should be noted that PCU2 has zero response in channel 10 hence there are gaps in some figures at ~6 keV, but these counts are redistributed to other channels. This is a result of gain and offset corrections which attempt to match the energy scales in different PCU detectors (Jahoda, 1996).

I used variability analysis software written by Phil Uttley to produce power-spectra, lag vs. energy spectra and covariance spectra (Wilkinson & Uttley, 2009) from the raw event lists and GTI files. Only complete segments of 64 s duration were used to construct the data products[1]; segments containing any gaps that were not included in the GTI files, were ignored.

The code makes use of the cross-correlation theorem, which states that the Fourier transform of the cross-correlation of two functions is equal to the product of one Fourier transform with the complex conjugate of the other. The cross spectrum is obtained for all channels relative to a reference band with good signal-to-noise and the average value of the cross-spectrum over all segments is recorded in a master-file for each frequency bin. In a similar manner, the power spectrum of the reference band and all channels of interest are also recorded. It is therefore possible to rapidly generate power spectra, covariance spectra and lag versus energy spectra over frequency ranges of interest. Further details of these methods are discussed in section 1.6.2.

It should briefly be noted that, throughout this work, all covariance spectra were extremely similar to standard rms spectra (i.e. the spectral coherence was high). I will still continue to use the covariance spectrum however, as it is a better tool with which to measure variability; it has smaller statistical errors and is less biased than the rms when signal-to-noise is low (see chapter 2 for more details). For the purposes of this work, it can simply be thought of as a variability spectrum.

All spectra were fitted over the range 3.0-25.0 keV using XSPEC (Arnaud, 1996) version 12.6 with a 0.5% systematic error (unless otherwise stated) to allow for uncertainties in the instrumental response. Figure 4.1 shows the significant section of the 2010 hardness-intensity diagram that is explored in this work.

In section 4.3 I examine the variability spectra of the QPO and demonstrate that the disc variability present at lower-frequencies is markedly reduced in covariance spectra extracted over the QPO frequencies. Having established that only the hotter innermost parts of the disc contribute to the variability of the QPO, I go on to explore the lag vs Energy spectrum of the QPO in section 4.4. The lag spectra show strong evidence for blackbody variations which *lead* power-law variations in the QPO spectrum, giving rise to the possibility that the disc could drive the QPO.

---

[1] A bin-size of 0.0009765625 was used with 65536 bins per segment. This gave a frequency range of 0.016-512 Hz for frequency products.

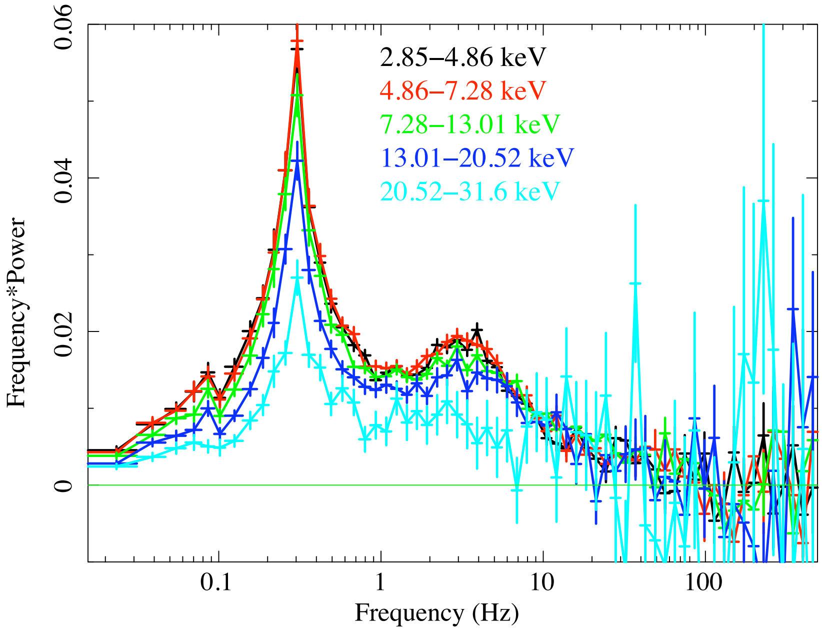

Figure 4.2: Top: Power spectrum made from the observations 95409-01-13-00, 95409-01-13-01, 95409-01-13-02 and 95409-01-13-04.

4.3 Power and Covariance Spectra

The integrated power spectrum, with the appropriate choice of normalisation, is equal to the variance over a given frequency range. Plotting power spectra as a function of energy is a crude way of looking at how the variability of a source changes with energy. Figure 4.2 shows a power-spectrum from four combined observations in the upper right-hand branch of the HID (figure 4.1) demonstrating a QPO located at approximately 0.3 Hz, surrounded by broadband noise. The fractional rms of these features decreases with increasing energy across the frequency range ∼0.01 to 6 Hz. As one moves up the right hand branch of the HID and leftwards along the top branch, the QPO continues to increase in frequency up until around 6 Hz and the band-limited noise component gradually disappears. A QPO at about 6 Hz showing no associated band-limited noise is known as a type-B QPO (Belloni, 2009; Casella, Belloni, & Stella, 2005), and the region of the HID where the type-B QPO is present and the rms variability drops has been referred to as “the zone” (Fender, Homan, & Belloni, 2009). Type-B QPOs have been marked with stars in the HID of figure 4.1, and in the zone, all of the significant variability power resides in the type-B QPO (and its small associated harmonic). In the remainder of this chapter I shall concentrate on observations within or adjacent to this zone.

Spectral fits were performed to covariance spectra obtained over frequencies corresponding to the QPO frequency and, in observations just prior to the zone, a lower-frequency band below the QPO. The latter is representative of the low-frequency band-limited noise which is only present prior to the onset of the true type-B QPO.

The model PHABS*(DISKBB+NTHCOMP+RDBLUR*REFXION*NTHCOMP) was fitted[2] to the mean and low-frequency spectra, but better fits were obtained to the QPO variability spectra using a simple blackbody model, BBODY, rather than the multicolour disc component DISKBB. Therefore, the mean and low-frequency covariance spectra are fitted with a DISKBB model, whilst the QPO covariance spectra are fitted with a simple BBODY. The reason for including two NTHCOMP components is simply that one is convolved with REFXION to produce the reflection component.

4.3.1 Just prior to the zone

Figures 4.3 and 4.4 show power spectra from the combined observations 95409-01-14-05 and 95409-01-15-00 and from 95409-01-15-01 respectively. These are the final three observations in the HID which demonstrate lower frequency broadband noise prior to the onset of the zone. The QPO in figure 4.3 is at ∼4 Hz and in figure 4.4 it has moved up to ∼6 Hz. The QPO variability is dominated by higher energies i.e. the fractional rms of the QPO increases with increasing energy. This is most likely due to the combination of the large average disc component in the mean spectrum (red) and the relatively small contribution of the disc in the variable spectrum across the QPO frequencies (black). The variable low-frequency black body (blue) actually exceeds the mean (red) at ∼10 keV, which is probably unphysical as it suggests variability in excess of 100% rms. This could however be due to the difficulty in constraining the shape of the spectral component at these energies.

Both covariance spectra show reflection features, but the main difference between the two is that at low frequencies (blue) the rms variability of the black body component is significantly higher, and that of the power-law significantly lower, than at the QPO frequency. For the QPO frequency range of figure 4.4 (5-8 Hz), the blackbody rms is approximately 0.2% compared to ∼8.5% at low frequencies (0.3-4 Hz). The very weak black body component is not formally required in the fits over the QPO frequency, but the inclusion of this component is justified later when I discuss the lag spectra.

---

[2] The lack of RXTE soft coverage below 3 keV made REFXION a more appropriate model in this case. The effects of the extra soft ionising flux due to the disc on the reflection spectrum are not important because the affected features are below 3 keV.

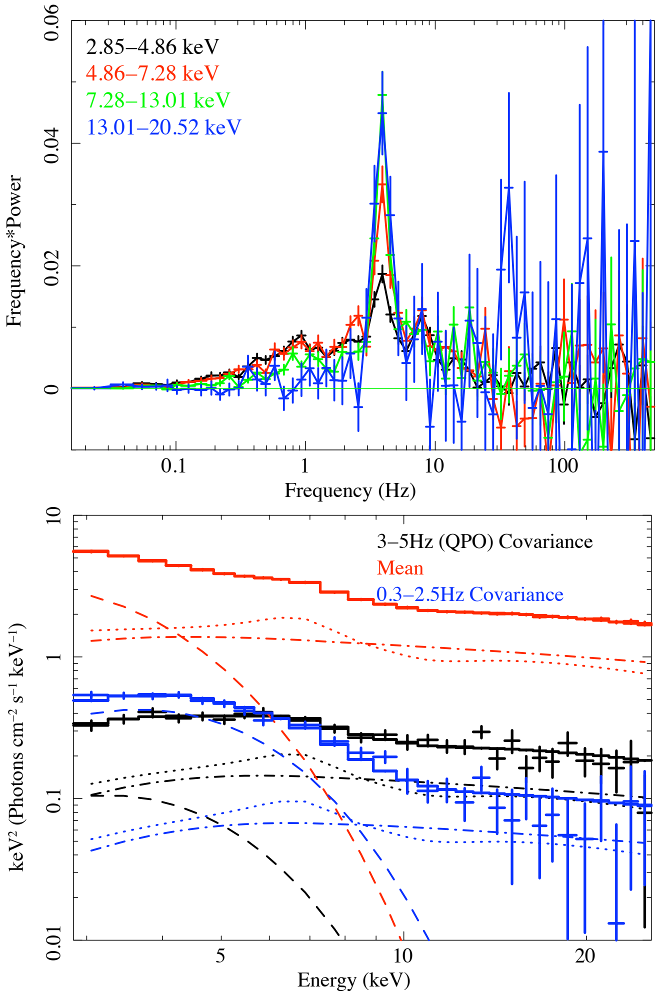

Figure 4.3: Top: Power spectrum made from the observations 95409-01-14-05 and 95409-01-15-00. Bottom: Unfolded spectra showing the relative contributions of disk blackbody (dashed), thermal Comptonisation (dash-dotted) and reflection (dotted) components in the mean and covariance spectra for these observations combined.

4.3.2 In the zone

Figure 4.5 shows a power-spectrum from all observations within the area of the hardness-intensity diagram known as the “zone”, at a hardness ratio of ∼0.2-0.3 as defined in figure 4.1. The low-frequency band-limited noise is no longer present, and the variability of the QPO, which lies just below 6 Hz, is again dominated by higher-energies. The QPO covariance spectra demonstrates slightly higher (0.8%) blackbody rms variability than in figure 4.4, but this is still significantly smaller than the low-frequency blackbody rms which is observed prior to the zone. The spectral fits (table 4.1) indicate that only the hottest innermost part of the disc contributes to the variability, which is why a simple hot (∼0.9 keV) blackbody component better

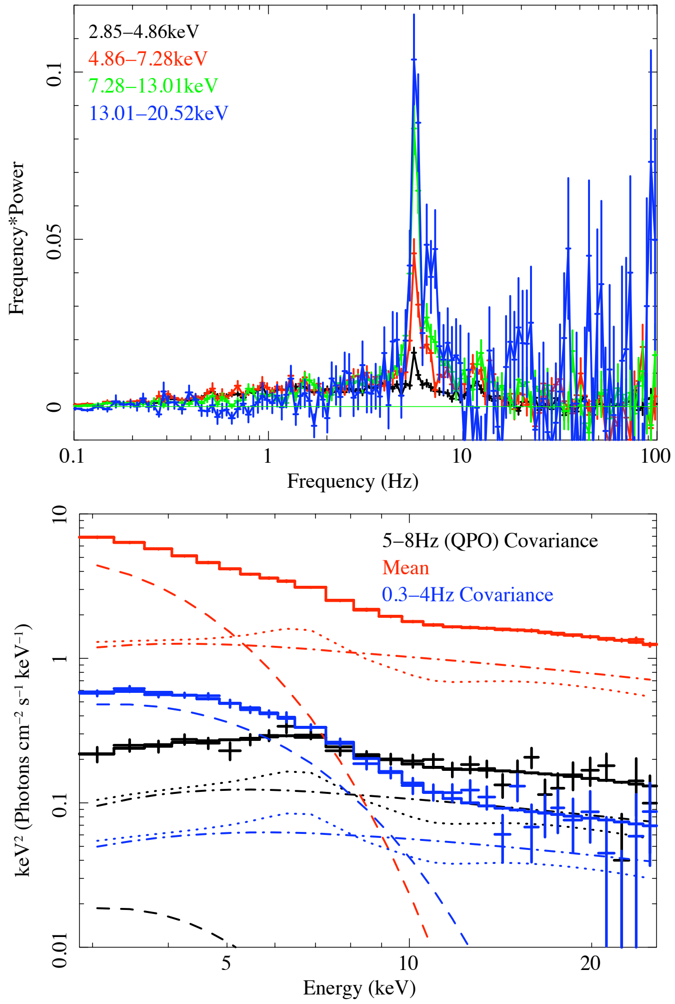

Figure 4.4: Top: Power spectrum made from the observation 95409-01-15-01. Data from PCUs 2 and 4 were used to improve the signal-to-noise. Bottom: Unfolded spectra showing the relative contributions of disk blackbody (dashed), thermal Comptonisation (dash-dotted) and reflection (dotted) components in the mean and covariance spectra for this observation.

fits the data than a multicolour disc component.

4.3.3 Post-zone

Figure 4.6 shows a power-spectrum from three combined observations to the left of the “zone” in the HID with a covariance spectrum obtained for a frequency range representative of the low-frequency noise (0.3-5 Hz). The QPO is no longer seen in the power-spectrum.

The spectra demonstrate a similar level of blackbody variability (0.7% rms) to that measured in the QPO from within the zone, but importantly nothing like the levels of disc variability seen in the pre-zone band-limited noise. This suggests that

Table 4.1: Fits to the QPO, Mean and Low-frequency spectra.

Parameter	Before Zone			In zone		Post-zone	
	QPO	Low-freq	Mean	QPO	Mean	Low-freq	Mean
BB_{kT}(keV)	$0.76^{+0.16}_{-0.30}$	$1.23^{+0.07}_{-0.05}$	$0.81^{+0.02}_{-0.01}$	$0.93^{+0.06}_{-0.04}$	$0.82^{+0.01}_{-0.01}$	$1.16^{+0.49}_{-0.44}$	$0.80^{+0.01}_{-0.01}$
A_{BB}	$5.3^{+7.4}_{-4.8}\times10^{-4}$	34^{+2}_{-1}	2185^{+29}_{-36}	$2.13^{+0.22}_{-0.28}\times10^{-3}$	2462^{+23}_{-18}	9^{+4}_{-4}	3854^{+24}_{-27}
Γ	$2.33^{+0.02}_{-0.02}$ (tied)			$2.47^{+0.02}_{-0.02}$ (tied)		$2.35^{+0.01}_{-0.01}$ (tied)	
R_{in} (R_g)	22^{+17}_{-6} (tied)			25^{+52}_{-17} (tied)		23^{+33}_{-13} (tied)	
log Xi	$4.0^{+**}_{-0.1}$ (tied)			$3.8^{+0.1}_{-0.1}$ (tied)		$3.7^{+0.2}_{-1.2}$ (tied)	
Inc.	37^{+5}_{-6} (tied)			43^{+5}_{-7} (tied)		30^{+8}_{-17} (tied)	
Ref Frac	$0.89^{+0.50}_{-**}$ (tied)			$0.54^{+0.07}_{-0.11}$ (tied)		$0.58^{+0.10}_{-0.20}$ (tied)	
χ^2/ d.o.f.	60/71			76/46		42/43	
RMS_{BB}	0.2%	8.5%	N/A	0.8%	N/A	1.0%	N/A
RMS_{pow}	10%	6%	N/A	14%	N/A	10%	N/A

The emissivity was fixed at -3.0 and R_{out} was fixed at 1000 R_G. Tied indicates that these parameters were free to vary, but constrained to be the same for all data-sets. ** indicates that fit parameters pegged at upper limits during error fitting. Quoted errors are at the 90% confidence level. The mean and low-frequency spectra were fitted using a DISKBB model, where as QPO variability spectra were fitted using a simple BBODY model. Blackbody RMS values were obtained by integrating the flux of these components from 0.01-20 keV. Given that the seed photon temperatures for thermal Comptonisation were therefore different, power-law RMS is best estimated from the unfolded spectra rather than using the normalisation from spectral fits which is defined at 1 keV. A 0.5% systematic was used for these fits.

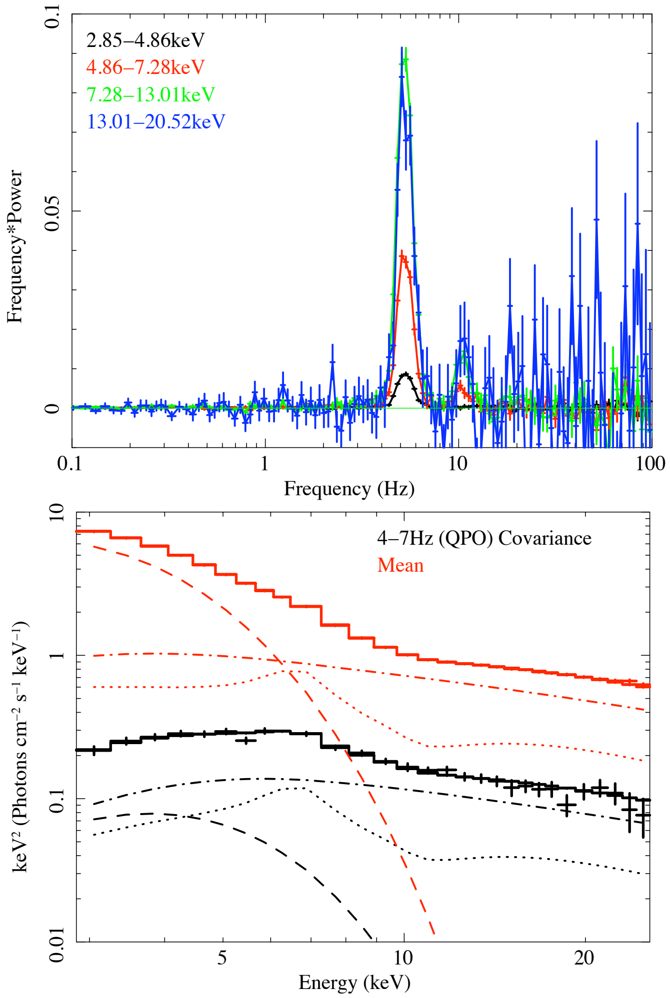

Figure 4.5: Top: Combined power spectra from the "zone" where the band-limited noise disappears and the QPO is classified as type B. This spectrum is made from observations 95409-01-15-02, 95409-01-15-06, 95409-01-17-05, 95409-01-17-06, 95409-01-18-00, 95335-01-01-07, 95335-01-01-00, 95335-01-01-01, 95335-01-01-05, 95335-01-01-06, 95409-01-18-05 and 95409-01-19-00. Bottom: Unfolded mean and covariance spectrum for these observations combined.

the disc has largely stabilised, and this could be linked to the fact that no more QPO features are seen in the power-spectrum to the left of the zone.

4.4 Lag Spectra

Figures 4.7 and 4.8 show the two characteristic lag spectral shapes observed over the QPO frequency and low-frequency noise respectively. The model used to fit these spectra are discussed below. Both lag spectra follow the typical log-linear relation at high energies, but there is a sharp break at around 6 keV in the type-B QPO lag

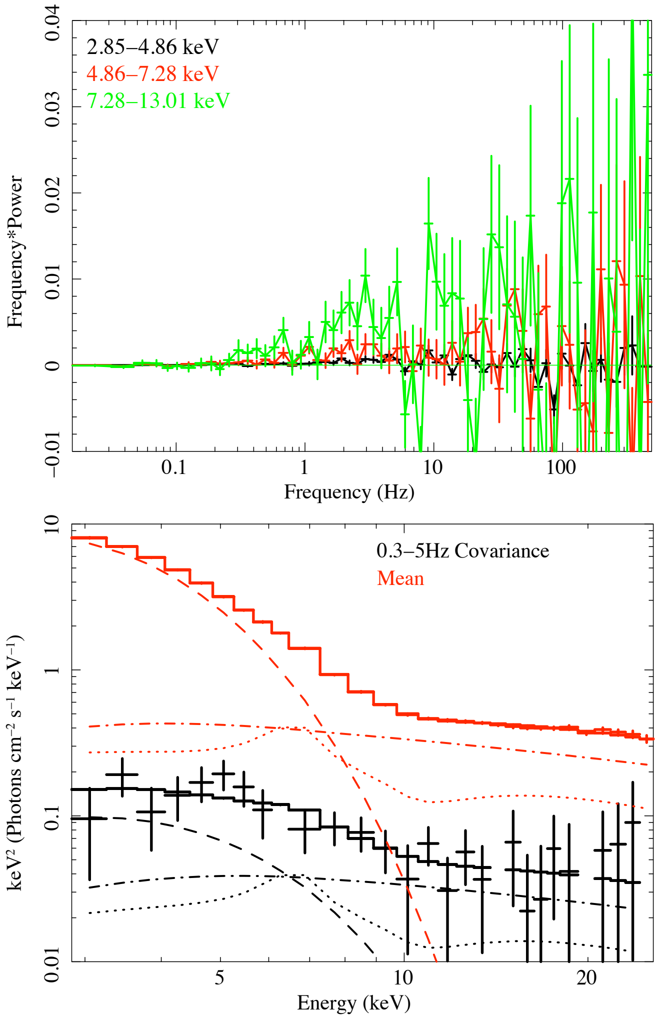

Figure 4.6: Top: Power spectrum made from the combined observations 95409-01-15-03, 95409-01-16-01 and 95409-01-16-06 to the left of the zone in the hardness-intensity diagram (figure 4.1). Bottom: Unfolded spectra for these combined observations.

spectrum (figure 4.7), and a flattening to a constant lag at low energies in the band-limited noise (figure 4.8). This is highly suggestive of a disc contribution to the lag, supporting the spectral fits of table 4.1, and justifying the addition of a variable black body component. Comparing the break in the lag spectrum of figure 4.7 to that of figure 2.9, suggests a similar origin for this feature, but with a significantly higher disc temperature leading to a break at higher energies. This result suggests that the disc component is leading the power-law emission, and could possibly be responsible for driving the QPO.

At lower-frequencies (figure 4.8), where the disc is more variable, the lag vs. energy spectrum shows a constant component at low energies. This implies that the disc contributes a constant lag which dominates the power-law lag at these energies.

The covariance spectra of the QPO clearly shows a far less variable disc component, so the blackbody lag cannot dominate as it does at low-frequencies, but instead causes a break in the lag vs. energy spectrum at ~6 keV as it competes with the power-law lag.

Phil Uttley developed a simplistic model of the lags in XSPEC computed as:

$$E_{lag} = \frac{F_{pow+refl}\tau_{pow} + F_{BBseed}\tau_{pow} + F_{BB}\tau_{BB}}{F_{pow+refl} + F_{BBseed} + F_{BB}} \tag{4.1}$$

This is effectively a weighted mean lag based on the relative flux contributions from the spectral components. The model assumes the standard log-linear dependence of the power-law lag on energy (Kotov, Churazov, & Gilfanov, 2001), and the flat shape of the low-frequency lag spectrum at low energies (figure 4.8) motivated the choice of a constant black body lag. An extra black body (model BBODY in XSPEC) term is included in the lag model, labelled BBseed above. This represents the black body component due to thermal reprocessing, and therefore (due to the very small light travel time) this component is assumed to contribute nothing to the black body lag; as an approximation this is instead treated in the model as contributing to the log-linear power-law lag. This seed component provides the seed photons for thermal Comptonisation. In this way, this very simplistic lag model can disentangle the reflected and intrinsic contributions to disc variability.

4.4.1 Lag model fits

4.4.1.1 QPO Lags

This lag model was fitted simultaneously with the covariance and mean spectra obtained over the type-B QPO frequencies. For simplicity, and so the normalisation of the black body component responsible for the lag could be compared directly with that of the mean, the mean and covariance/lag spectra were fitted with multicolour disk black body spectra and their temperatures were tied. Note that this is different to earlier spectral fits in which a simple black body component was used for the variable QPO spectrum and a multicolour disc was used for the mean and low-frequency thermal emission. The model is essentially the same as in table 4.1 with the subtle difference that the thermal emission now has two contributions - one from a multicolour disk, and another from a zero-lag black body component. The model fit is the solid line in figure 4.7 which fits the data, and particularly the break, remarkably well.

The extra black body component, which provides hotter seed photons for thermal

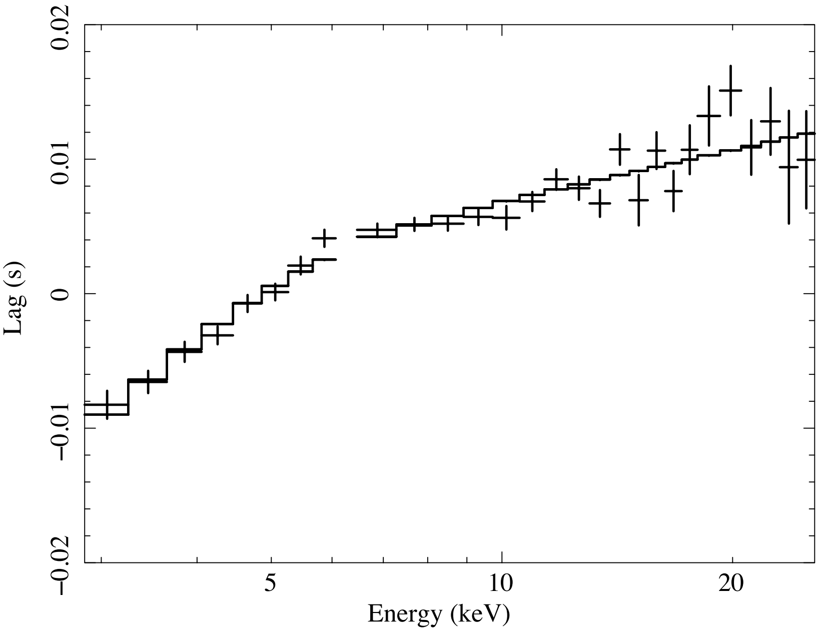

Figure 4.7: Lag vs Energy Spectrum over the QPO frequencies (4-7 Hz) for the type-B QPO. Observations were combined as in figure 4.5

Comptonisation, changes some aspects of the spectral fit as can be seen in table 4.2. The spectral slope is slightly harder, the inner radius much larger and the reflection parameters are different. However, the fundamental idea is the same, that there is an intrinsically variable disc component which *leads* the power-law by ≈0.14s. Comparing the disk normalisations directly, the variable contribution is extremely small, only 0.25%. This implies that intrinsic disc variations must be happening at the very inner edge of the disc so they are unable to modulate very much of the disc emission. The power-law variability at ∼20 keV is ∼15% as can be seen from figure 4.5, so it is clear that the disc variations in the very inner parts must be of this order to propagate in to the power-law region. However, this disc variability can only propagate inwards and modulate the disc emission inwards of this point, so in rms terms it is very small.

4.4.1.2 Low-frequency Lags

From the spectral fits in figure 4.4, the disc component is much stronger in the frequency band 0.3-4 Hz. The fact that the black body dominates at lower energies, means that the constant lag also becomes dominant. This is exactly what is seen in the lag vs. energy spectrum in figure 4.8 for observation 95409-01-15-01. Due to difficulties in modeling the overlap region between the log-linear power-law and disc I could not successfully fit the data using our simple lag model. However, the

Table 4.2: Fit parameters from lag model fitted over type-B QPO frequencies.

Parameter	Lag/Covariance	Mean
$\mathrm{Disk_{kT}}$ (keV) (Tied)	$0.80^{+0.02}_{-0.02}$	
$\mathrm{A_{disk}}$	6^{+11}_{-11}	2351^{+84}_{-84}
$\mathrm{Seed_{kT}}$(keV)	$1.25^{+0.07}_{-0.07}$	$0.93^{+0.09}_{-0.09}$
$\mathrm{A_{seed}}$	$2.3^{+0.8}_{-0.8} \times 10^{-3}$	$2.3^{+0.7}_{-0.7} \times 10^{-2}$
Γ (Tied)	$2.37^{+0.08}_{-0.08}$	
BB Lag (Tied)	$-0.15^{+0.02}_{-0.02}$	
$\mathrm{R_{in}}$ ($\mathrm{R_g}$) (Tied)	83^{+111}_{-111}	
log Xi (Tied)	$3.4^{+0.3}_{-0.3}$	
Inclination	43 (F)	
Ref Frac (Tied)	$0.28^{+0.18}_{-0.18}$	
χ^2/ d.o.f.	89/66	

Tied indicates that these parameters were free to vary, but constrained to be the same value for all data-sets, F indicates that parameters were frozen. A 0.5% systematic was used for these fits.

lag spectra is qualitatively in agreement with the dominant black body component contributing a constant lag at lower energies, flattening off the lag spectrum from the typical log-linear relation at higher energies.

4.5 Conclusions

It is clear from fits to the covariance spectra in section 4.3 that the disc variability is greatly reduced over the QPO frequencies. This suggests that at these frequencies the QPO is occurring in the vicinity of the inner edge of the thin disc, or possibly even at the Innermost Stable Circular Orbit (ISCO) if the disc is not truncated, where intrinsic variations in the disc can only modulate a tiny fraction of the total emitted disc luminosity. As such, although these variations can be passed in to the power-law region and fully modulate the power-law (so the power-law variability more accurately reflects the intrinsic amplitude of $\dot{M}$ fluctuations), they are barely noticeable in the disc due to dilution by a large constant thermal component from larger radii. The disc modulations that do show up significantly have propagated through a larger range of radii, hence the larger disc variability component present in the low-frequency (larger radius) covariance spectrum of figures 4.4 and 4.3. The

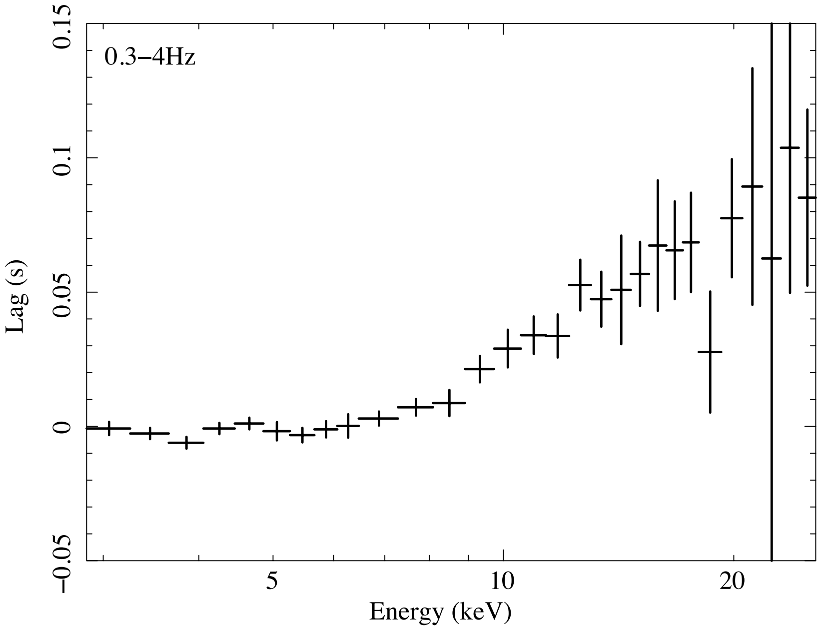

Figure 4.8: Lag vs Energy Spectrum for the low-frequency (0.3-4 Hz) band-limited noise component, see figure 4.4

.

fits to the QPO covariance spectra support this idea, indicating small, hot black body components consistent with the inner edge of the disc. If the QPO spectrum was obtained when the QPO was lying at lower frequencies, this region of turbulence would be lying at a larger radius and would be able to modulate all of the disc inwards of the turbulent region. This would give rise to a much larger variable blackbody component, as was seen in chapter 2. Further support for this scenario comes from the evolution of the QPO itself. The QPO frequency increases, indicating that some region of turbulence in the mass accretion flow moves inwards until it reaches $\sim$6 Hz, a frequency that is broadly consistent with the thermal or viscous timescale close to the ISCO (the latter only for a large scale height flow).

Fits using a simplistic lag model indicate that the black body contributes a constant lag component and imply that the disc variability responsible for generating the QPO is less than 1% rms. The area to the left of the zone in the HID, where the QPO is no longer present in the PSD, could correspond to the region where the disc becomes stable. When the QPO switches off, we could be seeing the very inner edge of the disc finally become stable.

Things should be made as simple as possible, but not any simpler.

ALBERT EINSTEIN (1879 - 1955)

5

Phase-resolved spectroscopy of continuum and reflection in SAX J1808.4-3658

I perform phase-resolved spectroscopy of the accreting millisecond pulsar, SAX J1808.4-3658, during the slow-decay phase of the 2002 outburst. Simple phenomenological fits to RXTE PCA data reveal a pulsation in the iron line at the spin frequency of the neutron star. However, fitting more complex spectral models reveals a degeneracy between iron-line pulsations and changes in the underlying hotspot blackbody temperature with phase. By comparing with the variations in reflection continuum, which are much weaker than the iron line variations, one can infer that the iron-line is not pulsed. The observed spectral variations can be explained by variations in blackbody temperature associated with rotational Doppler shifts at the neutron star surface. By allowing the blackbody temperature to vary in this way, I also find a larger phase-shift between the pulsations in the Comptonised and blackbody components than has been seen in previous work. The phase-shift between the pulsation in the blackbody temperature and normalisation is consistent with a simple model where the Doppler shift is maximised at the limb of the neutron star, $\sim 90^\circ$ prior to maximisation of the hot-spot projected area.

5.1 Introduction

SAX J1808.4-3658 was the first accreting millisecond X-ray pulsar (AMXP) to be discovered (Wijnands & van der Klis, 1998). Lying some 3.5 kpc distant (Galloway & Cumming, 2006), the neutron star spins with a frequency of $\sim$401 Hz and is thought to be orbiting a low-mass brown-dwarf companion (Bildsten & Chakrabarty, 2001) with a 2.01 hr orbital period (Chakrabarty & Morgan, 1998). The established picture is that such AMXPs are recycled to millisecond periods from more slowly rotating neutron stars, due to the transfer of angular momentum from the accretion flow provided by the companion (Bhattacharya & van den Heuvel, 1991). In this sense, the AMXPs bridge the gap between low mass X-ray binaries (LMXB) and rotation powered millisecond pulsars.

The accretion flow in AMXPs differs from that in black hole X-ray binaries (BHXRB) due to the stellar magnetic field and the solid neutron star surface. The magnetic field of SAX J1808.4-3658 is $\sim 10^8$ G (Hartman et al., 2008) and this is sufficient to channel accreting material approaching within a few neutron star radii along field lines towards the magnetic poles. The funneled gas passes through an accretion shock before falling on to the magnetic poles. X-ray observations of AMXPs made with the *Rossi X-ray Timing Explorer* (RXTE) and *XMM-Newton* (XMM) have discovered distinct spectral components originating from these sources. The accretion disc and neutron star surface contribute to a soft component up to $\sim$10 keV, and Comptonisation in the shock region (most likely of seed photons from the impact hot-spot) produces a harder component extending to $\sim$100 keV (Gierliński, Done, & Barret, 2002). Recent *XMM-Newton* observations of SAX J1808.4-3658 have shown two distinct blackbodies at soft energies plus a hard component, interpreted as an accretion disc, a neutron star hot-spot and an accretion shock (Patruno et al., 2009; Papitto et al., 2009).

In an analogous manner to reflection in BHXRB (Fabian et al., 1989), it is thought that Comptonised photons reflect off the geometrically thin optically thick accretion disc producing a Compton reflection hump and fluorescent iron Kα line emission at $\sim$6.4 keV (see Cackett et al. 2010 for a review of broadened iron lines in neutron star LMXBs). The shape of the line provides information about the distance of the line-forming region, since reflection occurring close to the compact object produces a characteristic asymmetric profile due to Doppler-broadening and gravitational redshift. Observations of SAX J1808.4-3658 have revealed evidence suggestive of such a broadened iron line (Cackett et al., 2009b; Papitto et al., 2009). Iron Kα lines are also of particular importance because they place a constraint on the magnetospheric radius. It is, as yet, unclear how the magnetic field of a magnetised star truncates the disc,or what effect the star's rotation has on the disc inner edge.

The X-ray emission from AMXPs is pulsed due to misalignment of the spin and magnetic poles. As the hot-spot and magnetically channelled accretion column rotate around the spin axis, the projected area and the magnitude of the Doppler shift changes, causing emission to be pulsed at the spin frequency. It is therefore not unreasonable in this scenario to imagine that changes in the line shape and/or energy with phase might also occur. For instance, if the accretion column illuminates significantly different parts of the disc with phase, reflection occurring from approaching and receding parts of the disc should display a change in line energy with phase. Exploring the variation of the line properties with phase, as well as the phase dependent correlation between the line equivalent width (EW) (or normalisation) and the reflection hump, might be a valuable window on the formation of this spectral feature. The iron Kα feature in SAX J1808.4-3658 has been known about for many years (Gierliński, Done, & Barret, 2002), and it is now known that this feature might be relativistically broadened (Cackett et al., 2009b; Papitto et al., 2009). Therefore, it is of interest whether this feature is also pulsed at some level, which might be expected if the illuminating continuum is also pulsed as seen from the inner disc (which might be expected in certain geometries, e.g. where a part of the disc is shielded by the neutron star itself).

Using the correct orbital ephemeris and referencing the photon arrival times to the Solar System barycenter, it is possible to define an arbitrary phase-zero and 'fold' all of the incoming photons in to phase-bins representative of a full rotation of the neutron star. By examining the energy spectra of photons from individual phase bins, one can perform phase-resolved-spectroscopy. A phase-resolved analysis was performed of the 1998 outburst (Gierliński, Done, & Barret, 2002), and the self-consistent continuum reflection and iron-line were found to be consistent with having a constant value as a function of phase. In this work, I produce phase-resolved spectra of the best-sampled and best-studied 2002 outburst of SAX J1808.4-3658 as observed by *RXTE* over the 'slow-decay' of the outburst (Hartman et al., 2008) where pulse profiles are most stable and the phase-resolved spectrum can be investigated with high signal-to-noise. I shall explore changes in the iron-line properties with phase, and investigate the viability of the currently accepted picture of the broadened iron-line emission in AMXPs.

5.2 Observations and Data Reduction

I have concentrated on RXTE observations of SAX J1808.4-3658 from the slow-decay phase (MJD 52564-52574) of the 2002 outburst where the pulse profile is the most stable and the data is best sampled (in date order OBS ID 70080-01-01-02 to 70080-01-03-03 inclusive). The reader is referred to Figure 3 of Hartman et al. (2008) for a light curve of the outburst illustrating the data segment I have used. For simplicity, only data taken with the E_125US_64M_0_1S event mode of the *RXTE* Proportional Counter Array (PCA) were used in this work. Although during these observations different PCA detectors were switched on, I have only analysed data from PCU 2 which was always on, in order to ensure consistency. Gain and offset corrections, which attempt to match the energy scales in different PCU detectors, assign zero response in different channels of different PCUs (Jahoda, 1996). Combining different detectors involves weighting different detector responses, and this could introduce an unknown systematic bias. In total, 64 event files were analysed with a total exposure of 167 ksec, which provided sufficient signal to noise for phase-resolved spectroscopy using 16 phase bins.

The photon arrival times in each event file were corrected to the Solar system barycenter with the ftool FAXBARY. The photon phases were determined by using a high-order polynomial to “whiten” the phase residuals and increase the signal to noise of the pulsations. This corrects for ‘X-ray timing noise’, changes in phase thought to be caused by variations in the location of the hot-spot on the neutron star surface (Patruno, Wijnands, & van der Klis, 2009). Additionally, the arrival time of photons was corrected for the orbital motion of the binary using a first-order approximation as outlined, for example, in Papitto et al. (2005). A folded pulse profile was created for each separate event file, and fitted with a simple constant offset plus a sinusoid. During the slow-decay, pulse profiles have been shown to be stable and nearly sinusoidal (Ibragimov & Poutanen, 2009; Hartman et al., 2008). By fitting each event file with the best fitting sinusoidal function, an offset could be determined for each event file to accurately align the different files in phase for subsequent summation. Custom code was written to select the photons from PCU2 only and produce separate FITS files containing events from each of the 16 different phase bins for each event file. The ftool SEEXTRCT was then used to produce PHA spectra for each phase bin.

Background files were created using the ftool PCABACKEST, and extracted using SAEXTRCT over contemporaneous good time intervals created using the ftool MAKETIME. The ftool MATHPHA was used to sum pha files from each respective phase bin and sum the background spectra. A weighted PCU2 response file was created (due to any variations in the response over time) from all observations using PCARSP and ADDRMF. Care was taken to adjust the exposure of the phase-resolved spectra to reflect the fact that each spectrum only contained 1/16th of the total exposure. Phase averaged PCU2 spectra were also obtained from the same observations.

The pre-processed High Energy X-ray Timing Experiment (HEXTE) cluster A spectra from the same observations were summed together to provide some constraints on the phase-averaged power-law spectral component at higher energies.

Throughout this work, spectral fitting was performed using XSPEC version 12.5.1 (Arnaud, 1996) with a 0.5% systematic error for PCA and HEXTE data during fitting. It should be noted that the PCU 2 data has zero response in channel 10, but these counts are redistributed to other channels, hence the gap in the data in Figure 5.2.

5.3 Analysis and Results

5.3.1 Phase-averaged spectrum

Phase-averaged spectra of SAX J1808.4-3658 from the slow-decay phase of the 2002 outburst have been fitted before (Ibragimov & Poutanen, 2009). It is therefore known that a simple power-law fit shows residuals that are consistent with Compton reflection and blackbody hotspot emission. In both the 1998 and 2002 outbursts, thermal Comptonisation models have typically shown photon indices of ~ 1.8 with blackbody temperatures around 0.7 keV and hot-spot areas in the range 20-110 km^2 (Gierliński, Done, & Barret, 2002; Ibragimov & Poutanen, 2009; Poutanen & Gierliński, 2003).

As well as fitting PCA data over 3.0 to 25.0 keV, the HEXTE spectra are also fitted simultaneously over the range 15.0-150 keV to constrain the power-law continuum and cut-off energy. The continuum was best-modelled using the thermal Comptonisation model NTHCOMP (Życki, Done, & Smith, 1999), and reflection was modelled using PEXRIV (Magdziarz & Zdziarski, 1995) and GAUSSIAN components convolved with RDBLUR. Only the reflection component of the PEXRIV model was included. A thermal Comptonisation model is chosen since the hot electrons in the accretion shock are thought to Compton up-scatter the seed photons from the hot-spot, whilst the blurred Gaussian is chosen to model the iron-line feature. All parameters were tied between the two instruments apart from a normalising constant to allow for a calibration offset. The hotspot emission is modelled using a BBODYRAD component. The BBODYRAD model is a single temperature blackbody spectrum parameterised by the temperature and the normalisation $\mathrm{R}^2_{\mathrm{km}}/\mathrm{D}^2_{10}$, where R_{km} is the source radius in km and D_{10} is the distance to the source in units of 10 kpc. The NTHCOMP model is parameterised by the asymptotic power-law photon index, the electron temperature, the seed photon temperature and the normalisation (the photon flux defined at 1 keV in units of photons $\mathrm{cm}^{-2}\mathrm{s}^{-1}\mathrm{keV}^{-1}$). The PEXRIV model describes an exponentially cut-off power-law spectrum reflected from ionised material and is parameterised by the power-law photon index, the power-law cut-off energy, the disc temperature, the disc ionization parameter (Done et al., 1992), the normalisation (photon flux at 1 keV) of the power-law only (without reflection) and a dimensionless reflection scaling factor. RDBLUR is a convolution model taking account of the blurring due to relativistic effects from an accretion disc around a non-rotating black hole, and is parameterised by the power-law index of emissivity, the disc inner radius, the disc outer radius and the inclination. Full parameters of the fit are shown in Table 5.1 and the unfolded spectrum is included in Figure 5.1. The spectral fits reflect the average parameters over the 167 ksec of data that was analysed from the slow-decay phase of the outburst. The parameters of this 'average' fit are consistent with previous work, though it should be noted that as the mass accretion rate drops throughout the outburst, the disc inner edge likely recedes (Ibragimov & Poutanen, 2009), causing changes in the fit parameters. The fits were insensitive to ξ, the ionisation parameter, and the disc temperature so these were frozen at values of 100 erg cm s^{-1} and 10^6 K respectively. The low value of ξ is consistent with the line energy which was constrained to lie between 6.4 and 6.9 keV and pegged at the lower limit during fitting[1]. In order to avoid the PEXRIV power-law cut-off energy becoming unphysical, this parameter was constrained to be equal to three times the value of the electron temperature. Freeing the seed photon temperature for Comptonisation from the blackbody temperature had no statistically significant effect, consistent with the notion that the seed photons for Comptonisation come from the hotspot emission. It should also be noted that the PEXRIV normalisation and reflection fraction are degenerate parameters in these fits hence the large absolute values of reflection fraction quoted in Table 5.1. The relatively poor chi-squared value of the model quoted in Table 5.1 is due to the higher energy HEXTE data. Removing the HEXTE data and fitting only PCA data results in a χ^2/d.o.f of 16.56/18, but it was considered important to include the

---

[1] It should be noted that if the companion is hydrogen deficient, for instance more akin to the degenerate core of a star than a true brown-dwarf, the reflection parameters would change and current models are not strictly applicable.

Table 5.1: Best fitting parameters for the phase-averaged CONS*PHABS*(NTHCOMP + BBODYRAD + RDBLUR*(PEXRIV + GAUSSIAN) model used in section 5.3.1

Parameter	Value
$\mathrm{BB_{kT}}$(keV)	$0.676^{+0.02}_{-0.01}$
$\mathrm{BB_{norm}}$	$130.89^{+10.12}_{-12.87}$
Γ	$1.96^{+0.03}_{-0.03}$
nthComp $\mathrm{KT_e}$ (keV)	$45.53^{+14.08}_{-8.10}$
$\mathrm{nthComp_{norm}}$	$0.051^{+0.004}_{-0.004}$
foldE(keV)	$136.59^{+42.24}_{-24.30}$
$\mathrm{PEXRIV_{norm}}$	0.034(Frozen)
$\mathrm{PEXRIV_{refl}}$	$-3.96^{+0.93}_{-0.69}$
$\mathrm{PEXRIV_{\xi}}$	100(Frozen)
$\mathrm{HEXTE_{const}}$	$0.88^{+0.01}_{-0.01}$
$\mathrm{R_{in}}$ ($\mathrm{R_G}$)	$18.41^{+29.15}_{-12.41*}$
Emissivity	$-3.30^{+1.1}_{-6.7*}$
Fe line E (keV)	$6.40^{+0.08}_{-0.00*}$
Fe line width (keV)	0.01(Frozen)
Fe norm (10^{-4})	$6.11^{+2.70}_{-3.04}$
χ^2 / d.o.f	97.18 / 62

Inclination was fixed at 60°, R_{out} fixed at 1000 R_G, nH fixed at 0.113×10^{22} and solar abundances assumed. Upper/lower error limits labelled with an asterisk show that the fit parameters were pegged, at times indicating that the fit was not particularly sensitive to this parameter.

HEXTE data during fitting to model better the electron cut-off and thermal Comptonisation continuum. Grouping the HEXTE data in to bins of 4 channels each in this fit improves the χ^2/dof to 38.44/28 (a null hypothesis probability of 0.09), an acceptable fit given the low number of degrees of freedom. Previous pulse-profile modeling (Poutanen & Gierliński, 2003) has derived a lower limit of 65° for the inclination of this source, but since no eclipses or absorption dips are seen, a value of 60° is assumed throughout this work consistent with previous analysis (Gierliński, Done, & Barret, 2002; Ibragimov & Poutanen, 2009). Any difference in inclination only introduced a systematic shift in the normalisation of spectral components, and therefore did not effect the relative phases of any pulsations.

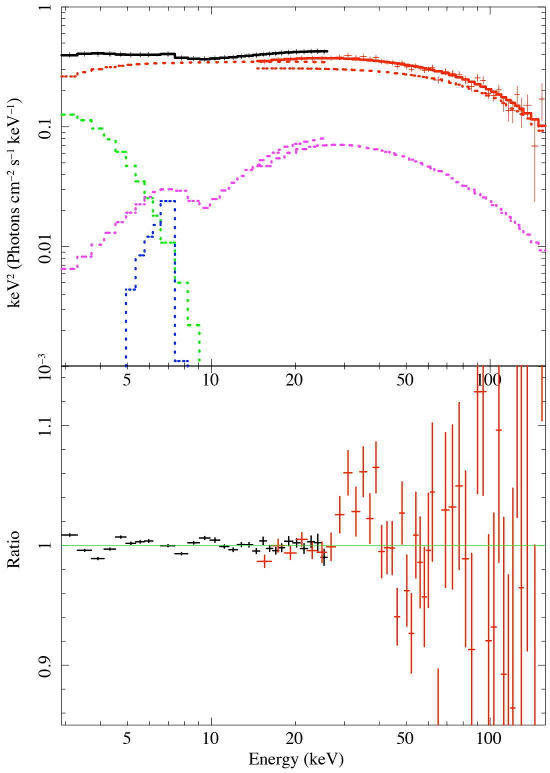

Figure 5.1: Top: Unfolded phase-averaged spectrum (model multiplied by the ratio of observed data to the response folded spectral model) showing iron line, blackbody and reflected power-law components using the CONS*PHABS*(NTHCOMP + BBODYRAD + RDBLUR*(PEXRIV + GAUSSIAN)) model. Bottom: Data to model ratio plot of this fit.

5.3.2 Phase-resolved energy spectra

5.3.2.1 Evidence for a varying iron-line EW with phase

A simple phenomenological fit was performed to the 16-bin phase-resolved data consisting of a PHABS*(POW+BBODYRAD) model. The absorption was fixed at 0.113×10^{22} cm^{-2} as in Ibragimov & Poutanen (2009) (obtained from the HEADAS tool *nh*) and the fit performed over the region 3.0-25.0 keV whilst ignoring the iron-line region of 5.5-10.0 keV. Component normalisations were allowed to be free for each of the 16 different spectra. Having fitted a model excluding the data in the iron-line region, by then including the data in this region one can plot the data-to-model residuals as in Figure 5.2. The plot of the residuals demonstrates a broad iron-line feature and hints at a changing iron-line equivalent width with phase.

In the following sections, I shall explore different models to explain this apparent pulsation of the iron-line with phase.

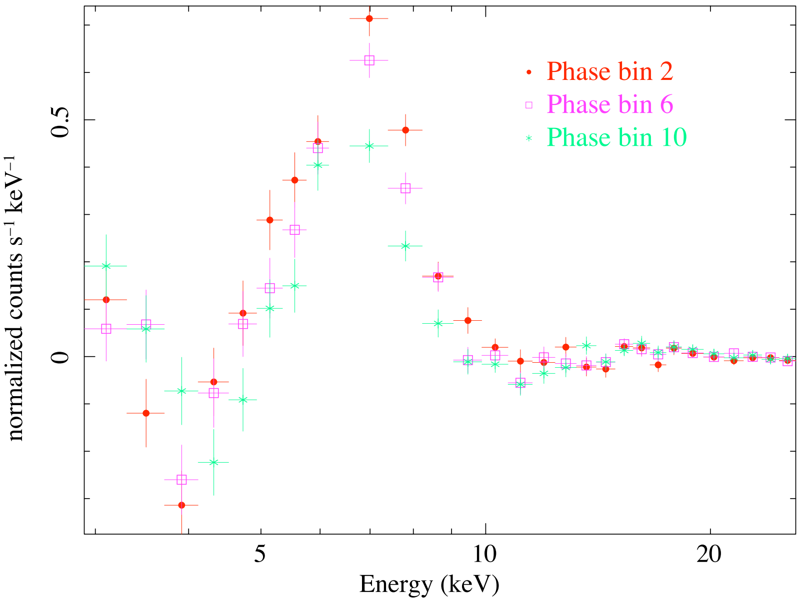

Figure 5.2: Data to PHABS*(POW+BBODYRAD) model residuals showing a broad excess in the iron line region. For clarity only three of the sixteen phase bins are shown here. The slight soft excess is most likely due to the Wien tail of accretion disc emission. The zero point from PCU channel 10 has been removed from this plot as discussed in the last paragraph of section 5.2.

5.3.2.2 Phenomenological Fits

A fit was performed with the model PHABS*(CUTOFFPL+BBODYRAD+DISKLINE), using the 16 phase-resolved spectra over 3.0 to 25.0 keV and the phase-averaged *HEXTE* spectrum over 15.0 to 150.0 keV. The iron line energy was constrained to lie within 6.4 and 6.9 keV and the inclination fixed at 60° as in Gierliński, Done, & Barret (2002) and Ibragimov & Poutanen (2009). With the cut-off power-law and blackbody normalisations free to vary between phase-bins (untied), and the DISKLINE normalisation constrained to its best fitting value across all phase bins (tied), the fit gave a χ^2/dof of 756.52/467. The best fitting DISKLINE R_{in} was 11.9 R_g and the low value (1.63) of power-law photon index (compared to the phase-averaged fits) points to some degeneracy between the power-law and blackbody contributions at soft energies in this simple fit. Untying the DISKLINE normalisation between phase-bins improved the χ^2/dof to 694.46/451 and the spectral components demonstrate the pulsations shown in Figure 5.3. Untying the DISKLINE normalisation simply allows the flux from the line to change with phase, rather than assuming the flux is constant as a function of phase. If the blackbody temperature is untied between phase-bins

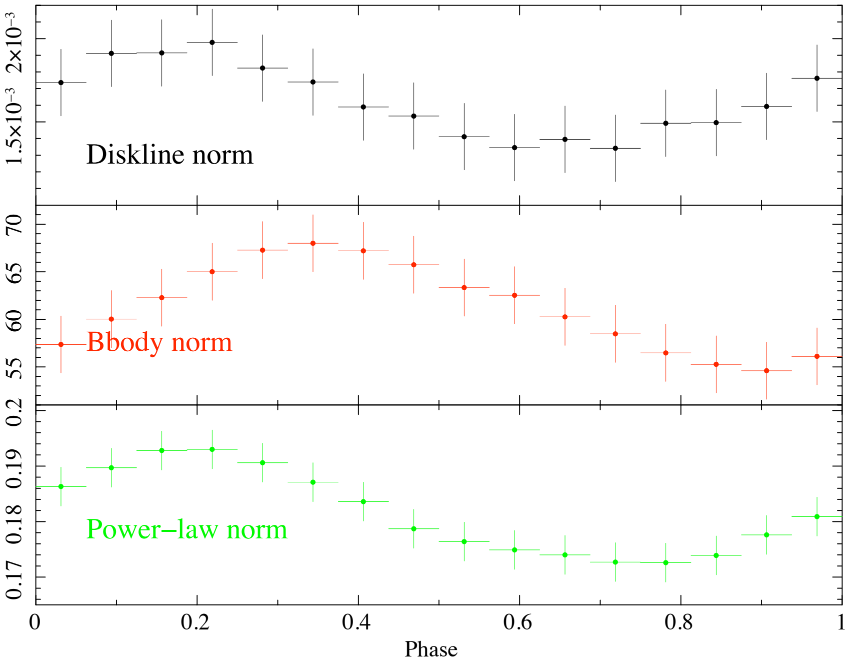

Figure 5.3: Phenomenological fit demonstrating the pulsation in the DISKLINE normalisation with phase. The blackbody temperature was tied between phase bins in this fit. The approximate peak-to-peak change in the line normalisation was 42%, in the blackbody normalisation 20% and in the power-law normalisation 11%.

instead of the DISKLINE normalisation, the χ^2/dof improves to 691.38/451 and the spectral components this time pulsate as shown in Figure 5.4. Untying the blackbody temperature produces an $\sim 80^\circ$ phase-shift in the pulsation of the blackbody normalisation compared to Figure 5.3, suggesting that there is some offset between the Doppler shift of blackbody photons (that affects the temperature measured by an observer at infinity and is dependent on the maximum line of sight velocity) and the projected area of the hot-spot which dominates the blackbody normalisation. It is also interesting to note that the DISKLINE normalisation and kT are in phase in Figures 5.3 and 5.4 respectively. Again, it should be pointed out that the poor χ^2/dof is due to the higher energy HEXTE data used to constrain the parameters in this fit. If a fit is performed excluding the HEXTE data (fixing the now unconstrained high energy cut off to the phase-averaged values) the χ^2/dof improves to 473.58/407. Although the fits obtained with this simple phenomenological model are formally unacceptable, they do provide some physical insight in to the nature of the pulsations in this source which are discussed below. The detailed reflection models explored in section 5.3.2.3 produce much more acceptable values of reduced χ^2.

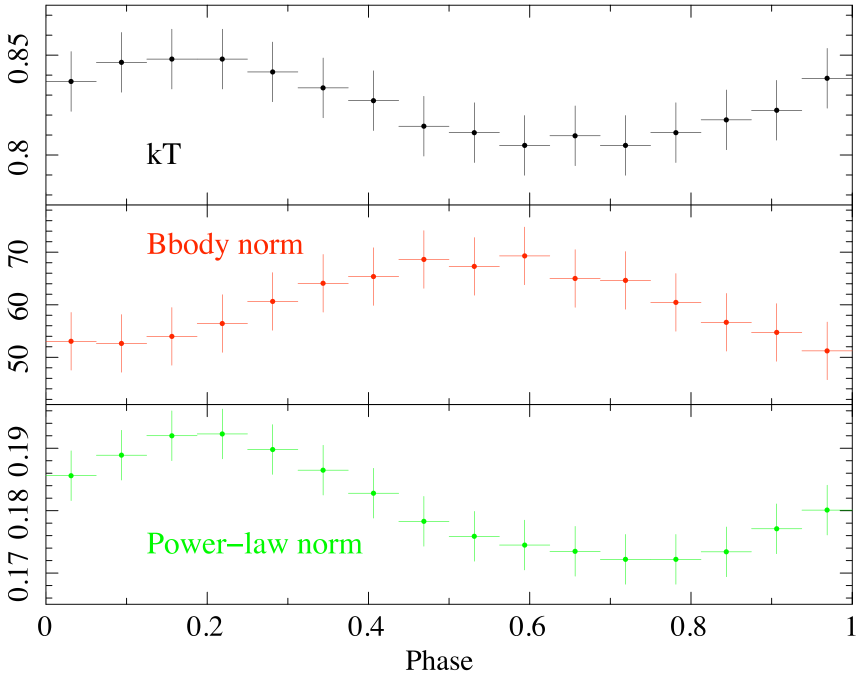

Figure 5.4: Phenomenological fit demonstrating the pulsation in the blackbody temperature when DISKLINE normalisation is tied between phase-bins. The approximate peak-to-peak change in the blackbody temperature was 5%, in the blackbody normalisation 28% and in the power-law normalisation 11%

This preliminary analysis leads to two explanations for the spectral pulsation, which are equally likely on statistical grounds alone. In the first case, the line normalisation is pulsating due to solid angle changes of the line emitting region and in the second case the line normalisation itself is constant, but the changing spectral shape of the blackbody component (governed by temperature changes, possibly due to Doppler effects) introduces a modulation at the spin frequency. It is important to point out here the physical situation that these alternative models are describing. In the first case, which invokes a varying line normalisation, the visible area of line emission changes with phase. This could, for instance, be due to the neutron star self-shielding the line emission from the disc as the system rotates, as shown in Figure 5.5, or due to solid angle changes of the emitting area with phase. In the second scenario, where the line emission is constant with phase, the alignment of the spin and magnetic poles are such that the illumination of the disc by the accretion shock is more or less constant with phase as depicted in Figure 5.6. The amount of observed iron-line emission is therefore fairly constant with phase, and the modulation can be explained solely in terms of the spectral changes in the blackbody component occurring in the same energy channels as the iron-line.

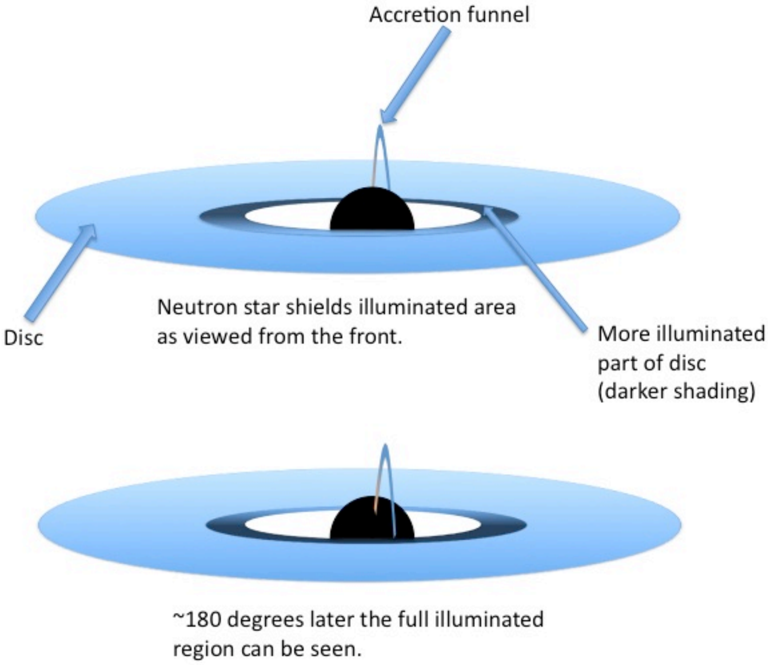

Figure 5.5: Shielding of the reflected emission by the neutron star itself could lead to a variation in the visible area of line emission

5.3.2.3 Fits with reflection models

Having established these two alternative scenarios using the phenomenological fits, the same physically motivated reflection model described in the phase-averaged fits was fitted to the phase-resolved spectra (and *HEXTE* spectra). In the first fit, the normalisations of the BBODYRAD, NTHCOMP, PEXRIV and GAUSSIAN components were untied between phase-bins, whereas the blackbody temperature and seed photon temperature were tied between phase-bins (and tied to each other). Throughout these phase-resolved fits, all parameters constrained to not vary with phase remained very close to the phase-averaged values quoted in Table 5.1. The χ^2/dof for this fit was 455.0/435 and the pulsation of the spectral components with phase can be seen in Figure 5.7.

It is clear from Figure 5.7 that, in this model, the gaussian (iron-line) normalisation is systematically varying with phase, whilst the reflection normalisation shows no clear evidence of doing so. Both the GAUSSIAN and PEXRIV normalisations shown in Figure 5.7 were jointly fitted with a simple constant offset plus a sinusoid, which forced the fractional amplitude and phase of the normalisation variations to be the same. The fit was poor, but was significantly improved by untying the phase ($\Delta\chi^2 = 3.23$ for one additional free parameter) and amplitudes ($\Delta\chi^2 = 4.69$ for one

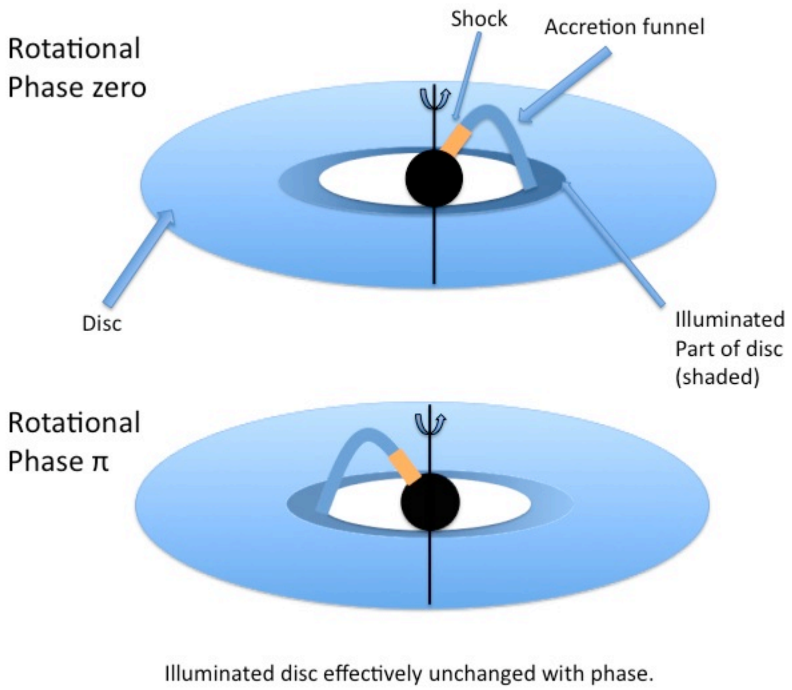

Figure 5.6: Illustration of a geometry that could give rise to a constant reflection and iron line emission with phase. The small angle between the shock and the rotation axis means that the shock does not preferentially illuminate parts of the disc with different line of sight velocities. The illuminated area of the inner disc is illustrated using darker shading.

additional free parameter). The likelihood of an observed improvement by chance was 0.003 and 3.7×10^{-6} for untying phase and then fractional amplitude respectively. The fractional amplitude of variation in the PEXRIV normalisation was close to zero i.e. consistent with a constant PEXRIV reflection component. This inconsistency in the reflection components is the most compelling evidence that the "iron line pulsation" is actually no more than a change in the underlying blackbody spectral shape with phase. The reflection and iron-line normalisation should be strongly correlated in amplitude and in phase with one another because they both emerge as a consequence of hard X-ray irradiation of the disc. In fact, Figure 5.7 demonstrates no discernible pulsation in the PEXRIV component at all.

Untying the blackbody temperature between phase-bins in this fit did not significantly improve the fit.

A second fit was performed to the phase-resolved spectra using the same model described in the phase-averaged fits, but this time constraining the reflection and line normalisations to be constant with phase. The χ^2/dof of this fit was 492.46/467. Allowing the blackbody temperature to also vary with phase (it was still assumed

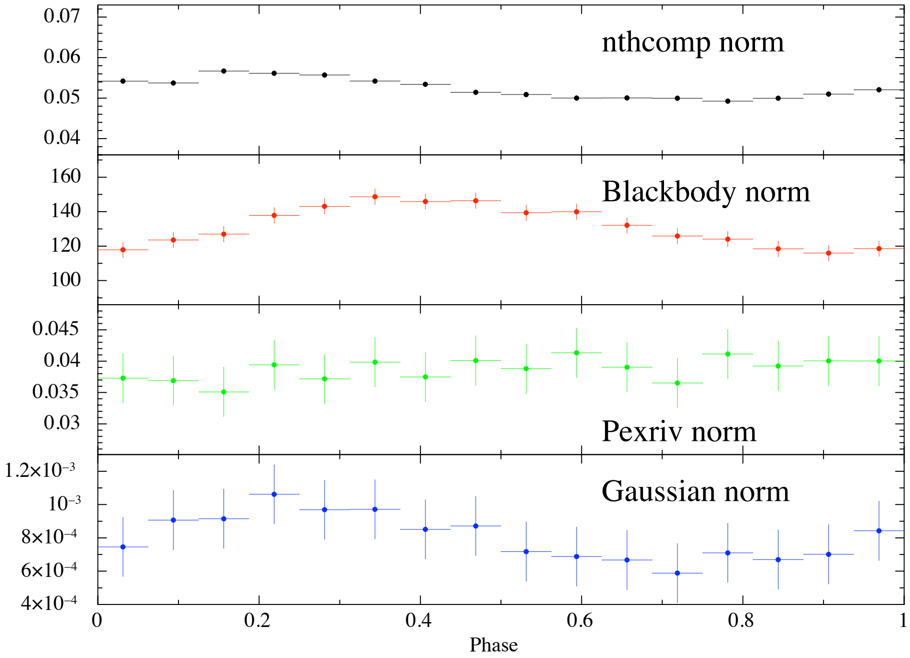

Figure 5.7: Pulsations in the normalisations of spectral components using the physical reflection model described in the phase-averaged fits. Vertical axes are plotted to roughly show the relative amplitude of pulsations and the iron-line is modelled using a Gaussian component.

that the blackbody temperature and seed photon temperature for Comptonisation were identical) improved the χ^2/dof to 464.07/451 with an f-test null hypothesis probability of 0.039. The variations with phase are shown in Figure 5.8. Again, as with the earlier phenomenological fits, the blackbody normalisation is shifted along in phase when the blackbody/seed photon temperature is a free parameter. Figure 5.9 shows 99.9% confidence contours for three phase bins (1,6 and 11) of blackbody temperature against blackbody normalisation and demonstrates that the temperature and normalisation are correlated. However, the fact that the 99.9% contours do not overlap significantly in temperature for a given normalisation (and vice versa) and there is no anti-correlation in the pulsations of these components in figure 5.8, suggests that the pulsation in these components might be real.

Untying the seed photon temperature for thermal Comptonisation and the blackbody temperature had no significant effect on the spectral fits.

There is no concrete statistical evidence to favour blackbody temperature variations over varying reflection, but there is a good physical reason to do so as outlined

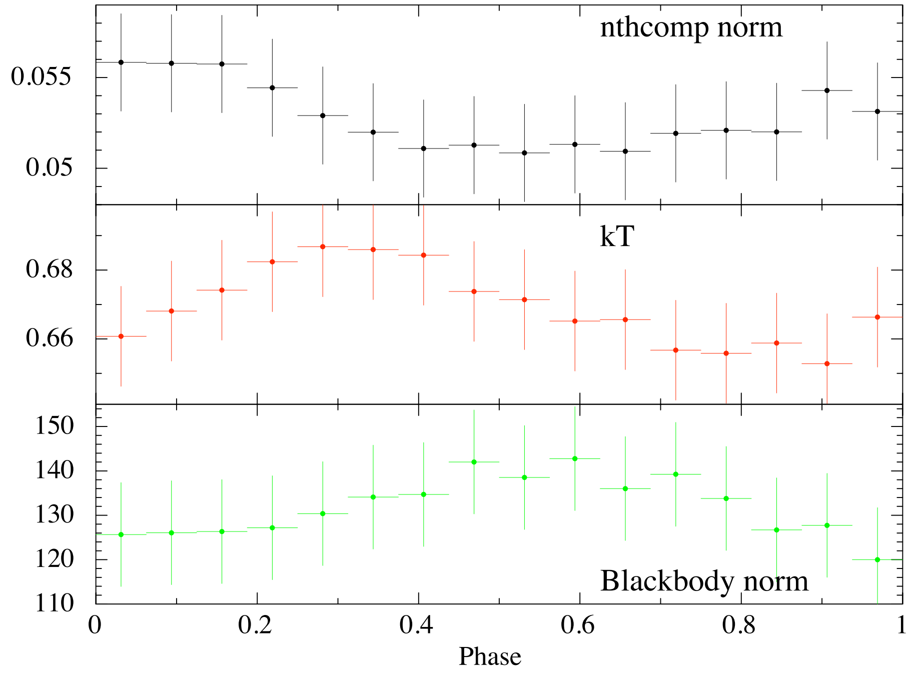

Figure 5.8: Pulsations in the BBODYRAD and NTHCOMP normalisations and the blackbody temperature with phase with all reflection parameters fixed between phase-bins.

above. The best fit arises by invoking a changing blackbody temperature with phase and, although the error bars are large, the amplitude and shape of reflection variations do not match the line variations seen in Figure 5.7. In the next section I will show that the observed variations can be explained quite simply in terms of the Doppler shifts (to produce the observed hotspot temperature variation) and solid angle changes (to produce the normalisation variation) which are expected for this system.

Table 5.2 shows the fractional rms values for the different model components of each model described above.

5.4 Discussion

The rms values shown in Table 5.2 for the physically motivated reflection model invoking blackbody temperature variations (Figure 5.8), suggest a larger variation in the blackbody component than the Comptonised component. As shown in Figure 5.10, this is most likely due to blackbody emission arising from a flatter, more hor-

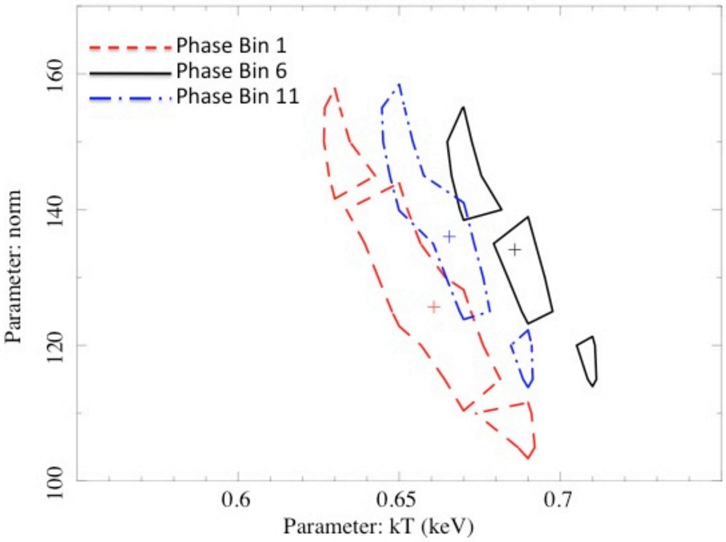

Figure 5.9: 99.9% confidence contours of blackbody normalisation versus kT corresponding to phase bins 1, 6 and 11 in figure 5.8. Due to the coarseness of the grid used to search parameter space (a step size of 0.02 keV and 5 for kT and normalisation respectively) the contours do not join up.

Table 5.2: Table of fractional rms values for different model components

	Fractional RMS			
	Fig 5.3	Fig 5.4	Fig 5.7	Fig 5.8
Diskline	0.157	n/a	n/a	n/a
Bbody norm	0.072	0.10	0.083	0.046
Power-law	0.039	0.039	n/a	n/a
kT	n/a	0.018	n/a	0.015
nthcomp norm	n/a	n/a	0.044	0.030
Pexriv norm	n/a	n/a	0.020	n/a
Gauss norm	n/a	n/a	0.155	n/a

Fractional RMS values are obtained from the best-fitting constant offset plus sinusoid model. Quoted value for the Pexriv normalisation is an upper limit.

izontally extended 'pancake' type region compared to the Comptonised emission from the accretion shock which could extend vertically from the neutron star surface. As the star rotates, the projected area of the blackbody region changes more than the accretion shock region, leading to a greater amplitude of variation. The fractional variation from the Comptonised emission might also be reduced if the accretion column is relatively optically thin (which mitigates the effect of solid angle variation), or if there exists a second, constant Comptonising region, e.g. an extended corona. The pulsation in the Comptonised component is significantly out of phase with the blackbody component, as seen in previous work (Gierliński, Done, & Barret, 2002; Ibragimov & Poutanen, 2009). However, the phase shift of $\sim$170° between these components in Figure 5.8 (when kT is a free parameter), is much larger than in previous work where the shift was $\sim$50° (Gierliński, Done, & Barret, 2002) and $\sim$70° (Ibragimov & Poutanen, 2009) with kT fixed. By fixing the blackbody temperature, the offset between the blackbody and Comptonised component is found to be $\sim$ 50°, consistent with Gierliński, Done, & Barret (2002). It would therefore appear that some of the role of changing normalisation is subsumed by the changing kT, shifting the variations in blackbody normalisation to later phases. It is perhaps surprising how sensitive the phase-shift of the blackbody component pulsations are to the choice of model used. If the accretion column is optically thick and vertically elongated above the neutron star surface (as argued above), then the solid angle of the column could be maximised when it points away from the observer. This would coincide with the minimum projected hotspot area and can therefore explain the $\sim$180° phase shift between the blackbody and Comptonised components.

For a 15 km neutron star, the Doppler shift $\Delta E/E = 2\pi R\nu/c$, produces a large shift at the equator (e.g., around 13% at a rotation frequency of 401Hz). For an accretion shock aligned at 10° to the rotation axis, the upper limit obtained by Ibragimov & Poutanen (2009), R is reduced from 15 km at the equator to just 2.6 km and the Doppler shift reduced to just 2%. If the possibility of pulsed iron line variations is discounted (as implied by the much weaker variations in the reflection continuum), the phase-resolved fits suggest that some of the pulsed variation in the spectral shape can be explained by a varying Doppler shift of the blackbody photons underlying the iron-line. If we associate the blackbody temperature change with a Doppler shift, Figure 5.8 demonstrates a peak-to-peak change in temperature of approximately 0.035 keV which in this source, assuming an inclination of 60°, translates to a radius of rotation of 3.5 km, consistent with the arguments of Poutanen & Gierliński (2003). This shift is consistent with a hot-spot aligned at

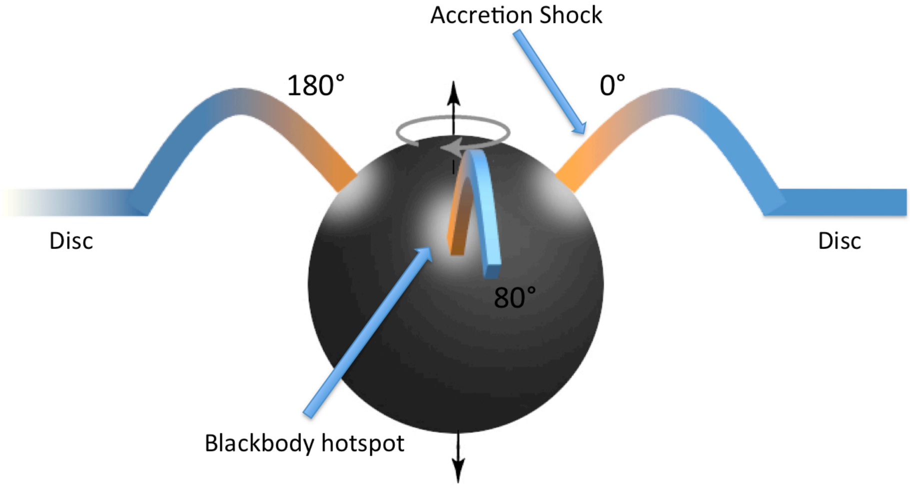

Figure 5.10: The projected area of the blackbody hotspot changes more than the projected area of the accretion shock region as the neutron star rotates. A snapshot at three different rotational phases are included on this diagram.

approximately 13.5° (20°) to the rotation axis, for a 15 km (10 km) radius neutron star. The fact that the shock makes a small angle with the rotation axis of the neutron star implies that the whole inner disc is illuminated more or less evenly i.e. there is no preferential illumination of different parts of the disc with different line of sight velocities which would lead to a change in the iron-line shape with phase.

A phase shift measured as $\sim 80^\circ$ can be seen in Figure 5.8 between the pulsation in the blackbody temperature (driven by Doppler variations) and the blackbody normalisation (driven by projected area effects). As discussed in Gierliński, Done, & Barret (2002), this is consistent with a geometry where Doppler variations are strongest when the hot-spot is at the limb of the star, and projected area effects are strongest $\sim 90^\circ$ later when the solid angle of the hot-spot is maximised. Clearly, this picture is only approximate, since effects such as light-bending are not taken account of (e.g. Ibragimov & Poutanen 2009).

The fits to these data are consistent with the idea that the iron-line shape and normalisation remain constant with phase, suggesting a geometry where the illumination of the disc by the accretion shock is fairly constant. By assuming that the *only* variable components are the normalisations of the blackbody and Comptonised components (Gierliński, Done, & Barret, 2002; Ibragimov & Poutanen, 2009), one can detect an apparent pulsation in the residual iron-line component. However, any apparent change in the iron-line normalisation with phase can be explained by taking into account the Doppler boosting of the underlying blackbody continuum. The constancy of the iron line is not really surprising, because for the small offset of the accretion column from the rotation axis that is envisaged here, the disc will not see much variation in solid angle of the accretion-shock region, and variations in Doppler beaming of the accretion-shock emission toward the disc will be small. The presence of a constant power-law continuum component from a corona would also serve to reduce the variability of the iron line emission.

5.5 Conclusions

Phase-resolved spectroscopy of the 2002 outburst of the AMXP SAX J1808.4-3658 as observed by *RXTE* reveals no convincing evidence for pulsations in the iron-line or changes of any line properties with phase. By allowing the blackbody spectral shape to change (i.e. freeing the blackbody temperature during fitting) one can allow for variable Doppler boosting of the underlying blackbody continuum, which introduces a larger phase-shift between the Comptonised component normalisation and the blackbody normalisation than has been seen in previous work. The phase-shift between the blackbody normalisation and the blackbody temperature is approximately consistent with the expected 90° offset between the maximum projected area and maximum Doppler shifts. The fraction of the disc illuminated by the Comptonising region appears to be roughly constant with rotational phase.

I think and think for months and years. Ninety-nine times, the conclusion is false. The hundredth time I am right.

ALBERT EINSTEIN (1879 - 1955)

6

Conclusions

In this final chapter I shall discuss some of the conclusions that can be gleaned from this work, and discuss the potential for future work informed by both my own results and those of my colleagues.

6.1 A picture of BHXRB c.2007

I shall start by giving a brief, but by no means exhaustive, overview of relevant information known about BHXRB at the time when I started my PhD in 2007.

As discussed in the introduction to this thesis, it was commonly accepted that the different spectral states of BHXRB were described by an accretion flow with contributions to the emission from optically thick and optically thin material. The 'truncated-disc' model had been proposed and appeared to explain the correlation between the amplitude of reflected emission and the slope of the Comptonised power-law, as well as the correlation between the reflection scaling factor and the degree of relativistic smearing (Gilfanov, Churazov, & Revnivtsev, 2004). The truncated-disc model provided a geometric argument explaining the spectral state transitions in Black Hole X-ray Binaries (BHXRBs) and was invoked to explain the changing characteristic frequencies in the variability power-spectra of these sources.

However, evidence was emerging of smeared iron lines and reflection features consistent with un-truncated discs in some (quite bright) hard-state observations (Miniutti, Fabian, & Miller, 2004; Miller et al., 2006). There were also soft excesses seen in some BHXRB with only moderate galactic absorption, consistent with a disc extending close to the black hole in the hard-state (Miller, Homan, & Miniutti, 2006; Rykoff et al., 2007). This was a clear conflict which hinted, at the very least, that the disc didn't necessarily truncate when a BHXRB transitioned to the hard-state. There were no ionised reflection models appropriate for BHXRB discs (at the time of writing there are still no publicly available models of this type), since all had been calculated assuming AGN conditions where the disc emission lies in the UV. It was clear that better reflection models were required, but more generally spectral fitting alone was simply too unreliable due to the difficulty in interpreting fits that incorporated often simplified and idealised model components.

Although a great deal of phenomenology had been developed, in truth not a great deal was known about the physical interpretation of the variability power-spectra of these sources. The propagating fluctuation model of Lyubarskii (1997) was able to successfully explain the ν^{-1} flicker-noise shape of the power-spectrum at low-frequencies, the rms-flux relation (Uttley & McHardy, 2001) and the energy/time dependence of the lags (Kotov, Churazov, & Gilfanov, 2001). The origin of the shape of the band-limited noise in the power-spectrum was less well understood. Attempts had been made to fit Lorentzian components to the band-limited noise and identify the characteristic frequencies of these components with characteristic timescales of the disc. There was however, no consensus as to the origin of these features. One suggestion (Done et al., 2007) was that, in the context of the truncated disc model, fluctuations at certain frequencies were generated at the truncation radius (possibly by turbulence at the disc/hot inner flow interface), and propagated through the hot-flow which acted as a low-pass filter damping fluctuations faster than the viscous timescale at the inner radius of the hot-flow. As the disc inner radius moved inwards, the frequencies generated at the truncation radius would increase, but the filtering effect of the hot-flow kept the high-frequency power-spectrum quite constant.

One final point worth reiterating, alluded to in section 1.7 of the introduction, is that very few observations of hard-state BHXRB had been made with good soft X-ray coverage when I began my PhD. Studies searching for variability in the thin disc concentrated on soft states (e.g. Cygnus X-1 in Churazov et al. (2001)) where the disc was dominant in the mean spectrum. These studies found that the disc was remarkably stable, and reasoned this was so because fluctuations in the disc were damped due to its much longer viscous timescale. The power-law component, however, was seen to vary strongly. The established fact that the variability was much stronger in the hard state, coupled with the facts that the power-law component dominated the radiative output and that the disc was seen to be very stable in the soft-state, lead people to conclude that variability was associated only with the hot-flow. Unveiling this misconception about disc stability is one of the key contributions of this thesis.

6.2 Impact of this work

The reader is referred back to the concluding sections of each chapter for a detailed summary of my work; here I present only a brief overview highlighting the key science results. Given that chapter 5 is a stand-alone piece of work and not related to the topic of disc variability, I shall not include this in my general discussion here.

My work exploiting the soft X-ray coverage of *XMM-Newton* has provided the first evidence in the hard-state of BHXRBs for enhanced intrinsic disc-variability on time-scales of seconds or longer. Furthermore, a comparison of the normalisation of black-body and iron-line components in the variability spectrum implies that the short time-scale variability is driven by thermal reprocessing of power-law continuum absorbed by the disc. This is supported by the fact (Uttley et al., 2011) that the soft photons lag harder photons with delays of $\sim$1 msec on time-scales $\sim$0.1 sec, consistent with the light crossing time for a few tens of Rg. The fact that X-ray reverberation of the disc dominates the lags on the shortest time-scales means that this kind of analysis is potentially very useful to map the disc in LMXBs. On longer timescales, where we see extra intrinsic disc variability in BHXRB, the lags display the opposite behaviour to that described above. There is a sharp increase in the hard-soft time-lag which arises at energies where the disc begins to dominate the X-ray spectrum (figure 2.9). This suggests that it is the disc that drives the variability in the hard-state, because accretion rate fluctuations in the disc are subsequently propagated in to the inner hot flow. It had previously been assumed that all the variability in BHXRB was generated in the hot-flow, but the soft coverage of *XMM-Newton* has revealed the intrinsically variable disc in the hard-state and that it is the disc that drives the variability. If the geometry was such that the corona could see the disc variability directly (e.g. if the corona sandwiched the disc) lags of this type would be washed out due to up-scattering by seed photons. This implies that the corona is compact and central. Further evidence for a compact central corona comes from the fact that the intrinsic disc variability on seconds timescales is larger than the power-law variability on those timescales. If the corona could see the disc modulations directly, then the seed photon flux would modulate the power-law emission with a similar amplitude to that of the disc. The most elegant explanation which fits in with established propagation models for the reduced power-law variability on these timescales, calls upon the damping of mass accretion rate variations in the disc as the variations propagate inwards to the inner-flow. The relative contribution of intrinsic variability to reverberation variability as a function of frequency is currently unclear, but proposed future studies of Cygnus X-1 will elucidate this issue.

Having established that the Lorentzian component in the hard-state PSD was a disc signature, I could not find any strong model independent evidence to suggest that this feature could be associated with the movement of the inner edge of the disc. However, extending my analysis of disc variability to higher frequencies and other source states revealed remarkable evidence that disc variability *could* drive such QPOs. One possible picture is that the frequency of a given QPO corresponds to the radius where a region of turbulence occurs in the disc. A frequency increase corresponds to a decrease of this turbulent radius, $R_{\rm QPO}$, such that at frequencies >5 Hz (close to the maximum fundamental frequencies observed for the QPO) the turbulent region is already close to the ISCO and the amount of disc emission inside this radius is small. The disc blackbody variability seen at the QPO frequency is therefore very small since only a small fraction of the disc luminosity can be modulated. In this model the power-law component is primarily generated inside $R_{\rm QPO}$, hence the power-law variability reflects more closely the intrinsic amplitude of $\dot{M}$ fluctuations, since most of the power-law flux can be modulated by the QPO variations in $\dot{M}$. During the evolution of an outburst the type-B QPO frequency peaks at ~6 Hz, and this could represent the fact that the region of disc turbulence generating the QPO cannot move any further than the ISCO.

Given the limitations of current reflection models, not much can be said with certainty about the radius of truncation in the hard-state from this work. There is nothing that definitely excludes the possibility that the disc can remain at the ISCO in the hard-state, and the disc reverberation lags (Uttley et al., 2011) place an upper limit on the truncation radius in terms of tens, rather than hundreds, of gravitational radii. I have demonstrated in Chapter 3 that spectral fitting involving reflection components can be extremely degenerate. The inner radius and emissivity profiles are very degenerate parameters in all such model fits, so it is absolutely essential to corroborate any interpretations made from spectral fitting with model independent analysis. It is also important that a reflection model is made publicly available that properly models the reflection from an accretion disc of a BHXRB, instead of assuming AGN conditions. No such strong model independent evidence could be found in chapter 3 that the change in frequency of the low-frequency Lorentzian component could be associated with changes in the location of the inner edge of the disc. This was despite compelling evidence from spectral fitting alone when assumptions are made about the emissivity profile of the reflection and the ionisation state of the disc. The lesson to be learned is that if the interpretation of the data is correct then a consistent picture will emerge from a range of different analysis techniques.

Novel spectral-timing techniques have been used to probe the rapid variability of X-ray binaries throughout this thesis. A summary of my main findings are listed below.

- I have utilised a new technique, the covariance spectrum, to measure the correlated variability in different energy bands. This technique overcomes low signal-to-noise and has lower statistical errors. It has enabled me to disentangle correlated contributions from distinct spectral components.

- I have identified additional disc variability on seconds timescales by looking at variable spectra on different timescales.

- Covariance ratios provide model independent evidence of this additional blackbody variability on longer timescales.

- I have shown that the PSD demonstrates larger low-frequency power in the soft band, consistent with the interpretation of enhanced disc variability on longer timescales.

- I have discussed recent work undertaken by Phil Uttley which has demonstrated a causal connection between the disc and power-law by exploiting cross-spectral time-lags.

- I have demonstrated using cross-spectral time-lags that, over QPO frequencies, the disc variations lead power-law variations implying that the disc might drive the QPO. Here, the extra information provided by the time-lags actually informs the spectral fits, leading to the addition of spectral components that cannot be statistically justified using spectral-fitting alone.

- Variability spectra have shown that disc variability is greatly reduced over QPO frequencies, suggesting that at these frequencies the QPO is generated by disc variations near the disc inner edge.

- I have used the technique of phase-resolved spectroscopy to place constraints on the accretion geometry of the AMXP SAX J1808.4-3658. Our results are consistent with there being no preferential illumination of different parts of the disc with different line of sight velocities.

6.3 Future Work

My colleagues and I would like to extend this work to explore the disc variability and lag behaviour of neutron-star binaries. No similar studies exploring the disc variability in neutron-star binaries have been performed. The accretion of material on to a neutron-star is similar to that of a black hole, with the obvious exception that material accreting on to a neutron star has to impact on to its solid surface releasing kinetic energy in a boundary layer. This boundary layer creates some spectral differences, but, particularly at low accretion rates, the X-ray variability properties of neutron-star and black hole systems are extremely similar. It is thought that at low mass-accretion rates, the disc is truncated in a similar manner, with seed photons from the surface of the neutron-star being partially Comptonised in the boundary layer and illuminating the hot inner flow. We would expect to see similar disc variability behaviour in neutron-stars, which would further confirm the link between the accretion flows of neutron-star and black-hole binaries.

One ideal candidate to study such behaviour would be the persistent low-magnetic field neutron star Low-Mass X-ray Binary (LMXB) 4U 1636-536. This source, like all atoll sources, displays two distinct states, the island and banana states, analogous to the hard and thermal dominated states of BHXRBs. 4U 1636-536 has low galactic absorption ($< 0.4 \times 10^{22}$ cm^{-2}) and its light-curves have so far shown no evidence for any intrinsic absorption or eclipses. 4U 1636-536 has undergone regular transitions between the island and banana states for over 5 years on a typical timescale of 20-30 days (Belloni et al., 2007) with a hardness-intensity diagram (HID) that follows a hysteresis cycle similar to that of BHXRBs. Relativistically broadened iron-line emission has also been seen in this source (Pandel, Kaaret, & Corbel, 2008) suggestive of reflection from the inner-accretion disc. If the disc is being irradiated by the Comptonizing region (corona or boundary layer), one would expect some fraction of this incident continuum to be absorbed leading to thermal reprocessing, which has already been shown to dominate the lags in BHXRBs on the shortest time-scales. The fact that 4U 1636-536 has transitioned so regularly between these two states for so long, makes it an ideal candidate to explore the intrinsic variability of the disc. Given that a soft excess has been detected in many BHXRB hard-states with black-hole masses far greater than neutron-star masses, we would expect to see the contribution from the thin disc in X-rays. Neutron-star binary X-ray spectra are more complex than their black-hole counterparts due to the extra boundary layer emission. Disentangling the soft emission components is difficult, therefore the only way to understand the role of each component is to separate their relative contributions through variability analysis on different timescales (Shrader, Kazanas, & Reig, 2007).

Key objectives of this work would be to:

- Use the covariance, rms and mean spectra to disentangle the relative contributions of intrinsic and thermally reprocessed disc emission and disentangle the neutron-star surface emission from the lower energy multicolour disc blackbody emission.

- Use the technique of Fourier-resolved spectroscopy to determine whether there is enhanced disc variability on certain timescales, and relate these to features (e.g. Lorentzian components) in the power spectrum (PSD) of this source.

- Examine the energy spectra at different mass accretion rates to detect changes in the broadening of the iron-line, and link this to changes in the truncation radius of the disc.

- Explore whether or not the disc variability stabilises in the banana state of atoll sources, in an analogous manner to the soft-state of BHXRBs.

- For the first time explore the lag vs energy spectra of this source to see if the disc blackbody component leads the power-law as it does in BHXRB. The lag vs. energy spectra may be distinct from those seen in BHXRBs due to the presence of the thermal emission from the neutron star surface. If this is powered by accretion, this blackbody component will lag the disc blackbody by a time equal to the viscous infall time from the disc emitting regions to the neutron star surface: a unique probe of accretion. Furthermore, we can use the lags to establish the causal relationship between the surface blackbody and the power-law emission. If the power-law is a hot flow, it will lead the surface blackbody emission by the radial infall time, which could be tens of ms. If the power-law is associated with the boundary layer itself there will be only a very small (light-crossing time) lag between these components.

The hard-state of BHXRBs provides the ideal laboratory to simultaneously study the accretion disc, the inner-flow and the jet. A clear correlation exists between the accretion power dissipated in the disc and that which is injected into the jet as shown originally by Gallo, Fender, & Pooley (2003). Given that the unstable disc has been shown to drive the hard power-law component in the hard-state, and that the jet is linked to the hard-state, an investigation should be made in to the relationship between disc stability and the jet; perhaps a variable disc is a prerequisite for jet emission which is why it is only seen in the hard-state. The optical and Near Infra-Red (NIR) variability observed in BHXRB is thought to arise due to variable jet synchrotron emission, therefore simultaneous fast optical and X-ray (with good soft coverage such as XMM-Newton or SWIFT) timing studies could search for correlations between the disc and the optical variability. Particularly interesting would be identifying the region in the HID where the jet switches on/off, and seeing if this corresponds to the disc variability arising/quenching.

Another area to focus on in the future would be the development of physically motivated models to fit lag-spectra. Lag spectra establish the causal relationship between correlated variations in different emission components, so successful model fits would demonstrate a significant step forward in our understanding of BHXRBs. More generally, the ultimate goal of exponents of X-ray timing should be to produce physically motivated models that can simultaneously fit mean spectra, variability spectra and lag spectra. In this way we will be using *all* of the available timing information to present a physically consistent and more compelling picture of X-Ray Binaries.

APPENDICES

Research is what I'm doing when I don't know what I'm doing.

JOE BLOGS (1890-1949)

A

Plotting X-ray Spectra

X-ray spectra are usually presented as photons received per unit time, per unit detector area, per unit energy interval, P_E(E), in units of photons/cm^2/s/keV.

As discussed in the introduction, such spectra are generated by Compton up-scattering and are well represented as a power-law:

$$P_E \propto E^{-\Gamma} \tag{A.1}$$

or in terms of energy flux:

$$F_E = E \times P_E \propto E^{-\Gamma+1} \tag{A.2}$$

This power-law dependence applies over a wide range of energies, therefore logarithmic energy intervals are used:

$$P_E dE = P_E E dE/E = E P_E dlogE = F_E dlogE \tag{A.3}$$

So, counter intuitively, plotting the log of flux against the log of energy shows the number of photons per energy bin. In a similar manner, extending the arguments above, plotting log EF_E against log E shows the energy at which the source luminosity peaks.

Since $EF_E \propto E^{-\Gamma+2}$, a soft spectrum, which peaks at low energies, has a Γ of > 2 and a hard spectrum, which peaks at higher energies, has a Γ of < 2.

Come on... Come on! Do it! Do it! Come on. Come on!
Kill me! I'm here! Kill me! I'm here! Kill me! Come on!
Kill me! I'm here! Come on! Do it now! Kill me!

DUTCH (1987-?)

B

The error on the excess variance

The excess variance, $\sigma^2_{xs,j}$, of the j$^{\mathrm{th}}$ lightcurve, which represents one particular realisation of a process, consisting of counts in bins $\mathrm{x_i}$ to $\mathrm{x_N}$ can be written:

$$\sigma^2_{xs,j} = S^2_j - <\sigma^2_{err,j}> \tag{B.1}$$

where S is the sample variance from a single observed light curve and σ^2_{err} represents the expected contribution from measurement errors. Angle brackets denote averages over the length of one observation (realisation). Typically, one attempts to estimate measurement errors experimentally, either from error bars or by assuming a certain error distribution (e.g. Poisson noise). In this sense, a distinction needs to be made between the underlying measurement errors and the observed estimate of these errors obtained from looking at an individual light curve. Slight deviations will exist in this error estimate from realisation to realisation, and the average expected error can be represented in the following way for a lightcurve, j:

$$<\sigma^2_{err,j}> = <\Delta x^2_i + \Delta\sigma^2_{err,i}> \tag{B.2}$$

where Δx^2_i is the underlying true variance of the counts in each bin (i=1 to N) for that realisation, and $\Delta\sigma^2_{err,i}$ represents the deviations (sometimes positive, sometimes negative) around this value. Over a very large number of realisations the expectation value of equation B.2 would approach the underlying true value $\overline{\sigma_{err}^2} = \overline{\Delta x_i^2}$, since the expectation value of the deviations, $\Delta\sigma_{err,i}^2$, becomes zero.

Equation B.1 can be expanded as:

$$< \sigma_{xs}^2 >= \frac{1}{N}\sum_{i=1}^{N}(x_i+\Delta x_i)^2 - (\frac{1}{N}\sum_{i=1}^{N}(x_i+\Delta x_i))^2 - \frac{1}{N}\sum_{i=1}^{N}\left(\Delta x_i^2+\Delta\sigma_{err,i}^2\right) \tag{B.3}$$

where $\mathrm{x_i}$ is the count rate in the $\mathrm{i^{th}}$ bin. Before deriving the error on the excess variance from first principles, it is important to note that the notation $< ... >$ throughout this derivation represents expectations taken over ONE light curve. This is different to expectations evaluated over many (infinite) light curves, for which the notation E[...] is used throughout. It should also be noted that I use a 1/N normalisation when calculating variances, as in the limit of large N the N/N-1 bias in the variance estimate makes a negligible difference (i.e. we assume that light curves are long enough for this difference to be negligible). Using this notation, equation B.3 can be re-written simply as:

$$\begin{aligned} < \sigma_{xs}^2 > \;=\; & < x_i^2 > + < 2x_i\Delta x_i > + < \Delta x_i^2 > - \\ & \left(\frac{1}{N^2}\sum_{i=1}^{N}(x_i+\Delta x_i)\sum_{k=1}^{N}(x_k+\Delta x_k)\right) - \frac{1}{N}\sum_{i=1}^{N}\left(\Delta x_i^2+\Delta\sigma_{err,i}^2\right) \end{aligned} \tag{B.4}$$

$$\begin{aligned} < \sigma_{xs}^2 > \;=\; & < x_i^2 > + < 2x_i\Delta x_i > + < \Delta x_i^2 > - \\ & \frac{1}{N^2}\left(\sum_{i=1}^{N}x_i\sum_{k=1}^{N}x_k + 2\sum_{i=1}^{N}x_i\sum_{k=1}^{N}\Delta x_k + \sum_{i=1}^{N}\Delta x_i\sum_{k=1}^{N}\Delta x_k\right) - \\ & \frac{1}{N}\sum_{i=1}^{N}\left(\Delta x_i^2+\Delta\sigma_{err,i}^2\right) \end{aligned} \tag{B.5}$$

$$\begin{aligned} < \sigma_{xs}^2 > \;=\; & < x_i^2 > + < 2x_i\Delta x_i > + < \Delta x_i^2 > - < x_i >^2 - < \Delta x_i >^2 - \\ & < \Delta x_i^2 > - < \Delta\sigma_{err,i}^2 > -2 < x_i >< \Delta x_i > \end{aligned} \tag{B.6}$$

Canceling the $< \Delta x_i^2 >$ terms leaves:

$$\begin{aligned} < \sigma_{xs}^2 > \quad = \quad & < x_i^2 > + < 2x_i\Delta x_i > - < x_i >^2 -2 < x_i >< \Delta x_i > - \\ & < \Delta x_i >^2 - < \Delta\sigma_{err,i}^2 > \end{aligned} \tag{B.7}$$

We need to determine the error in the excess variance, σ_{xs}^2, which is computed from its variance:

$$\mathrm{VAR}\left[\sigma_{\mathrm{xs}}^2\right] = \mathrm{E}\left[(\sigma_{\mathrm{xs}}^2)^2\right] - \left[\mathrm{E}(\sigma_{\mathrm{xs}}^2)\right]^2 \tag{B.8}$$

where, to reiterate for the sake of clarity, the notation E refers to the expectation over many (i.e. an infinite number) of light curves. This means we have to work out the following quantities, $< \sigma_{xs}^2 >$, $(< \sigma_{xs}^2 >)^2$ and the expectation values $E\left[(< \sigma_{xs}^2 >)^2\right]$ and $E[< \sigma_{xs}^2 >]$. Great care should be taken with the notation since, for example, $E[x^2]$ might be very different from $(E[x])^2$.

Performing the algebra, the expression for $(< \sigma_{xs}^2 >)^2$ is:

$$\begin{aligned} < \sigma_{xs}^2 >^2 \quad = \quad & < x_i^2 >^2 + < x_i^2 >< 2x_i\Delta x_i > - < x_i^2 >< x_i >^2 -2 < x_i^2 >< \Delta\sigma_{err,i}^2 > - \\ & 2 < x_i^2 >< x_i >< \Delta x_i > - < x_i^2 >< \Delta x_i >^2 + < 2x_i\Delta x_i >< x_i^2 > + \\ & < 2x_i\Delta x_i >^2 - < 2x_i\Delta x_i >< x_i >^2 - < 2x_i\Delta x_i > 2 < x_i >< \Delta x_i > - \\ & < 2x_i\Delta x_i >< \Delta x_i >^2 - < x_i >^2< x_i^2 > - < x_i >^2< 2x_i\Delta x_i > + < x_i >^4 + \\ & < x_i >^2 2 < x_i >< \Delta x_i > + < x_i >^2< \Delta x_i >^2 -2 < x_i >< \Delta x_i >< x_i^2 > - \\ & 2 < x_i >< \Delta x_i >< 2x_i\Delta x_i > + < x_i > 2 < \Delta x_i >< x_i >^2 + < \Delta\sigma_{err,i}^2 >^2 + \\ & 2 < x_i >< \Delta x_i >< \Delta x_i >^2 - < \Delta x_i >^2< x_i^2 > - < \Delta x_i >^2< 2x_i\Delta x_i > + \\ & < \Delta x_i >^2< x_i >^2 + < \Delta x_i >^2 2 < x_i >< \Delta x_i > + < \Delta x_i >^4 - \\ & 2 < 2x_i\Delta x_i >< \Delta\sigma_{err,i}^2 > +2 < x_i >^2< \Delta\sigma_{err,i}^2 > +4 < x_i >^2< \Delta x_i >^2 + \\ & 2 < \Delta x_i >^2< \Delta\sigma_{err,i}^2 > +4 < x_i >< \Delta x_i >< \Delta\sigma_{err,i}^2 > \end{aligned} \tag{B.9}$$

Any term containing Δx_i to an odd power will go to zero when the expectation value is taken over many light curves, since there are as many positive as negative contributions. This means many terms in equation B.9 go to zero and can be disregarded. This is also true of terms containing $<\Delta\sigma^2_{err,i}>$ since these values will also be distributed about zero (but not terms containing $<\Delta\sigma^2_{err,i}>^2$ which are non-zero over many realisations).

Taking expectations over many light curves of equation B.7 gives:

$$E[<\sigma^2_{xs}>] = E[<x_i^2>] - \mu^2 - E[<\Delta x_i>^2] \tag{B.10}$$

where μ is the mean count rate. Squaring this equation gives:

$$\begin{aligned}(E[<\sigma^2_{xs}>])^2 &= (E[<x_i^2>])^2 - 2\mu^2 E[<x_i^2>] - 2E[<\Delta x_i>^2]E[<x_i^2>] + \\ &\quad \mu^4 + 2\mu^2 E[<\Delta x_i>^2] + (E[<\Delta x_i>^2])^2\end{aligned} \tag{B.11}$$

Below I use the subscript j to indicate that we are multiplying different sums together before expectation values are taken. Taking expectations of equation B.9 (ignoring terms that obviously go to zero as discussed above):

$$\begin{aligned}E[<\sigma^2_{xs}>^2] &= E[<x_i^2>^2] - 2\mu^2 E[<x_i^2>] - 2E[<x_i^2><\Delta x_j>^2] + \\ &\quad 2\mu^2 E[<\Delta x_i>^2] + \mu^4 + E[<\Delta x_i>^4] + E[<2x_i\Delta x_i>^2] - \\ &\quad 2\mu E[<2x_i\Delta x_i><\Delta x_j>] - 2\mu E[<\Delta x_j><2x_i\Delta x_i>] + \\ &\quad 4\mu^2 E[<\Delta x_i>^2] + E[<\Delta\sigma^2_{err,i}>^2]\end{aligned} \tag{B.12}$$

Inserting these results in to equation B.8 leaves the following remaining terms:

$$\begin{aligned}E\left[(\sigma^2_{xs})^2\right] - \left[E(\sigma^2_{xs})\right]^2 &= E[<\Delta x_i>^4] + E[<2x_i\Delta x_i>^2] - \\ &\quad 4\mu E[<\Delta x_j><2x_i\Delta x_i>] + 4\mu^2 E[<\Delta x_i>^2] - \\ &\quad (E[<\Delta x_i>^2])^2 + E[<\Delta\sigma^2_{err}>^2]\end{aligned} \tag{B.13}$$

$$E[<\Delta x_i>^4] = (E[<\Delta x_i>^2])^2 = \left(\frac{\overline{\sigma^2_{err}}}{N}\right)^2 \tag{B.14}$$

so these two terms in equation B.13 cancel. An important distinction in notation between Δx and δx is now made. The term δx_i refers to intrinsic source variability, where as Δx_i represents uncertainty due to measurement error (e.g. Poisson noise for example). One can then understand the equality $x_i = \mu + \delta x_i$ to be attributing a mean component and an intrinsically variable component to the count rate in a given bin. It is important to note that throughout this derivation δx_i is the same for every realisation. Only the photon statistics change from realisation to realisation, where as the intrinsic variability of the light curve is always assumed to be the same. This enables us, when taking expectation values, to treat δx_i as a constant term, analogous to the treatment of μ in the equations that follow below.

Solving the remaining terms in equation B.13 by taking expectations over many (infinite) realisations (remembering that over many realisations only j=i terms are always positive and do not cancel) gives:

$$\begin{aligned} E[< 2x_i\Delta x_i >^2] &= E\left(\frac{1}{N^2}\sum_{i=1}^{N} 2x_i\Delta x_i \sum_{j=1}^{N} 2x_j\Delta x_j\right) = \\ & E\left(\frac{1}{N} < 4(\mu+\delta x_i)^2\Delta x_i^2 >\right) = \\ & \frac{4\mu^2\overline{\sigma^2_{err}}}{N} + \frac{4\overline{\sigma^2_{rms}\sigma^2_{err}}}{N} + \frac{8\mu\overline{\delta x_i}\overline{\sigma^2_{err}}}{N} \end{aligned} \tag{B.15}$$

$$\begin{aligned} 4\mu E[< \Delta x_j >< 2x_i\Delta x_i >] &= 4\mu E\left(\frac{1}{N^2}\sum_{j=1}^{N} \Delta x_i \sum_{k=1}^{N} 2x_k\Delta x_k\right) = \\ & E\left(\frac{4\mu < 2\mu\Delta x_i^2 >}{N} + \frac{4\mu < 2\delta x_i\Delta x_i^2 >}{N}\right) = \\ & \frac{8\mu^2\overline{\sigma^2_{err}}}{N} + \frac{8\mu\overline{\delta x_i}\overline{\sigma^2_{err}}}{N} \end{aligned} \tag{B.16}$$

$$4\mu^2 E[< \Delta x_i >^2] = E\left(4\mu^2\frac{1}{N^2}\sum_{i=1}^{N}\Delta x_i^2\right) = \frac{4\mu^2\overline{\sigma^2_{err}}}{N} \tag{B.17}$$

As discussed in the introduction, the variance is obtained by integrating the power over frequency. The distribution of the powers is a chi-square distribution with two degrees of freedom, so the error on the power is equal to the expected value. The error on the noise power in any given bin is therefore simply equal to the noise power in that bin:

$$err(\Delta\nu P_N) = P_N \Delta\nu \tag{B.18}$$

Given that there are N/2 frequency bins, the expected variance due to measurement noise, $\overline{\sigma^2_{err}}$, can be expressed as:

$$\overline{\sigma^2_{err}} = P_N \Delta\nu \frac{N}{2} \tag{B.19}$$

therefore:

$$err(\Delta\nu P_N) = P_N \Delta\nu = \frac{2\overline{\sigma^2_{err}}}{N} \tag{B.20}$$

Adding these errors in quadrature over all frequency bins, gives the variance of the expected measurement errors:

$$E[(\Delta\sigma^2_{err})^2] = err(\sum_{i=1}^{N/2} \Delta\nu P_N) = \sqrt{\frac{N}{2}\left(\frac{2\overline{\sigma^2_{err}}}{N}\right)^2} = \frac{2(\overline{\sigma^2_{err}})^2}{N} \tag{B.21}$$

This analysis enables us to compute the last expectation value:

$$E[< \Delta\sigma^2_{err} >^2] = \frac{2(\overline{\sigma^2_{err}})^2}{N} \tag{B.22}$$

Going back to equation B.13 and inserting terms:

$$\begin{aligned} E\left[(\sigma^2_{xs})^2\right] - \left[E(\sigma^2_{xs})\right]^2 &= \frac{4\mu^2\overline{\sigma^2_{err}}}{N} + \frac{4\overline{\sigma^2_{err}\sigma^2_{rms}}}{N} - \frac{8\mu^2\overline{\sigma^2_{err}}}{N} + \frac{4\mu^2\overline{\sigma^2_{err}}}{N} + \frac{2(\overline{\sigma^2_{err}})^2}{N} = \\ & \frac{4\overline{\sigma^2_{err}\sigma^2_{rms}}}{N} + \frac{2(\overline{\sigma^2_{err}})^2}{N} \end{aligned} \tag{B.23}$$

So, finally:

$$\mathrm{VAR}\left[\sigma^2_{\mathrm{xs}}\right] = \frac{4\overline{\sigma^2_{\mathrm{err}}\sigma^2_{\mathrm{rms}}}}{\mathrm{N}} + \frac{2(\overline{\sigma^2_{\mathrm{err}}})^2}{\mathrm{N}} \tag{B.24}$$

Which can be compared with equation 11 of Vaughan et al. (2003) (which is the expression for the error on the *normalised* excess variance so includes a factor $1/\bar{x}^2$ and expressions in terms of $\mathrm{F_{var}}$ (rather than σ_{rms}).

It is possible to follow similar arguments to derive the errors on the covariance spectrum, but this is not included here due to time constraints.

BIBLIOGRAPHY

Arévalo P., Uttley P., 2006, MNRAS, 367, 801

Arévalo, P., Uttley, P., Kaspi, S., Breedt, E., Lira, P., M^{c}Hardy, I. M., 2008, MNRAS, 389, 1479

Arnaud, K. A. 1996, Astronomical Data Analysis Software and Systems V, 101, 17

Axelsson, M., Hjalmarsdotter, L., Borgonovo, L., Larsson, S., 2008, A&A, 490, 253

Ballantyne D. R., Iwasawa K., Fabian A. C., 2001, MNRAS, 323, 506

Bartlett, M.S., 1955, An Introduction to Stochastic Processes, CUP, Cambridge

Bartlett, M.S., 1948, Nature 161, 686-687

Belloni T., Homan J., Motta S., Ratti E., Méndez M., 2007, MNRAS, 379, 247

Belloni T. M., States and transitions in black-hole binaries, arXiv:0909.2474v1

Bhattacharya D., van den Heuvel E. P. J., 1991, PhR, 203, 1

Bildsten L., Chakrabarty D., 2001, ApJ, 557, 292

Box, G.E.P., Jenkins, G.M., 1976, Time Series Analysis: Forecasting and Control, 2nd edn. Holden-Day, San Francisco

Breedt E., et al., 2009, MNRAS, 394, 427

Cackett E. M., et al., 2010, ApJ, 720, 205

Cackett E. M., Altamirano D., Patruno A., Miller J. M., Reynolds M., Linares M., Wijnands R., 2009, ApJ, 694, L21

Casella P., Belloni T., Stella L., 2005, ApJ, 629, 403

Chakrabarty D., Morgan E. H., 1998, Natur, 394, 346

Churazov, E., Gilfanov, M., & Revnivtsev, M., 2001, MNRAS, 321, 759

Coriat M., Corbel S., Buxton M. M., Bailyn C. D., Tomsick J. A., Körding E., Kalemci E., 2009, MNRAS, 400, 123

D'Angelo C., Giannios D., Dullemond C., Spruit H., 2008, A&A, 488, 441

Done C., Mulchaey J. S., Mushotzky R. F., Arnaud K. A., 1992, ApJ, 395, 275

Done C., Gierliński M., 2006, MNRAS, 367, 659

Done, C., Gierliński, M., & Kubota, A., 2007, A&ARv, 15, 1

Done C., Diaz Trigo M., 2009, arXiv, arXiv:0911.3243

Done, C., arxiv:1008.2287v1

Dovčiak M., Karas V., Yaqoob T., 2004, ApJS, 153, 205

Eardley D. M., Lightman A. P., Shapiro S. L., 1975, ApJ, 199, L153

Esin A. A., McClintock J. E., Narayan R., 1997, ApJ, 489, 865

Fabian A. C., Rees M. J., Stella L., White N. E., 1989, MNRAS, 238, 729

Fender R. P., Homan J., Belloni T. M., 2009, MNRAS, 396, 1370

Frank J., King A., Raine D., Accretion Power in Astrophysics, Cambridge University Press, Third edition

Gallo E., Fender R. P., Pooley G. G., 2003, MNRAS, 344, 60

Galloway D. K., Cumming A., 2006, ApJ, 652, 559

Gandhi P., et al., 2010, arXiv, arXiv:1005.4685

Gierliński M., Zdziarski A. A., Poutanen J., Coppi P. S., Ebisawa K., Johnson W. N., 1999, MNRAS, 309, 496

Gierliński M., Done C., Barret D., 2002, MNRAS, 331, 141

Gierliński, M., Done, C., Page, K., 2008, MNRAS, 388, 753

Gilfanov, M., Churazov, E., & Revnivtsev, M., 1999, A&A, 352, 182

Gilfanov M., Churazov E., Revnivtsev M., 2004, AIPC, 714, 97

Gilfanov M., X-ray emission from black-hole binaries, arxiv :0909.2567v1

Haardt F., Maraschi L., 1991, ApJ, 380, L51

Hartman J. M., et al., 2008, ApJ, 675, 1468

Hawley J. F., Gammie C. F., Balbus S. A., 1995, ApJ, 440, 742

Hiemstra, B., Soleri, P., Mendez, M., Belloni, T., Mostafa, R., Wijnands, R., 2009, MNRAS in press (arXiv0901.2255)

Homan, J., Wijnands, R., van der Klis, M., Belloni, T., van Paradijs, J., Klein-Wolt, M., Fender, R., & Méndez, M., 2001, ApJS, 132, 377

Hynes R. I., Steeghs D., Casares J., Charles P. A., O'Brien K., 2003, ApJ, 583, L95

Hynes, R. I., Steeghs, D., Casares, J., Charles, P. A., O'Brien, K., 2004, ApJ, 609, 317

Hynes R. I., Brien K. O., Mullally F., Ashcraft T., 2009, MNRAS, 399, 281

Ibragimov A., Poutanen J., 2009, MNRAS, 1322

Ingram A., Done C., Fragile P. C., 2009, MNRAS, 397, L101

Jahoda K., Swank J. H., Giles A. B., Stark M. J., Strohmayer T., Zhang W., Morgan E. H., 1996, in Siegmund O. H., Gummin M. A., eds, Proc. SPIE Vol. 2808, EUV, X-Ray, and Gamma-Ray Instrumentation for Astronomy VII. SPIE, Bellingham, p.59

Kolb, U., 2010, Extreme environment astrophysics, Cambridge University Press

Kolehmainen M., Done C., 2010, MNRAS, 406, 2206

Kotov O., Churazov E., Gilfanov M., 2001, MNRAS, 327, 799

Lasota J.-P., 2001, NewAR, 45, 449

Li L.-X., Zimmerman E. R., Narayan R., McClintock J. E., 2005, ApJS, 157, 335

Lyubarskii, Y. E., 1997, MNRAS, 292, 679

Maccarone, T. J., Gallo, E., Fender, R., 2003, MNRAS, 345, L19

Magdziarz P., Zdziarski A. A., 1995, MNRAS, 273, 837

Malzac J., Beloborodov A. M., Poutanen J., 2001, MNRAS, 326, 417

Malzac, J., 2007, APSS, 311, 149

M^{c}Hardy, I. M., Körding, E., Knigge, C., Uttley, P., Fender, R. P., 2006, Nature, 444, 730

Mauche C. W., 2002, ApJ, 580, 423

Mayer, M., & Pringle, J. E., 2007, MNRAS, 376, 435

Meyer-Hofmeister, E., Meyer, F. 2003, A&A, 402, 1013

Miller J. M., Homan J., Steeghs D., Rupen M., Hunstead R. W., Wijnands R., Charles P. A., Fabian A. C., 2006, ApJ, 653, 525

Miller J. M., Homan J., Miniutti G., 2006, ApJ, 652, L113

Miller J. M., et al., 2010, ApJ, 724, 1441

Miniutti G., Fabian A. C., Miller J. M., 2004, MNRAS, 351, 466

Muñoz-Darias T., Motta S., Belloni T. M., 2010, MNRAS, 1553

Narayan, R., & Yi, I., 1994, ApJ, 428, L13

Narayan R., Yi I., 1995, ApJ, 452, 710

Pandel D., Kaaret P., Corbel S., 2008, ApJ, 688, 1288

Papitto A., Menna M. T., Burderi L., Di Salvo T., D'Antona F., Robba N. R., 2005, ApJ, 621, L113

Papitto A., Di Salvo T., D'Aì A., Iaria R., Burderi L., Riggio A., Menna M. T., Robba N. R., 2009, A&A, 493, L39

Patruno, A., Rea, N., Altamirano, D., Linares, M., Wijnands, R., & van der Klis, M., 2009, MNRAS, 396, L51

Patruno A., Wijnands R., van der Klis M., 2009, ApJ, 698, L60

Poutanen J., Svensson R., 1996, ApJ, 470, 249

Poutanen J., Gierliński M., 2003, MNRAS, 343, 1301

Priestley M. B., 1981, Spectral Analysis and Time Series. Academic, London

Psaltis D., Belloni T., van der Klis M., 1999, ApJ, 520, 262

Reis, R. C., Fabian, A. C., Ross, R. R., Miniutti, G., Miller, J. M., Reynolds, C., 2008, MNRAS, 387, 1489

Reis R. C., Miller J. M., Fabian A. C., 2009, MNRAS, 395, L52

Remillard R. A., McClintock J. E., 2006, ARA&A, 44, 49

Revnivtsev, M., Gilfanov, M., & Churazov, E., 1999, A&A, 347, L23

Revnivtsev, M., Gilfanov, M., & Churazov, E., 2001, A&A, 380, 520

Reynolds, C. S., & Nowak, M. A., 2003, PHYSREP, 377, 389

Rodriguez, J., Corbel, S., Hannikainen, D. C., Belloni, T., Paizis, A., & Vilhu, O., 2004, ApJ, 615, 416

Ross R. R., Fabian A. C., 2005, MNRAS, 358, 211

Ross R. R., Fabian A. C., 2007, MNRAS, 381, 1697

Russell D. M., Fender R. P., Hynes R. I., Brocksopp C., Homan J., Jonker P. G., Buxton M. M., 2006, MNRAS, 371, 1334

Rykoff E. S., Miller J. M., Steeghs D., Torres M. A. P., 2007, ApJ, 666, 1129

Shakura N. I., Sunyaev R. A., 1973, A&A, 24, 337

Shapiro S. L., Lightman A. P., Eardley D. M., 1976, ApJ, 204, 187

Shimura T., Takahara F., 1995, ApJ, 445, 780

Shrader C. R., Kazanas D., Reig P., 2007, AAS, 38, 919

Uttley P., McHardy I. M., 2001, MNRAS, 323, L26

Uttley, P., Edelson, R., M^{c}Hardy, I. M., Peterson, B. M., Markowitz, A., 2003, ApJ, 584, L53

Uttley, P. Submitted to MNRAS.

Vaughan, B. A., Nowak, M. A., 1997, ApJ, 474, L43

Vaughan S., Edelson R., Warwick R. S., Uttley P., 2003, MNRAS, 345, 1271

Vaughan, S., Edelson, R., Warwick, R. S., Uttley, P., 2003, MNRAS, 345, 1271

Wijnands, R., & van der Klis, M., 1998, nat, 394, 344

Wijnands R., van der Klis M., 1999, ApJ, 514, 939

Wilkinson T., Uttley P., 2009, MNRAS, 397, 666

Wilms, Juett, Schulz & Nowak, In preparation.

Witt, H. J., Czerny, B., Zycki, P. T., 1997, MNRAS, 286, 848

Wu, Q., Gu, M., 2008, ApJ, 682, 212

Zdziarski A. A., Johnson W. N., Magdziarz P., 1996, MNRAS, 283, 193

Zdziarski A. A., Gierliński M., Mikołajewska J., Wardziński G., Smith D. M., Harmon B. A., Kitamoto S., 2004, MNRAS, 351, 791

Zurita, C., Durant, M., Torres, M. A. P., Shahbaz, T., Casares, J., Steeghs, D., 2008, ApJ, 681, 1458

Życki P. T., Done C., Smith D. A., 1999, MNRAS, 309, 561